



THE UNIVERSITY OF QUEENSLAND
AUSTRALIA

Automatic Mesh Generation and Adaptive Remeshing for Geological Modelling

Yan Liu

Master of Engineering

*A thesis submitted for the degree of Doctor of Philosophy at
The University of Queensland in 2015*

School of Earth Sciences

Centre for Geoscience Computing

Abstract

Structures of faults, fractures and geomaterial interfaces are complex, making their behaviour difficult to predict. The ability to simulate geomechanical, geochemical and hydrogeological behaviours with these structures is required for better engineering process ahead of design. A pivotal step of geological simulation using the commonly applied finite element method is the mesh generation which is the subdivision of spatial objects into small elements. When complicated constraints such as faults, fractures and interfaces are present existing mesh generation methods are still far from feasible solutions for geological modelling. This thesis addresses this key issue and demonstrates how to generate high-quality mesh for representation of geo-objects with heterogeneous structures.

This thesis focuses on proposing a comprehensive solution for meshing and remeshing for geological modelling. The primary contributions are summarized as follows:

1. A boundary focused quadrilateral mesh generation method has been developed to produce high-quality mesh models for 2D multi-material geological data. Together with geodesic isolines, a valence clear-up pattern “Pisces” developed in this thesis is employed to improve the mesh quality. Hence the proposed method has more advantages in generating high-quality elements compared with algorithms developed by previous researchers (Park et al. 2007, Lee et al. 2003.) In the application to meshing images of coal plugs and fractured rocks, layers of well-aligned elements parallel to the material interfaces are generated and thus the average element quality of the generated mesh is close to that of a regular quadrilateral;

2. An effective 3D meshing method has been proposed and implemented towards generating mesh representations for fractured rocks. A high-resolution image can capture fracture structures in detail but it leads to a huge data set. To reduce the data size, surface meshes (served as constraints within volume meshes) rather than traditional volume meshes are utilized to represent fractures in this research. A simplified Voronoi diagram based on a proposed pseudo-surface assumption is developed to extract fractures, identify fracture junctions and indirectly generate high-quality meshes. Subsequent numerical experiments showed that the generated mesh representing a fractured rock has a high shape similarity 64.57% and its data size is merely 1/6000 as much as that of the image data.

3. A strategy has been carried out for meshing 3D geological reservoirs with arbitrary stratigraphic surface constraints. To achieve this, a geodesic-based procedure is designed to provide a robust implementation for handling geometrical heterogeneity on stratigraphic surfaces (i.e. stratum interfaces). The procedure also contributes to a well-designed advancing front technique which achieves the generation of high-quality elements and adaptive meshes. The effectiveness of the proposed strategy is demonstrated by meshing a reservoir geological model of Lawn Hill in Queensland, Australia.

4. A 3D remeshing approach conforming to stratum interfaces has been developed for simulating dynamic geo-engineering processes by finite element applications. To preserve stratum interfaces and clearly represent geological models, 2D and 3D stratum preservation algorithms are integrated to carry out a complete solution for remeshing with the consistency of interfaces. A near well bore drilling and a long wall caving model are utilized to demonstrate the capability of the proposed remeshing approach application in both the petroleum and coal mining industry.

In summary, the thesis presents both 2D and 3D strategies for generating high-quality mesh representations of geo-objects with heterogeneous structures in reality. This provides a link between geological data and numerical analysis. The methods and algorithms developed in this study are quite general thus can be widely applied to bring various geological data into numerical simulations for both geo-science and geo-engineering.

Declaration by author

This thesis is composed of my original work, and contains no material previously published or written by another person except where due reference has been made in the text. I have clearly stated the contribution by others to jointly-authored works that I have included in my thesis.

I have clearly stated the contribution of others to my thesis as a whole, including statistical assistance, survey design, data analysis, significant technical procedures, professional editorial advice, and any other original research work used or reported in my thesis. The content of my thesis is the result of work I have carried out since the commencement of my research higher degree candidature and does not include a substantial part of work that has been submitted to qualify for the award of any other degree or diploma in any university or other tertiary institution. I have clearly stated which parts of my thesis, if any, have been submitted to qualify for another award.

I acknowledge that an electronic copy of my thesis must be lodged with the University Library and, subject to the policy and procedures of The University of Queensland, the thesis be made available for research and study in accordance with the Copyright Act 1968 unless a period of embargo has been approved by the Dean of the Graduate School.

I acknowledge that copyright of all material contained in my thesis resides with the copyright holder(s) of that material. Where appropriate I have obtained copyright permission from the copyright holder to reproduce material in this thesis.

Publications during candidature

Refereed Journal Articles

1. **Y. Liu**, H. L. Xing. (2014). A feature extracting and meshing approach for sheet-like structures in rocks, *Computer Methods in Applied Mechanics and Engineering*, 276: 396-409
2. H. L. Xing, **Y. Liu**, J. F. Gao, and S. J. Chen. (2015) Recent Development in Numerical Simulation of Enhanced Geothermal Reservoirs, *Journal of Earth Science*, 26: 28-36
3. **Y. Liu**, H. L. Xing. (2013). A boundary focused quadrilateral mesh generation algorithm for multi-material structures, *Journal of Computational Physics*, 232: 516-528.
4. H. L. Xing, **Y. Liu**. (2011). Automated quadrilateral mesh generation for digital image structures, *Theoretical and Applied Mechanics Letters*, V1(6): 061001.

Peer-Reviewed Conference papers

1. H. L. Xing, **Y. Liu**. (2014). Mesh generation for 3D geological reservoirs with arbitrary stratigraphic surface constraints, *Procedia Computer Science*, 29: 897-909.
2. **Y. Liu**, H. L. Xing. (2013). Surface mesh generation of large-scale digital rock images in 3D, *Procedia Computer Science*, 18: 1208-1216
3. H. L. Xing, J. F. Gao, **Y. Liu**. (2012). PANDAS: high performance geocomputing software and its potential application in deep mining. In: T. Mares, Eastern Australasian Basins Symposium IV. Fourth Eastern Australasian Basins Symposium and Exhibition (EABS IV), Brisbane, Australia, (1-5). 11–14 September 2012.
4. H. L. Xing, J. F. Gao, J. Zhang and **Y. Liu** (2012). Recent Development in Simulation of Enhanced Geothermal Reservoirs (5 pages), *International Workshop of Deep Geothermal Systems*, Wuhan China, June 29-30, 2012.
5. H. L. Xing, J. Zhang, J. F. Gao and **Y. Liu** (2011), PANDAS and Its New Applications in Geothermal Modelling, *Proceedings of AGEC 2011 (Australian Geothermal Engineering Conference)*, pp293-298, Melbourne, 16-18 Nov 2011.

Publications included in this thesis

Y. Liu, H.L. Xing. (2014). A feature extracting and meshing approach for sheet-like structures in rocks, Computer Methods in Applied Mechanics and Engineering, 276: 396-409. Refereed Journal Paper – incorporated in Chapter 3.

Y. Liu (PhD candidate) designed the solution algorithm, implemented the algorithm by C++ programming language and wrote manuscript; H.L. Xing (Principle PhD supervisor) raised the related scientific questions, reviewed and edited manuscript.

Y. Liu, H.L. Xing. (2013). A boundary focused quadrilateral mesh generation algorithm for multi-material structures, Journal of Computational Physics, 232: 516-528. Refereed Journal Paper – incorporated in Chapter 2.

Y. Liu (PhD candidate) designed the solution algorithm, implemented the algorithm by C++ programming language and wrote manuscript; H.L. Xing (Principle PhD supervisor) raised the related scientific questions, reviewed and edited manuscript.

H.L. Xing, Y. Liu. (2014). Mesh generation for 3D geological reservoirs with arbitrary stratigraphic surface constraints, Procedia Computer Science, 29: 897-909. Peer-Reviewed Conference Paper – incorporated in Chapter 4.

Y. Liu (PhD candidate) designed the solution algorithm, implemented the algorithm by C++ programming language and wrote manuscript; H.L. Xing (Principle PhD supervisor) raised the related scientific questions, reviewed and edited manuscript.

Contributions by others to the thesis

Huilin Xing and Hans Mulhaus put together the initial proposals for funding through the ARC for Discovery and International Linkage projects that resulted in the conception of the multiscale multiphase supercomputer simulation and applications in geo-engineering and natural hazard analysis as a whole, of which this thesis was a part.

My advisors Huilin Xing and Joan Esterle of the School of Earth Sciences, the University of Queensland, each contributed to editing the thesis prior to submission.

Dr Jianping Zuo of China University of Mining and Technology, Ms P Liu of Research Institute of Petroleum Exploration& Development, China and Professor and Director Margie Scott of SMI BRC of University of Queensland provided the related data through Huilin Xing, which respectively used as application examples in Chapter 2, 3 and 4.

Statement of parts of the thesis submitted to qualify for the award of another degree

None

Acknowledgements

First and foremost, I would like to give my heartfelt thanks to my principle supervisor Associated Professor Huilin Xing, for providing me with the opportunity to join such a supportive and active research group in UQ and work with him. His guidance, foresight and serious attitude for research, have been critically important throughout my PhD studies. I would also like to express my sincere gratitude to my associate supervisor Professor Joan Esterle, for her endless encouragement and assistance in all the PhD milestones and efforts in reviewing this document.

My thanks go to Professors Hans Muhlhaus and Gregg Webb for their pertinent comments on my PhD project in each of my PhD milestones. My special thanks are given to Professors Zhenqun Guan and Hongwu Zhang of Dalian University of Technology. They introduced me to Huilin in 2008 and provided me with sagacious judgments and guidance on my research work. I would like to thank two visiting scholars: Associated Professor Zhiwei Tian of China University of Geosciences for helping me with my PhD confirmation presentation and Associated Professor Shaojie Chen of Shandong University of Science and Technology for discussing the long wall caving model with me in Chapter 5.

My thanks go to Dr Louise Olsen-Kettle, Dr Joel Fenwick and Dr Vince Boros for their help to polish up my English in the thesis and publications. I am grateful to a long list of people Ms Jinfang Gao, Mr Nianchao Zhang, Mr Xiangchong Liu, Mr Quanshu Li, Mr Zhiting Han, Ms Qin Li, Mr Fei Ren, Ms Jie Yi. They bear my stupid questions in mining science and petroleum engineering and share all the happiness time in BBQs, picnics and bush walking with me. I would like to thank Professor Stephen Tyson, Associated Professor Lutz Gross, Mr Ziping Fang, Dr Yucang Wang, Dr Jingyu Shi, Ms Ashleigh Paroz, Ms Tracy Paroz et al. for their assistance, advice and friendship.

For the financial support, I acknowledge the support given by the Australian government for the International Postgraduate Research Scholarship, the University of Queensland for the UQ Centennial Scholarship, Australia Research Council (ARC) for ARC DP 0666203 and ARC LX0989423 project and the School of Earth Sciences for the travel grant, which enable me to concentrate on the research.

I am grateful to Dr Jianping Zuo from China University of Mining and Technology, Ms Ping Liu from Research Institute of Petroleum Exploration& Development, China and Professor and Director

Margie Scott of SMI BRC of University of Queensland for providing the micro-CT datasets and geological data used in this thesis.

Above all, to my wife and parents, thank you for your unwavering love and support.

Keywords

Mesh generation, remeshing, Delaunay triangulation, digital rock physics, imaging, fracture, rock, geo-object, finite element method.

Australian and New Zealand Standard Research Classifications (ANZSRC)

ANZSRC code: 091001 CAD/CAM Systems, 60%

ANZSRC code: 091406 Petroleum and Reservoir Engineering, 40%

Fields of Research (FoR) Classification

FoR code: 0404 Geophysics, 60%

FoR code: 0914 Resources Engineering and Extractive Metallurgy, 40%

Table of Contents

Abstract	I
Declaration by author	III
Publications during candidature	IV
Publications included in this thesis.....	V
Contributions by others to the thesis	VI
Acknowledgements.....	VII
Keywords.....	IX
Australian and New Zealand Standard Research Classifications (ANZSRC)....	IX
Fields of Research (FoR) Classification	IX
Table of Contents	X
List of Figures & Tables	XIII
Chapter 1 Introduction	1
1.1 Background	1
1.2 Research aims	2
1.3 Geocomputing by finite element method.....	3
1.4 Unstructured mesh generation	4
1.5 Imaging and meshing	9
1.6 Geological packages and meshing	13
1.7 Remeshing in geocomputing.....	15
1.8 Summary of findings.....	17
1.9 Thesis Outline	18
Chapter 2 Two-Dimension Mesh Generation for Heterogeneous Rock.....	19

2.1	Overview	19
2.2	The paper.....	20
2.3	Conclusions	34

Chapter 3 Three-Dimensional Mesh Generation for Fractured Rock 35

3.1	Overview	35
3.2	Digital rock imaging	36
3.3	3D Fracture junction identification	36
3.3.1	Fracture medial surface extraction.....	36
3.3.2	Disk scanning method for fracture junction identification	37
3.4	Simplified centroidal Voronoi diagram and mesh generation	39
3.4.1	Simplified Centroidal Voronoi Diagram (SCVD) construction for fractures.....	39
3.4.2	Mesh generation for fractures	42
3.5	Mesh repairing	43
3.5.1	Umbrella operation	44
3.5.2	Effectiveness evaluation	45
3.6	Mesh optimization.....	47
3.7	Numerical applications	47
3.7.1	The workflow of the proposed algorithm	48
3.7.2	The choice of an optimal Voronoi cell radius	50
3.7.3	The application to a complicated fracture structure	55
3.7.4	Time efficiency analysis	60
3.8	Conclusions	60

Chapter 4 Three-Dimensional Mesh Generation for a Geological Reservoir 62

4.1	Overview	62
4.2	Background mesh generation.....	63
4.3	Surface remeshing.....	64
4.3.1	Detection zone generation	64
4.3.2	Front mergence	65
4.3.3	Front construction.....	68
4.3.4	Surface mesh generation.....	68
4.4	Volume mesh generation	69
4.5	Numerical applications	69
4.5.1	Lawn Hill and its geological model.....	69
4.5.2	Surface remeshing for the Lawn Hill model.....	70
4.5.3	Volume mesh generation for the Lawn Hill model	72
4.5.4	Integrated meshing process for the Lawn Hill model.....	74

4.6	Conclusions	77
-----	-------------------	----

Chapter 5 An Adaptive Remeshing Approach for Geological structure with Stratum Interface Constraints 79

5.1	Overview	79
5.2	Mesh density control and centroidal Voronoi diagram.....	80
5.2.1	Mesh density control.....	80
5.2.2	Centroidal Voronoi diagram based on mesh density control.....	81
5.3	2D remeshing with confirmed stratum interface.....	82
5.3.1	Node reposition.....	82
5.3.2	Edge removal	84
5.4	3D remeshing with confirmed stratum interface.....	85
5.4.1	Stratum interface remeshing	85
5.4.2	Volumetric mesh generation.....	86
5.5	Numerical applications	88
5.5.1	Remeshing for a vertical well drilling	88
5.5.2	Remeshing for a horizontal long wall caving	91
5.6	Conclusions	93

Chapter 6 Conclusions and Future Work..... 95

6.1	Conclusions	95
6.2	Future work	96

References..... 98

List of Figures & Tables

Figure 1.1: Weighted centroidal Voronoi tessellation built with 100 iterations of Lloyd relaxation (left), and final remeshing with 50k vertices (right) [28].	6
Figure 1.2: CT scan volumes of (a) Berea sandstone and (b) carbonate sample. The sizes of (a) and (b) are $724 \times 724 \times 724$ and $1024 \times 1024 \times 1024$ respectively. [3].	10
Figure 1.3: Marching Cube [117].	11
Figure 1.4: A geological model created by Petrel (http://www.slb.com)	14
Figure 3.1: Medial surface extraction: (a) fractures extracted from a rock and (b) the medial surface	37
Figure 3.2: Scanning disks with different W_2 values: W_2 of a flat disk (a) is higher than that of a non-flat disk (b).	38
Figure 3.3: Junction identification: left and right are the same fractures with different view angles and colours indicate different JWs on the fractures.	39
Figure 3.4: Simplified Voronoi diagram construction: (a) a patch and its generators; (b) the growing Voronoi cells; (c) the final Voronoi diagram.	41
Figure 3.5: The enhanced construction of SCVD for fractures: (a) the SCVD at fracture junctions, (b) the SCVD at fracture surfaces and (c) the SCVD for the fractures.	41
Figure 3.6: Triangular element construction: (a) a regular case and (b) an ambiguous case	42
Figure 3.7: Amending strategy for triangular element construction: (a) the SCVD with ambiguity; (b)-(f) the proposed amending processes based on the proposed strategy	43
Figure 3.8: An umbrella operation on a surface node N : (a) incident triangles and edge constraints in red, (b) the parameterized mesh in 2D domain, (c) the 2D mesh with recovered edge constraints and (d) reconstructed triangles and new generated edge constraints in blue.	45
Figure 3.9: Cases failed to satisfy the VMC: (a) a failed umbrella operation; (b) overlapped junction triangles.	47
Figure 3.10: Fractures of a rock mass: (a) the fractures in voxel format, (b) medial surfaces of the fractures, (c) the JW diagram, (d) the SCVD, (e) the initially generated mesh, (f) the repaired mesh, (g) the optimized mesh and (h) the volume mesh for the fractures.	50
Figure 3.11: A 3D rock image meshed with different element sizes: (a) the 3D rock image with a size of $1012 \times 1024 \times 931$; (b) the internal structures; (c) the major fractures; (d)-(f) are triangular meshes generated by different Voronoi cell radii where the major fractures are shown in white colour and the outside rock boundaries in golden.	52
Figure 3.12: Relationship between shape similarity and Voronoi cell radius: the highest similarity is 64.57% when the Voronoi cell radius is 7	53

Figure 3.13: Mesh generation for a rock image: (a) surface mesh of the main structure; (b) surface mesh with the input image; (c) surface mesh with thickness property and (d) the volume mesh with 28,631 nodes and 143,901 elements.	54
Figure 3.14: Fractures of a rock mass: (a) 216 fractures within the rock and (b) one slice of the fractures.....	55
Figure 3.15: Relationship between the JW threshold and the percentage of failed umbrella operations.....	56
Figure 3.16: Relationship between the JW threshold and the junction residual ratio.....	57
Figure 3.17: Mesh models for the fractures in Figure 3.14: (a) and (b) are the surface meshes with different view angles, (c) is the corresponding volume mesh containing 193,144 nodes and 1,089,010 elements and (d) is a close-up of the part marked in (c).	58
Figure 3.18: Manually repairing a failed umbrella operation: (a) the local mesh before repairing and (b) the local mesh after repairing. Junction node is red and surface node is blue. N is the node where the umbrella operation fails.....	59
Figure 4.1: Workflow of the proposed method.	62
Figure 4.2: Surfaces extracted from a reservoir model. The border lines indicate surface junctions.	63
Figure 4.3: The appropriate choice of ζ for front generation.	64
Figure 4.4: geodesic distance updating with different DZ widths: (a) $\zeta = \zeta$; (b) $\zeta = 3.4\zeta$	65
Figure 4.5: A node P and its 8 vicinities v_i ($i=1, 2, \dots, 8$).	66
Figure 4.6: collision detection: (a) DZ is generated according to the source points which are in green. Colours indicate the magnitude of node CDVs; (b) a close-up of (a).	67
Figure 4.7: DZ mergence.	67
Figure 4.8: Front mergence: (a) the green points are source and bright blue zones are current layer; (b) the result of detection zone updating.....	68
Figure 4.9: Front construction: (a) two green points are source and belt width is $\zeta=8.5$; (b) belt width is $\zeta=4.3$	68
Figure 4.10: Triangular mesh generation for belts: (a) the segmented fronts; (b) the Voronoi diagram for the belt; (c) triangular mesh of the belt.	69
Figure 4.11: The Lawn Hill model which is built by GoCAD with 7.1×10^7 voxels.	70
Figure 4.12: Remeshing for a rock stratum interface: (a) is a stratigraphy surface; (b) is the surface mesh (2.8×10^6 elements) extracted by the marching cube method [175]; (c) mesh (1.5×10^4 elements) created by the proposed remeshing method; (d) and (e) are the close-ups of (b) and (c) respectively.....	71
Figure 4.13: Remeshing by different size fields: (a) $S_{max}=20$, $q=1.1$ and $S_{seg}=2.5$; (b) $S_{max}=20$, $q=1.2$	

and $S_{seg}=2.5$; (c) $S_{max}=30$, $q=1.1$ and $S_{seg}=5$; (d), (e) and (f) are the close-ups of (a), (b) and (c) respectively.....	72
Figure 4.14: Volume mesh generation for the reservoir model: (a) and (b) are two adjacent strata; (c) is a close-up of the volume meshes.....	74
Figure 4.15: Lawn Hill geological model: (a) a rock stratum interface remeshed by the proposed method; (b) the surface mesh; (c) the volume mesh with 1.7×10^5 nodes and 9.7×10^5 elements; (d) 10 meshed components of the geological model.	77
Figure 5.1: An elliptic cylinder for the governing remeshing zone	80
Figure 5.2: A Voronoi cell in 2D domain	82
Figure 5.3: remeshing for a patch of geological mesh model: (a) is an old mesh to be remeshed; (b) is an isotropic remeshing result based on the proposed size map H	83
Figure 5.4: A remeshed model conforming to stratum interfaces	85
Figure 5.5: A well pass through a stratum interface.....	86
Figure 5.6: A long wall mining example.....	86
Figure 5.7: A cube consists of five tetrahedra	87
Figure 5.8: one step of a well drilling process: (a) the well and remeshing zone, (b) stratum interface within the remeshing zone, (c) the size map, (d) the stratum interface after remeshing and (e) the volumetric mesh after remeshing.	90
Figure 5.9: A well drilling process: (a) the well model, (b) the stratum interfaces and (c)-(f) the well drilling steps. The charts are element quality measured by the minimum dihedral angle in tetrahedral elements.	91
Figure 5.10: 2D adaptive remeshing conforming to stratum interfaces: (a) is the old mesh model and (b) is the remeshed result.	92
Figure 5.11: 3D adaptive remeshing conforming to stratum interfaces: (a) is the original mesh model and (b) is a half of it. (c)-(f) are the caving steps driven by the proposed remeshing method, where the charts are element quality measured by the minimum dihedral angle in tetrahedral elements.	93
Table 3.1: Summary for surface meshes in Figure 3.11 (d)-(f).....	52
Table 3.2: Grid model for Figure 3.11 (c) with different sample rates	53
Table 3.3: Element quality for Figure 3.13 (d).....	55
Table 3.4: Element quality for Figure 3.17 (c).....	59
Table 3.5: Time efficiency (unit: s)	60
Table 4.1: Element qualities of mesh in Figure 4.15 (c)	77

List of Abbreviations used in the thesis

FEM	Finite Element Method
FVM	Finite Volume Method
FDM	Finite Difference Method
LBM	Lattice Boltzmann Method
XFEM	Extended Finite Element Method
GFEM	Generalized Finite Element Method
3D	Three-Dimensional
2D	Two-Dimensional
AFT	Advancing Front Technique
NMR	Nuclear Magnetic Resonance
CT	Computed Tomography
MRI	Magnetic Resonance Imaging
SEM	Scanning Electron Microscopy
MC	Marching Cubes
MT	Marching Tetrahedra
GIS	Geographic Information System
CAE	Computer Aided Engineering
JW	Junction Weight
BFS	Breadth First Search
SCVD	Simplified Centroidal Voronoi Diagram
VMC	Valid Mesh Criterion
DZ	Detection Zone
CDV	Collision Detector Vector

Chapter 1 Introduction

This thesis focuses on research and development of meshing and remeshing for geological modelling. In this chapter, the research background and research aims are introduced, then followed by a literature review including geocomputing, meshing, imaging, geological modelling and remeshing. Based on this review, challenges and problems are pointed out. Finally, an outline is provided to give readers an overview of the thesis.

1.1 Background

Geological processes are always complex and may change through time or due to man's intervention. Researchers have recognised the need to improve our knowledge of such processes through simulating reality. One vital step of geological simulation is the subdivision of spatial objects into small elements, which is well known as the Mesh Generation [1]. Mesh generation converts geological data to mesh models which are accepted by numerical simulation applications. Generally the various methods for obtaining geological data have been well developed and numerical simulations themselves are relatively mature, but the mesh generation in geology is still relatively new and quite challenging [2]. The key problem here is how to generate a high-quality mesh for a representation of geo-objects with heterogeneous structures including fractures.

Advanced imaging techniques are ubiquitously applied to obtain geological data and visualize rock samples in an intuitive way [3]. It can clearly identify mineral composition and fracture structures through high-resolution digital images. Geological packages such as GoCAD (<http://www.gocad.org>), GSI3D (<http://gsi3d.org>), Petrel (<http://www.slb.com>), have been developed over decades to achieve the determination of the spatial variation of a broad suite of data sources from mining, engineering, hydrogeology and environmental restoration fields. In general, current visualizing and static modelling toolkits are sophisticated to effectively describe both rocks in core-plug scale and geo-objects in basin/reservoir scale.

The finite element method (FEM), finite volume method (FVM), finite difference method (FDM) and lattice Boltzmann method (LBM) are employed to provide numerical solutions for problems in

geology [4]. FEM is perhaps the most widely applied numerical method over fields of both science and engineering. FEM provides flexibility for the treatment of material heterogeneity, non-linear deformability, complex boundary conditions, in situ stress as well as gravity. Moreover, the extensions of FEM such as extended FEM (XFEM) and generalized FEM (GFEM) are adopted to simulate fracture propagation which is recognized as one of the most difficult issues in rock mechanics. FDM has also been widely used but it cannot be used in domains with arbitrary shapes; thereby FVM accepting unstructured meshes is developed to overcome this difficulty. LBM using structured meshes is applied to single and multi-phase flow simulations and its applications are limited to fluid flow problems.

Mesh generation is the corner-stone of many simulations of geoscience processes and the bridge between geological data and numerical simulation. Due to the simple implementation, structured meshes are adopted by most geological software packages to represent geological models. Numerical methods such as FDM and LBM benefit from using this direct and intuitive modelling technique. However use of only structured mesh has drawbacks. Its inability to accurately represent complex geometries leads to difficulty in describing constraints such as fractures in rocks and object interfaces in geological models. Unstructured meshes are an ideal choice for depicting complex constraints. FEM based on unstructured meshes are advantageous over methods based on structured meshes for geomechanical analysis, especially for those with complicated constraints [2]. However, mesh generation consisting with these constraints is difficult and a bottle neck for numerical simulations in geology. Therefore, this Ph.D. thesis focuses on the automatic mesh generation and adaptive remeshing for geological modelling, which provides a link between geological data and numerical simulation.

1.2 Research aims

The purpose of this PhD project is to develop solutions for meshing heterogeneous structures within geo-objects and provide an interface between geological data and numerical simulation. The proposed meshing approaches take the practical geo-objects as input and focus on generating high-quality meshes with surface/line constraints representing the faults, fractures and stratum boundaries/interfaces. The proposed approaches can also be utilized to generate unstructured meshes for geological data generated by using commercial software (e.g. GoCAD). This method is the applied to a remeshing strategy conforming to stratum interfaces for simulating geo-engineering

processes such as caving and well drilling. Specifically, the primary objectives of this research are to:

- (1) study 2D quadrilateral mesh generation methods and develop a boundary focused approach for meshing multi-material structures with quadrilateral mesh;
- (2) develop a 3D surface mesh generation method for extracting and meshing fractures in digital rock images;
- (3) develop a 3D mesh generation method for meshing geological reservoirs;
- (4) design a remeshing strategy for simulation of caving and well drilling processes.

1.3 Geocomputing by finite element method

The finite element method [5] is a numerical technique for solving partial differential equations and routinely applied in studying deformation, temperature, fluid flow and coupled multi-physics problems. The basic idea of finite element method is achieving an approximation to continuum problems by the following two steps: (1) dividing the continuum into a finite number of elements and (2) solving the complete system consisting of its elements by the same rules of dealing with standard discrete problems [5]. The primary element shapes include triangle/quadrilateral for 2D domain and tetrahedron/hexahedron for 3D domain. Quad/hex elements could achieve a higher accuracy, while tri/tet elements have the advantages of representing complex geometries. Over the last two decades, the applications of FEM have been widely applied in the field of coal mining, geothermal exploration, CO₂ geo-sequestration, nature disaster prediction, rock property estimation, etc.

In coal mining, Valliappan and Wohua [6] utilized a finite element model to simulate the distribution of pressure and the concentration of methane gas due to gas migration in coal seams. Islam et al. [7] employed finite element analyses to evaluate stress redistribution, strata failure, and water inflow enhancements that result from these coal extraction operations in Bangladesh. They demonstrated that multi-slice extraction of coal would ultimately lead to a major water inflow hazard in the mine. Toraño et al. [8] simulated the behaviour of a longwall coal mining installation as well as the roof supporting through a virtual reality model approach. Zhu et al. [9] built a model

to simulate the coal–gas interaction under different temperatures. They suggested taking account of the thermal impact on coal-gas interactions especially for the domain with high temperature.

In geothermal exploration and CO₂ geo-sequestration, researchers usually focus on studying temperature and fluid flow within reservoirs. Ghassemi et al. [10] presented a 3D integral equation formulation to calculate heat extraction-induced thermal stress in enhanced geothermal reservoirs. They announced the proposed system can provide solutions for the injection/extraction in an arbitrarily shaped fracture. Zhou et al. [11] studied the poroelastic and thermoelastic effects of cold water injection in enhanced geothermal reservoirs. The application example shows that the rock cooling increases fracture conductivity, whereas fluid leakoff indirectly decreases fracture aperture. In CO₂ geo-sequestration, Shukla et al. [12] introduced a review of caprock integrity in geo-sequestration of carbon dioxide. Meanwhile, a FEM-based model of the CO₂ geosequestration system is developed to simulate coupled processes governed by highly nonlinear partial differential equations.

In the field of nature disaster prediction, the geomechanical behaviour of fault systems attracts a number of on-going researches. Xing et al. [13] studied the interacting fault systems through a finite element model and carried out a numerical simulation of the fault system in Southern California. Hsu et al. [14] utilized FEM models to examine the impact of fault slip, topography and variations in an elastic module on surface displacements. They also applied this model to analyse the 2005 Mw 8.7 Nias-Simeulue, Sumatra earthquake. Manasa et al. [15] employed FEM to simulate the 2004 Great Indian Ocean Tsunami. And the model they built includes Bay of Bengal, Arabian Sea and Indian Ocean.

1.4 Unstructured mesh generation

Geological models are naturally complicated concerning their geometry. Unstructured meshes are appropriate for the description of such complex geological structures, which can be analysed by FEM, XFEM and FVM applications.

Automatic unstructured meshing method has been developed for decades [16], and a number of commercial and non-commercial meshing applications have been ubiquitously utilized in the field of engineering, medicine, geology, visualization and so on. These applications cover various issues in the mesh generation community, including mesh generation, optimization, parameterization,

reconstruction, remeshing, repairing, to name a few. A comprehensive introduction of all these topics is out of the scope of this thesis. Therefore, in the following context, the introduction of meshing techniques is grouped by the widely used element shapes in practical applications: triangle, quadrilateral, tetrahedron and hexahedron.

Triangular mesh generation is not only used for representing objects in 2D but also employed to describe surfaces in 3D. 2D triangular mesh generation is not an open issue and most of its problems have been well studied and resolved [17-19]. Regarding to 3D surface triangular mesh generation, surface remeshing is a key component and a number of methods [20] have been proposed. The motivation of surface remeshing is that meshes generated by scanning devices or by implicit representations could not satisfy the element quantity criteria of FEM applications. Hence remeshing techniques based on such pre-existing mesh models are carried out. Approaches [21-24] based on a joint parameterization are usually implemented by parameterizing the models on a base domain (e.g. sphere). To make joint parameterization more general, researches [25-27] split mesh into matching patches with identical connectivity boundaries, and then parameterize these patches into planar domain respectively. Praun et al. [27] yielded a Voronoi-based scheme which iteratively inserts a sample point as far as possible from current placed ones. Alliez et al. [28] proposed an interactive remeshing approach, allowing users to control the sampling density over the surface patch (see Figure 1.1). The approach benefits from the centroidal Voronoi tessellation proposed by Du et al. [29]. The above remeshing approaches may fail due to the distortion in the process of parameterization. Alternatively, geodesic-based remeshing using fast matching method [30] attracts the interest of researchers. One advantage of geodesic-based remeshing is that it implements on surface meshes directly without parameterization. Peyre and Cohen [31] advocated a geodesic remeshing using a front propagation. They [32] also employed Geodesic Centroidal Tessellation to address the problem of mesh partition. Sifri et al. [33] proposed a geodesic-based surface remeshing in a manner similar to ‘advancing front’ approach. It starts from an arbitrary point to segment the initial mesh into regions. After the segmentation, all regions are remeshed and connected to construct a new mesh. Compared with the parameterization-based methods, these approaches are usually slow and the element quality is usually low.

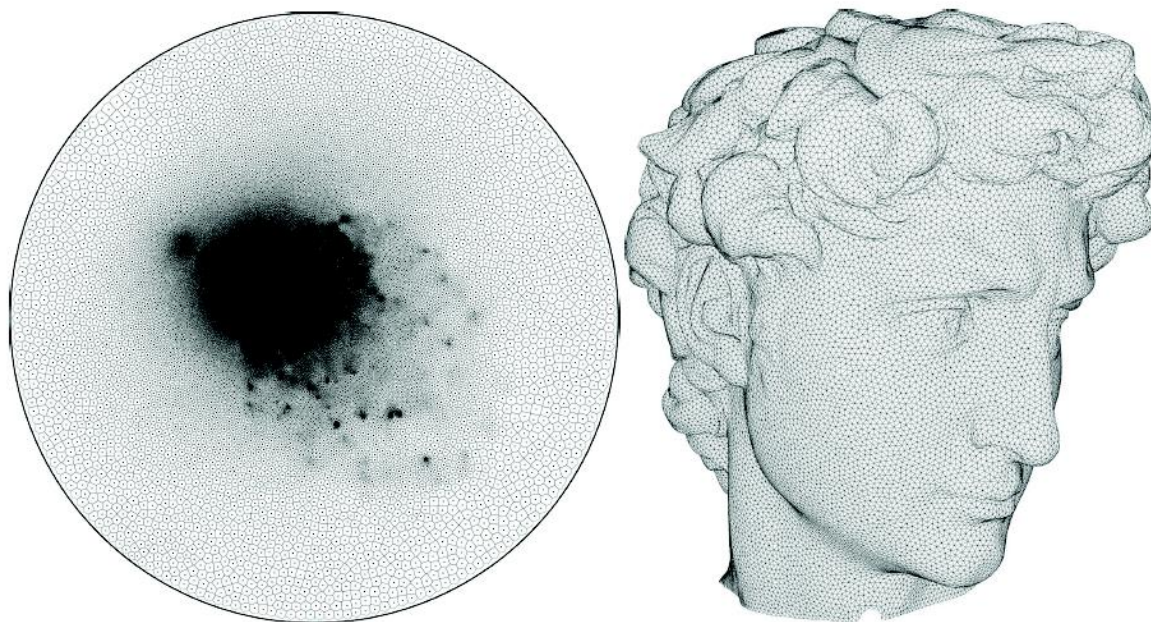


Figure 1.1: Weighted centroidal Voronoi tessellation built with 100 iterations of Lloyd relaxation (left), and final remeshing with 50k vertices (right) [28].

Quadrilateral meshes normally perform more efficiently and accurately than its triangular counterparts concerning FEM analysis. Generally, automatic quadrilateral mesh generation can be grouped into the following two categories: the direct approach and the indirect approach [16]. The direct approach is likely to generate well-aligned quadrilaterals parallel to the boundary of the domain or line constraints, such as ‘Paving’ [34, 35] and mapping-based approach [36]. The quality of the mesh generated in this way is usually better than that in the indirect approach. However, the direct approaches are not always achievable once boundaries or line constraints have complicated geometries. With regard to the geometry complexity, the indirect approach is more robust than the direct approach. The simplest indirect approach [37] is splitting a triangle into three quadrilaterals. This method guarantees an all-quad mesh, but the element quality is poor due to a number of irregular nodes [38] produced in the mesh. An alternative strategy is combining two triangles into one quadrilateral. Johnston et al. [39] and Lee and Lo [40] further developed this method to guarantee an all-quad mesh generation if the edge numbers of the input boundary are even. Borouckaki [41] proposed an adaptive meshing approach which firstly combines adjacent triangles and then splits triangle and quadrilateral into three and four quadrilaterals respectively. In contrast to the above indirect approaches, Owen et al. [42] designed the Q-Morph algorithm, which utilizes an advancing front method to generate quadrilaterals through existing triangular meshes. Lee [43] extended the Q-Morph for generating a quadrilateral mesh with line constraints. The advantage of Q-Morph-based methods is the maintenance of the desirable features of both boundaries of a domain and constraints inside. However, these methods rely on a well-generated triangular mesh capturing the model feature. Otherwise, they will crash or generate extremely bad quality

quadrilaterals in the connection of layers.

Hexahedral mesh generation has been an active research area in field of mesh generation for decades. As hexahedral elements can produce more accurate solutions than other elements, whenever it is possible hexahedral meshes are adopted in FEM-based simulations. However, automatic hexahedral mesh generation for arbitrary polyhedrons is difficult, which is well known as the “Holy Grail” in the meshing community. The most popular solutions of hexahedral mesh generation include: sweeping [44, 45], mapping [46-48], plastering [49-51], whisker-weaving [52-54], and octree-based algorithms [55-60]. Generally, sweeping methods [44, 45] can efficiently generate hexahedral mesh with high-quality elements for assembly geometries. However, these methods are limited to simple shapes and thus manually decomposing work is required to decompose models with complex structures into components with simple geometries. Although sweeping approaches are far from automatic mesh generation, they are undertaken by most of computer aided engineering packages to construct hexahedral meshes. Mapping is another popular hexahedral meshing technique which also requires manual interventions. The process of mapping approaches [46-48] mainly include two steps: (1) approximating model geometry structures by simplified configures and (2) mapping these configures to model boundaries. For instance, Nieser et al. [48] proposed the CubeCover method which designs a frame field for models and then undertakes the corresponding meshing process. Li and Tong [47] requested an initial hexahedral mesh inside models as the beginning of their inside-out advancing front technique. Plastering [49-51] can be recognized as an automatic hexahedral mesh generation methods, but they suffer from internal voids which lead to a convergence problem. Compared to plastering from a local view to generate meshes, the whisker-weaving approaches [52-54] attend to achieve automatic hexahedral mesh generation from a global view. The upside of whisker-weaving methods is they could generate elements parallel to boundaries, while the downside is they rely on the topology structure on the surface mesh and are difficult to apply to complex structures. Octree-based algorithms [55-57] is being used today to generate hexahedral meshes for a wide variety of models in medicine. Although these algorithms have the ability of automatically meshing complex geometries, it is impossible for them to construct well-aligned layers of elements parallel to model boundaries. The poor element quality around boundaries reduces the accuracy of the corresponding FEM analysis, which limits applications of octree-based mesh generation approaches.

Tetrahedral meshes can represent arbitrary volume geometries, which benefits from the mathematic properties of tetrahedron. The most popular tetrahedral meshing methods are the Octree mesh generation, the Delaunay mesh generation and the Advancing Front Technique (AFT). The Octree

mesh generation was firstly developed by Mark Shephard et al. [61, 62]. They employed an octree-structure to subdivide the geometric model till the desired mesh size is obtained. There are two major drawbacks of this approach: (1) generated meshes are not consistent with boundary surface meshes and (2) element quality close boundaries with high curvature and sharp corners are poor. Although researchers [63-68] undertook optimization methods to improve the element quality, tetrahedral meshes generated by the Octree method is still not comparable to that generated by AFT or Delaunay triangulation. Delaunay-based methods are the most popular techniques in the tetrahedral mesh generation community. Delaunay triangulation is the geometric dual of a Voronoi tessellation. Delaunay [69] introduced the theory of this configuration in 1934 with the property of empty circumsphere criterion. In 3D domain, the empty circumsphere criterion can be depicted as below: for every tetrahedron there are no vertices in its circumsphere except for its own vertices. In 1981, Bowyer [70] and Watson [71] proposed the method based on incremental insertion, which is proven as a simple and efficient Delaunay triangulation. Although the 3D Delaunay triangulation can automatically recover boundaries of a convex polyhedron, there is no guarantee for a concave or multi-connected polyhedron. The study of recovering polyhedron boundaries is undertaken by researches [72-74]. Besides, the removal of sliver or kite elements with zero volume is another crucial issue for Delaunay triangulation. Related refinement and optimization algorithms [75, 76] have been carried out to resolve this problem. AFT is another popular category of tetrahedral meshing. It is mainly contributed by Rainald Lohner [77, 78] and S. H. Lo [79, 80]. The concept of AFT is tetrahedrons are created layer by layer starting from polyhedron boundaries towards inner, which naturally generates layers of high-quality elements aligned to the boundaries. However, the drawback of AFT is there is no theoretical guarantee for the convergence and a typical case is schonhardt configuration [81]. To overcome this difficulty, George [82] utilized a revisit approach to enhance the convergence of AFT. Schöberl [83] optimally chose inserted nodes to avoid generating schonhardt-like polyhedron. Frey [84] innovatively combined Delaunay tetrahedralization with advancing-front approach to resolve the convergence problem. Compared to the hexahedral mesh generation, the tetrahedral mesh generation is more robust and thus widely applied to automatically construct models with complicated geometry boundaries and surface constraints. Although tetrahedral mesh generation is relatively mature, it is merely one stage of the object meshing process and cannot guarantee generating reasonable meshes for FEM applications independently. For instance, the generation of a high-quality tetrahedral mesh depends on an adequate triangular mesh input which is hard to obtain in some cases.

1.5 Imaging and meshing

With regard to geological models in core-plug scale, advantaged imaging techniques are ubiquitously utilized to obtain constructive minerals as well as fracture structures in rocks. Mesh generation based on rock images is crucial to study rock geomechanical, geochemical and hydrogeological behaviours. In this section, both imaging techniques and image-based meshing methods are introduced in detail.

Imaging technique is a part of computer vision which is a rich and rewarding topic. Traditional feature extractions [85] are based on 2D images acquired from an electronic camera and the applications are widely utilized in the field of face recognition [86], biometric identification [87] and Object categorization [88]. With the development of advanced imaging techniques such as nuclear magnetic resonance (NMR), X-ray computed tomography (CT) and scanning electron microscopy (SEM), 3D images and image-based modelling strategies [89] are studied by numerous researchers. In the field of medical science, heart [90], vessel [91] and brain [92] segmentations based on CT scanned 3D images are well studied and applied in the diagnosis and treatment by a skilled professional. In geo-science, advanced imaging technologies have been applied to observe rock structures (e.g. fractures [93], voids [94] and networks [95]) and study rock geomechanical, geochemical and hydrogeological behaviours. For instance, methane and other coal seam gases will flow out of pores of coal through these networks if there is a pressure gradient acting as a driving force. Therefore, the geometric properties of the networks have an essential impact on the flow behaviour gases in coal seams. Close and Mavor [96] stated that the main flow, by “Darcy-flow” through a coal bed, is determined by the cleat attributes: size, spacing, connection, aperture, mineral filling, and orientation pattern. Liu et al. [97] developed a fully-coupled hydrological–mechanical–chemical model to study fracture sealing and preferential opening and employed CT images to provide redundant constraints on fracture evolution by dissolution and precipitation. Methews et al. [98] utilized high-resolution CT images to observation the thermal drying processes of lump-sized subbituminous coal and studied new fracture propagation during this procedure.

Concerning rock images, rocks are usually made up of many constituents, ambiguities may happen if there is no prior knowledge about the constructive minerals. The partial volume effect is another reason for generating poor quality digital images. Digital imaging of such geomaterials is difficult in itself but is becoming more achievable [99-101]. Segmentation algorithms [102], together with the CT imaging techniques, are critical for labelling different rock objects and describing fracture structures. Such algorithms may be sensitive to the local image noise and may not produce

reasonable results for fractures with small thickness if the resolution is not high enough [103]. Therefore, high-resolution volumetric images are utilized to capture such geometric features (see Figure 1.2), but such high resolution images lead to a huge dataset, which may be out of current computer capabilities to analyse and even visualize [1, 104].

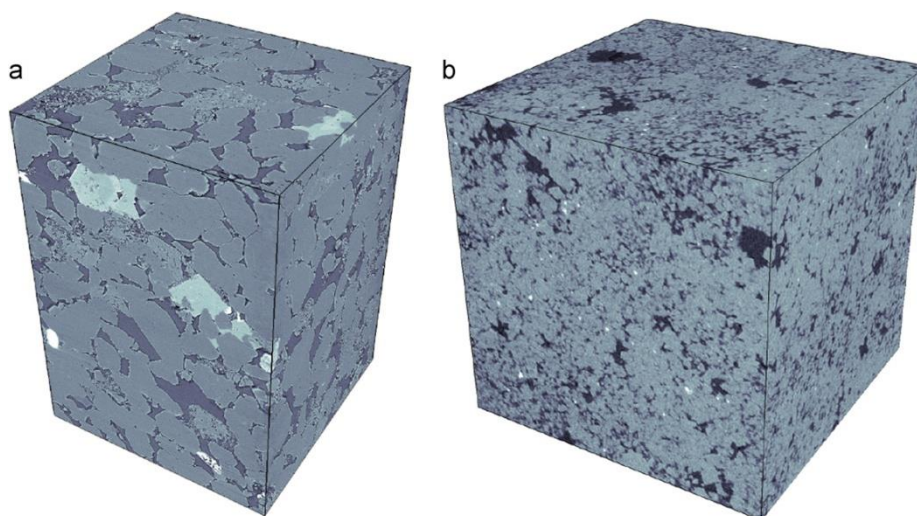


Figure 1.2: CT scan volumes of (a) Berea sandstone and (b) carbonate sample. The sizes of (a) and (b) are $724 \times 724 \times 724$ and $1024 \times 1024 \times 1024$ respectively. [3]

The most popular model for representing pore-scale rock samples is pore network. The model is proposed by Bryant and co-workers [105-107] and extended by Øren and Bakke [108, 109], which is utilized to predict relative permeability, electrical conductivity and capillary pressure of rock samples. Algorithms for extracting pore networks from images could be grouped into the axis based method and the maximal ball method. Readers interested in this topic are referred to [110]. Compared with methods based on pore network models, FEM has more advantages for complicated structure analysis, which is especially useful for studying the mechanical behaviours such as pressure, displacement, contact, conflict etc. An accurate FEM-based analysis relies on an adequately generated unstructured mesh model, and thus effective image meshing algorithms are desired.

The mesh generation for 3D images has been an active subject of a number of on-going studies [99, 111-115]. For meshing 3D images, the simplest way is to directly convert voxels into brick elements [111]. Such mesh models contain a huge dataset and jagged boundaries accounting for poor results and even errors in simulations [116]. Another strategy of image meshing is the octree-based approach, which is innovatively proposed by Zhang et al. [55, 99]. The advantage of their approach is the ability of creating quality hexahedral elements from images. However, like the other

grid-based approaches, it could not provide well-aligned elements parallel to interfaces, which are generally required by numerical simulations using hexahedral meshes.

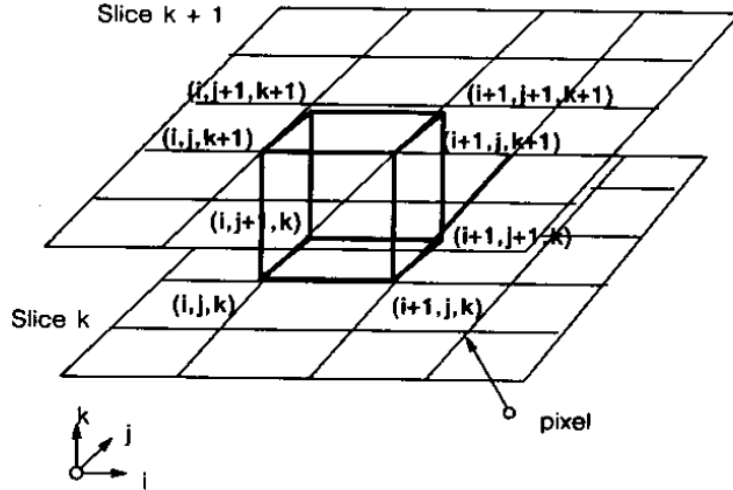


Figure 1.3: Marching Cube [117].

Currently the most popular image meshing approaches are based on the Marching Cubes (MC) method [117]. The MC considers voxels in an image as a lattice within a cubic cell and constructs local triangulation based on labels on the eight corners of the cell (see Figure 1.3). Although the MC method is robust and efficient, its drawbacks include: (1) the element size is uniform and depends on image resolutions, (2) staggered interfaces cannot smoothly represent sharp features and (3) interface ambiguities engender topological defects concerning meshing multi-material images. Coarsening methods [118, 119] are usually employed as a post-process for MC to indirectly generate adaptive meshes. However, the element quality is usually poor and geometry and topological flaws such as self-intersections and singular edges will emerge in the coarsening process. With regard to reproducing sharp features, the dual marching cubes method is proposed. Approaches [120, 121] based on this method introduce a representative vertex for each cells and then systematically connect these vertexes to construct meshes. Concerning multi-material images, as there are 8^8 or 16,777,216 possible cases of a cube with 8 vertexes, it is impossible to construct patterns for each of these cases. Efforts [112, 122, 123] have been made to extend MC to meshing images with different materials. One of these remarkable approaches is carried out by Wu et al. [112]. In their multi-material MC algorithm, they firstly constructed edges on the six faces of a cube, and then designed three different local facet generation methods according to the number of face-centred nodes. Consequently, the continuity and integrity of material boundary meshes are ensured by their robust approach. One important extension of MC is called the marching tetrahedra (MT) which is proposed by Shirley and Tuchman [124]. As the number of vertexes in a tetrahedron is 4, the quantity of possible marching patterns is smaller comparing to MC. For a 3D image, its

rectilinear grids are firstly subdivided into tetrahedral grids and then the MT is applied. Bonnell et al. [125] utilized the MT method to reconstruct material interfaces of volume fractions and their applications include a human brain data set from practice. d'Ottreppe et al. [126] focused on producing triangle surface meshes from multi-tissue segmented medical images and applied the proposed algorithm to a femur, a set of lumbar vertebrae and a mandible together with its teeth. In general, MC-based image meshing approaches are robust, but their lack of an adaptive control of element size and a guarantee of high element quality restricts the range of their applications.

Recently, image based meshing algorithms aiming at adaptive mesh generation with high quality have been studied by researchers. These algorithms could be roughly grouped into the AFT-based and the Delaunay-based techniques. The AFT-based methods [127-129] start from a set of seed points, i.e. front, which are previously created on model feature lines or domain boundaries. The progress of the front is achieved by choosing an edge in the front and constructing a new element attached to it. The basic approach is fast and effective in producing high-quality elements. However, self-intersections must be detected and avoided during the front progressing procedure, which will be acute when fronts are colliding from opposite directions. Thus, heuristically front detecting and smoothing strategies [130] always come with the AFT-based approaches to deal with collapsing or colliding, often at the expense of element quality in these areas. The Delaunay-based methods [131-134] firstly identify character nodes on material interfaces and then generate meshes preserving the interfaces. The character nodes are named as 0-cells, 1-cells and 2-cell, which represent nodes located on junctions, junction edges, and interfaces respectively. Meyer et al. [131, 132] proposed an image meshing approach for sampling and meshing material interfaces using a dynamic particle system. They sample nodes in a sequence of 0-cells, 1-cells and 2-cells. During the sampling process, a set of projection operators are carried out to enforce constraints of material interfaces. Based on the results from the level set literature [135], they indicated that the adequate angles between 1-cells are 120° at the 0-cells. In order to satisfy all the constraints and guarantee high-quality results, their sample scheme will cost a long computation times. Dey et al. [114, 134] achieved the meshing interface of multi-material data by Delaunay refinement. Specifically, they associated each sample a real valued weight as the radius of its protecting ball and proposed a restricted Delaunay triangulation aiming at preserving material interfaces. Concerning the refinement, they established a disk condition which request a topological disk formed by triangular elements around each node. The refining operations will be invoked whenever local mesh could not satisfy the disk condition. The idea of involving protecting balls is also employed by Boltcheva et al. [136] to preserve sharp features such as surface patches, edges and corners in multi-material images. In essence, the above Delaunay-based approaches benefit from the theory of surface

reconstruction by Voronoi filtering [137]. The material interfaces could be naturally extracted if there is a sufficient sampling density and local feature size is a vital aspect as far as preserving sharp features are required.

Concerning mesh generation for rock images, it is relatively new and challenging for the conventional image meshing techniques [117, 131-134]. Although these methods can create mesh models for rock masses with different constituents, they remain a lack of capability to adequately describe fractures. Due to the thin feature of fracture, the conventional methods generate a huge number of elements for fractures, which is difficult or impossible to use in FEM simulations. Alternatively, approaches [138-140] utilize a small number of elements to directly represent fractures through lines/surfaces in 2D/3D. Such approaches could naturally describe the geometry properties of fracture and significantly reduce the element quantity. However, the drawbacks of these methods is fractures within rocks can meet at arbitrary angles and with complex topologies, causing topological defects, geometric errors and local connectivity flaws on mesh models.

1.6 Geological packages and meshing

In terms of geological models in basin/reservoir scale, geological packages have provided an intuitive way of visualize stratum and fault structures. Although some of these packages can generate meshes for geological models, they do not have functions to handle structures with complicated constraints. In this section, several geological suites are introduced and capacities of current mesh generation methods based on geological models are discussed.

Geological packages have been developed and widely used for decades to meet the request of geologists in modelling geographic information system (GIS), geostatistical analysis, seismic depth conversion, visualization, and property modelling. Interpolation and intersection engines are widely employed in these packages to deal with complicated fault systems. Several of the most popular geological suites are introduced as below. (1) GoCAD (<http://www.gocad.org>) is one of the most popular geological software. It provides customers high flexibility to depict complex geo-objects [141, 142]. A number of studies [142-144] have benefited from its geometry handling ability as well as various data formats. (2) 3D Geomodeller (<http://www.geomodeller.com>) is a popular geological modelling software, which is developed by BRGM (French Geological Survey) and commercialized by Intrepid Geophysics. It directly uses geological observation data to construct models and automatically constructs intersections and volumes of geo-objects [145, 146]. (3)

GSi3D (<http://gsi3d.org>) developed by the British Geological Survey is a methodology and associated software for geological modelling [147, 148]. In this suite, cross sections are required to be established in a structured manner to construct staggered geological surfaces. (4) Move (<http://www.mve.com>) by Midland Valley Software focuses on designing structural geology models. It is a modelling and analysis toolkit, which is with functions such as structurally constrained static modelling, kinematic analysis, deterministic modelling, as well as process modelling. (5) Petrel (<http://www.slb.com>) by Schlumberger is widely used in petroleum industry for accurate, high-resolution geological modelling of the reservoir structure and stratigraphy. It has sophisticated capabilities in generating well correlation panels, performing traditional mapping, plotting techniques as well as 3D reservoir modelling. A geological model created by Petrel is shown in Figure 1.4.

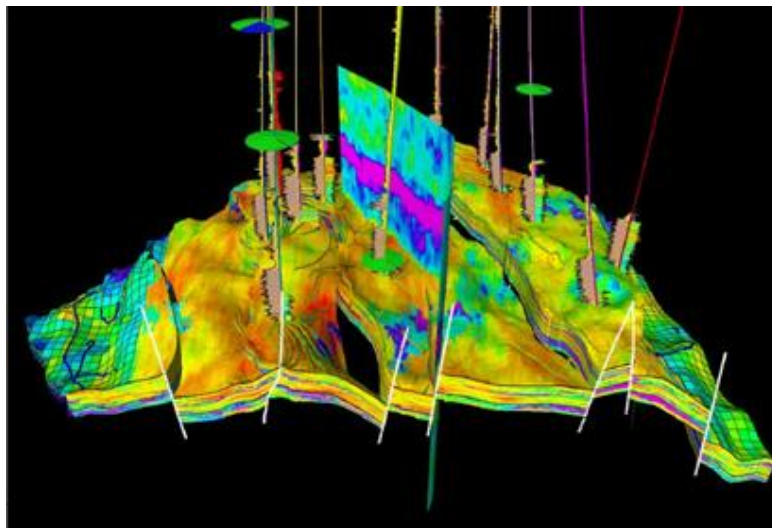


Figure 1.4: A geological model created by Petrel (<http://www.slb.com>)

Computer Aided Engineering (CAE) systems always provide well developed meshing functions for applications in mechanical engineering, but it cannot be applied to model geo-objects. Unlike the mechanical parts which consist of regular shapes, geo-objects include: complex geometry and topology, vague boundaries/interfaces defined by spatial variations and anisotropy of most subsurface features [2] (see Figure 1.4). Furthermore fault systems involved in basin/reservoir scale models compound the difficulties present in the corresponding mesh generation. Most geological numerical simulation software such as CMG (<http://www.cmgl.ca>), ECLIPSE (<http://www.slb.com>), FLAC3D (<http://www.itascacg.com>) et al. are based on finite difference methods using structured mesh models. However, structured meshes cannot adequately describe complicated structures (e.g. fault systems) especially in stress analysis, which limit applications of geological packages. Therefore, unstructured mesh generation is in high demand for description of complex geo-objects. Courrioux et al. [149] developed a volumetric reconstruction method for

modelling the main domains of the Cadomian collisional orogenic belt of Panafrican age in Northern Brittany (France). Wu et al. [150, 151] focused on constructing models from geological data which are generally sparse and undersampled. They applied the modelling method with data from boreholes, cross-sections, geological maps, etc. and generated meshes for complex faults through lag insertion and local reconstruction. Riard et al. [151] proposed an implicit approach to handle unconformities in restoration for eroded surfaces and onlap layer geometries. They showed how their approach could generate less mesh elements than the conforming mesh. Liu et al. [152, 153] studied the method of preserving line constraints within the process of quadrilateral mesh generation and applied it to create mesh models for fault systems. Overall there is still a lack of effective unstructured mesh generation methods for current geological packages, which restricts the capability of FEM-based simulations in geology.

1.7 Remeshing in geocomputing

In geological modelling, remeshing is utilized to achieve modifications of the mesh geometry and topology, which is an essential technique for simulation of dynamic processes in geological engineering. Remeshing for geological modelling is challenging since constraints such as stratum interfaces and faults increase its difficulties. We will discuss issues related to remeshing in geocomputing further in this section.

With the development of geological modelling and computing techniques, the geological structure of reservoirs can be described in more detail and the corresponding numerical simulations allow for better engineering of the processes ahead of design [2]. Remeshing has been studied for decades to simulate large deformation and crack propagation by finite element method applications [154-159]. However, it is still quite challenging when applied to geological models. This is mostly because geological mesh models with strata are different from traditional meshes with uniform material properties. Geological mesh models contain stratum interfaces which need to be clearly represented and preserved as interior constraints at any step of the numerical simulation. Besides, element size gradation on a geological model should be maintained and extended on the corresponding stratum interfaces in the remeshing process.

3D geological models have gained significant interest because of the rise of complex construction projects and natural hazard assessments which utilize them [2]. Due to the structural heterogeneity of the strata, triangular meshes are often used to represent stratum interfaces, which can accurately

construct geological models concerning visualization and numerical simulation for geo-science and geo-engineering. Frank et al. [160] developed an implicit triangular surface reconstruction method for complex geological interfaces such as horizons and salt domes. Durand-Riard et al. [161] focused on preserving stratum interface constraints and achieved a balanced restoration of geological volumes by a finite element method. Xing and Liu [162] proposed a method to generate surface meshes from voxel data and achieved meshing 3D geological reservoirs with arbitrary stratigraphic surface constraints. However, all the above algorithms are static mesh generation which are not suitable for simulate dynamic processes in petroleum and coal engineering.

In terms of simulation drilling and caving processes in geo-engineering, remeshing techniques are required to couple with finite element applications. During the last two decades, a number of remeshing algorithms [154-159] have been developed for simulating metal forming processes and fracture propagations. The research includes large deformation [154, 155], crack tips prediction [156, 157], remeshing error estimation [158, 159, 163] etc. Although the above methodologies provide excellent solutions for damage and crack simulation in mechanical engineering, they are not suitable for numerical simulations in geology due to the maintenance requirement of stratum interfaces. Braun and Sambridge [164] included the strata and proposed a dynamical Lagrangian remeshing approach to simulate large strain and apply the algorithm to fault-propagation folding. They preserved strata by attaching material properties on nodes and without changing the number of nodes during the remeshing process. The drawback of this method is the lack of the ability to adaptively remesh the area of interest with different element size and node density. Wang et al. [165] provided a soil interface conforming mesh refinement method for geological structures. The method could automatically insert extra nodes in problem domains while preserving soil interfaces. However, there are two limitations of this approach: there is no theoretical guarantee of adaptive features and it is difficult to extend to 3D. Pellerin et al. [166] proposed an automatic surface remeshing for 3D geological structural models. Concerning geological structures very close to each other, they locally inserted sufficient nodes to describe corresponding features. Globally, a centroidal Voronoi optimization is employed to generate mesh with high quality elements. It is noteworthy that the surface remeshing they proposed is used for subsequent volumetric meshing thus not a comprehensive approach for dynamic geo-engineering processes such as drilling and caving. Indeed, adaptive remeshing for 3D geological structures is challenging and it is necessary to develop an effective remeshing approach for both geo-engineering and geo-science.

1.8 Summary of findings

With the development of computational geo-science and geo-engineering, the mesh generation and its applications are increasingly important in studying geomechanical behaviours as well as coupled geomechanical and flow processes. Based on the above literature review, the problems in meshing for geological modelling are listed as below:

- For 2D domains using quadrilateral mesh generation with arbitrary line constraints, it is still difficult to construct well-aligned elements parallel to the constraints.
- Fractures in rocks are complex. Meshes generated by contemporary image meshing techniques have a large data set and cannot be utilized in FEM-based applications. So far, there is not an acceptable mesh method for generating a representation with a small data set for fractures.
- Hexahedral meshes have difficulty with mesh generation for rocks and representing complex geometries and tetrahedral meshes are highly reliant on the quality of the surface mesh in describing fracture structures. However, adequate surface mesh generation for fractures is difficult, as fractures can meet with each other at arbitrary angles with complicated topological structures.
- Unstructured meshes are better than structured meshes in terms of describing complicated geometries. The lack of effective unstructured mesh generation functions limits applications of contemporary geological packages.
- In simulations of dynamic processes in geo-engineering, remeshing with the preservation of stratum interfaces is still challenging.

In general, it is essential to develop a meshing system which can interface between geological data and numerical simulations in geology. Therefore, this thesis is focused on developing such a meshing system and providing solutions for the above problems. For 2D domains, a quadrilateral mesh generation method based on geodesic isolines is developed to create layers of well-aligned elements parallel to line constraints. With regard to fractures in rocks, a simplified Voronoi diagram based on a proposed pseudo-surface assumption is proposed to extract fractures, identify fracture junctions and generate high-quality mesh models with small data size. Concerning reservoir models generated by geological suites, a geodesic-based procedure is designed to provide a robust

implementation for handling geometrical heterogeneity on stratigraphic surfaces and generating unstructured meshes. Additionally, a 3D remeshing approach conforming to stratum interfaces is developed for simulation of dynamic geo-engineering processes by finite element applications.

1.9 Thesis Outline

The following presentation of this thesis is divided into six chapters. Chapter 2 describes a 2D image meshing algorithm. The emphasis of the algorithm is generating high-quality quadrilateral elements constrained by the material interfaces. Chapter 3 focuses on the development of 3D rock image meshing techniques. The sheet-like structure extraction method and the fracture surface mesh generation strategy are proposed and developed respectively. Chapter 4 provides a solution for generating unstructured meshes for reservoir models from static geological modelling software. Chapter 5 proposes an adaptive remeshing approach for geological structure with stratum interface constraints. Finally, conclusions and future work based on the above outcomes are drawn in Chapter 6.

Chapter 2 Two-Dimension Mesh Generation for Heterogeneous Rock

2.1 Overview

Digital images are nowadays widely accepted and used in many areas to describe the complicated structures within heterogeneous rocks. Researchers are always interested in convert digital images to analysable meshes which can be utilized in finite element/volume simulations [1, 13, 16, 167]. Concerning mesh generation for heterogeneous rock there are two difficulties: (1) heterogeneous rock in reality have complex material boundaries and (2) it is hard to generate layers of well-aligned elements parallel to the boundaries.

In this chapter, section 2.2 is a published paper describing a boundary focused quadrilateral mesh generation method, which is developed to produce high-quality mesh models for 2D heterogeneous rock. In the paper, a phase-based boundary smoothing method is proposed to remove jagged features and smooth material boundaries. Geodesic isolines are employed to indirectly generate well-aligned elements parallel to material boundaries. Moreover, a valence clear-up pattern Pisces is designed to improve the element quality.

Based on the numerical applications, the proposed method has been proven that it has more advantages in generating high-quality elements over algorithms developed by Park et al. [168] and Lee et al.[43]. Besides, the method is applied to generate mesh for images of a coal plug and a fractured rock, which demonstrates its effectiveness of handle data from practice.

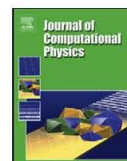
2.2 The paper

A boundary focused quadrilateral mesh generation algorithm for multi-material structures

Yan Liu, H.L. Xing

Journal of Computational Physics

Volume 232, Issue 1, 1 January 2013, Pages 516-528



A boundary focused quadrilateral mesh generation algorithm for multi-material structures

Yan Liu, H.L. Xing*

Earth Systems Science Computational Centre (ESSCC), School of Earth Sciences, The University of Queensland, St. Lucia, QLD 4072, Australia

ARTICLE INFO

Article history:

Received 12 October 2011

Received in revised form 16 June 2012

Accepted 23 August 2012

Available online 6 September 2012

Keywords:

Quadrilateral mesh

Multi-material

Material boundary

Digital image

Line constraint

Boundary smoothing

ABSTRACT

This paper describes a new boundary focused mesh generation algorithm. The algorithm produces quadrilateral meshes from images of multi-material structures. The challenge of meshing such images is to create high quality elements which are aligned with complex material boundaries. The approach proposed in this paper uses the following steps: (1) extract boundaries according to pixel colours; (2) smooth the jagged boundaries; (3) generate geodesic isolines aligned with smoothed boundaries; (4) generate a mesh from the boundaries and isolines; (5) optimize the mesh using the “Pisces” pattern (which is introduced in this paper). Application examples are presented to contrast the reliability and effectiveness of the new algorithm with existing approaches.

© 2012 Elsevier Inc. All rights reserved.

1. Introduction

With the development of advanced imaging technology such as computed tomography (CT) and magnetic resonance imaging (MRI), digital data are nowadays widely accepted and used in many areas to describe the complicated multi-material structures with multiple colours, such as in mining [1], medicine [2] and material science [3]. Methods [4–9] for meshing images have been studied in both 2D and 3D to convert the imaging data into finite element models for finite element/finite volume simulations [10–13]. However, these mesh methods usually focus on generating meshes inside the objects rather than creating high quality elements aligned with the boundaries. Since finite element analysis of mechanical behaviour is quite sensitive to element quality and shape especially along material boundaries. Poor quality boundary elements could lead to errors and crashes in numerical simulations [14,15]. For instance, boundaries between different materials are major sources of fracture. Hence they require high quality elements and well-aligned features to address such behaviours [16,17]. Therefore, the goal of this paper is to present a boundary focused quadrilateral mesh generation algorithm and evaluate it in meshing complicated multi-material structures based on image data.

Image-based finite element mesh construction is the subject of on-going research. The simplest way to build quadrilateral meshes from images is to use pixel models [18,19]. However, the drawbacks of this method are evident, jagged boundaries lead to poor results, even errors in simulations [8,20]. To remove such jagged features, methods such as marching cubes [21] and level set [4] are sometimes adopted to create smoothed material boundaries for further mesh generation. Based on these boundaries Zhang et al. [5,7] employed quadtree/octree methods to create meshes for multi-material image data in both 2D and 3D. However, in the generated meshes, element quality around boundaries is poor and there are no aligned elements parallel to the boundaries. Zhang et al. [22] proposed a surface smoothing method to improve element quality. But their

* Corresponding author. Tel.: +61 7 33464093; fax: +61 7 33464134.

E-mail addresses: y.liu8@uq.edu.au (Y. Liu), h.xing@uq.edu.au (H.L. Xing).

method has no contribution to generating aligned features in meshes. One method for producing both high quality elements and well-aligned features is “paving” proposed by Blacker and Stepheson [23]. “Paving” forms complete rows of quadrilaterals starting from the boundaries and moving into the interior. The main drawback of paving is the difficulty of resolving the intersection of two fronts which are likely to be overlapped with each other. The detection and resolution of the intersection is time-consuming and complicated. To address these problems, Lee et al. [24] extended Q-Morph [25] to generate quadrilaterals for domain with line constraints. The Q-Morph-based methods maintain the desirable features around boundaries. But they require an existing triangular mesh with a sufficient density to capture the model features; otherwise it will have the same problem as the paving method. Park et al. [26] proposed a direct quadrilateral meshing method to generate meshes with random line constraints. But they still encountered the same difficulty of “paving”. To overcome this difficulty, Liu et al. [27] proposed a robust quadrilateral mesh generation method. Based on the Catmull-Clark subdivision [28], it could automatically generate meshes with high quality elements comparable to the Catmull and Clark [28] approach. However, elements around boundaries are still in poor quality and without well-aligned features.

In summary, the current challenge of image-based quadrilateral mesh generation is how to robustly generate high-quality elements for complex multi-material structures especially aligned with material boundaries. To address this issue, a novel boundary focused quadrilateral mesh generation method for multi-material structures is proposed which includes image-based boundary extracting, smoothing, quadrilateral mesh generating and irregular nodes removing. The proposed method is outlined in the following three steps:

- (1) Boundary smoothing: a phase-based boundary smoothing method is employed to smooth jagged boundaries.
- (2) Quadrilateral mesh generation: geodesic isolines are utilized to generate mesh which includes several layers of well-aligned elements parallel to the smoothed boundaries.
- (3) Quadrilateral mesh optimization: a general pattern named “Pisces” is proposed to decrease the number of irregular nodes. It covers most of the specified patterns proposed by authors in Liu et al. [27].

This paper is organized as follows: In Section 2, material boundary (i.e. interface between different colours) smoothing as well as quadrilateral mesh generation and optimization are described. Then in Section 3 application examples are illustrated to show the effectiveness of our approach. Finally, conclusions are given in Section 4.

2. Proposed algorithms and implementation

Boundaries distinguishing different colours (i.e. materials) are important features in numerical simulation. To extract these boundaries, samples between different pixels are created and a multiply material marching cubes algorithm [21] is utilized to generate material boundaries through connecting these samples. The proposed meshing approach starts from these extracted material boundaries.

2.1. Boundary smoothing

Due to the nature of images, the extracted boundaries are usually jagged. As these jagged boundaries affect the element quality of generated quadrilateral meshes, a smoothing approach is proposed to remove the jagged features in a phase by phase manner.

Through the linear least squares method, a phase of a boundary line is described by a quadratic function $f(x) = a + bx + cx^2$. Supposing samples S_{i-1} , S_i and S_{i+1} are sequent on this line, the coordinates of node S_{i-1} and S_{i+1} are x_{i-1}, y_{i-1} and x_{i+1}, y_{i+1} respectively. The location of S_i is optimized by the following equations:

$$\begin{cases} f(x) = a + bx + cx^2 \\ g(x) = \frac{y_{i-1} + y_{i+1}}{2} - \frac{x_{i-1} - x_{i+1}}{y_{i-1} + y_{i+1}} \left(x - \frac{x_{i-1} + x_{i+1}}{2} \right) \\ x_{i-1} < x < x_{i+1} \end{cases} \quad (1)$$

where $g(x)$ is the perpendicular bisector of the segment $S_{i-1}S_{i+1}$.

To demonstrate the proposed phase-based boundary smoothing method, a jagged boundary (Fig. 1(a)) is utilized. Before describing this method, thresholds are introduced to control the process of finding phases: the maximum number of samples on the phase N and the maximum angle between the first and last edge vectors of the phase Ang . We take $N = 6$ and $Ang = \pi/2$ in this paper.

As shown in Fig. 1(b), and the previous smoothed boundary phase consists of samples from a to b . To find a new phase, the sample (i.e. sample c) between a and b is used as the start. And then the new phase is propagated sample by sample until there are N samples or the angle between the first and last edge vectors is larger than Ang . In Fig. 1(b), \vec{u} is the first edge vector and \vec{v} is the last one. Although the angle between \vec{u} and \vec{v} is less than Ang , the propagating process is stopped as d is the sixth sample. The current phase consists of samples from c to d . Eq. (1) is employed to smooth this phase as shown in Fig. 1(c). The final smoothed boundary is illustrated in Fig. 1(d).

The phase-based boundary smoothing method is described as below.

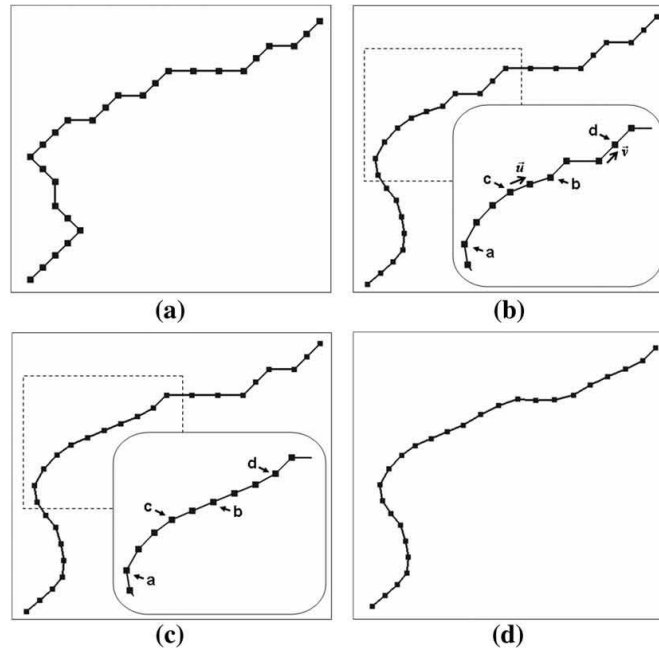


Fig. 1. The phase-based boundary smoothing method: (a) a jagged boundary; (b) finding a new phase; (c) the result of smoothing the new phase; (d) the result of smoothing the whole jagged boundary.

Phase-based boundary smoothing method

$\{s_i; i = 1, 2, \dots, n\}$ is a jagged boundary where s_i are samples on it.

N is the threshold of phase sample number.

Ang is the threshold of the angle between the first and last edge vectors.

i is the current index initialized as "0".

- Step 1: Push s_i into a queue Q . Take $\overrightarrow{s_i s_{i+1}}$ as the first edge vector \vec{u} .
- Step 2: $\overrightarrow{s_i s_{i+1}}$ is the last edge vector \vec{v} .
IF $i + 1 > n$ **OR** the size of Q equals N **OR** the angle between \vec{u} and \vec{v} is larger than Ang
THEN GOTO Step 4.
END IF
- Step 3: $i = i + 1$, and push s_i into Q . **GOTO** Step 2.
- Step 4: **IF** the size of Q is larger than 2
THEN smooth the samples in Q through Eq. (1)
END IF
- Step 5: $i = i + \lfloor N/2 \rfloor$.
IF $i > n$
THEN GOTO Step 6
ELSE GOTO Step 1
END IF
- Step 6: Output the smoothing result.

2.2. Quadrilateral mesh generation

Definitions:

Node valence: the number of edges connected with the node.

Regular node: an inner node whose valence is four.

Irregular node: an inner node whose valence does not equal four.

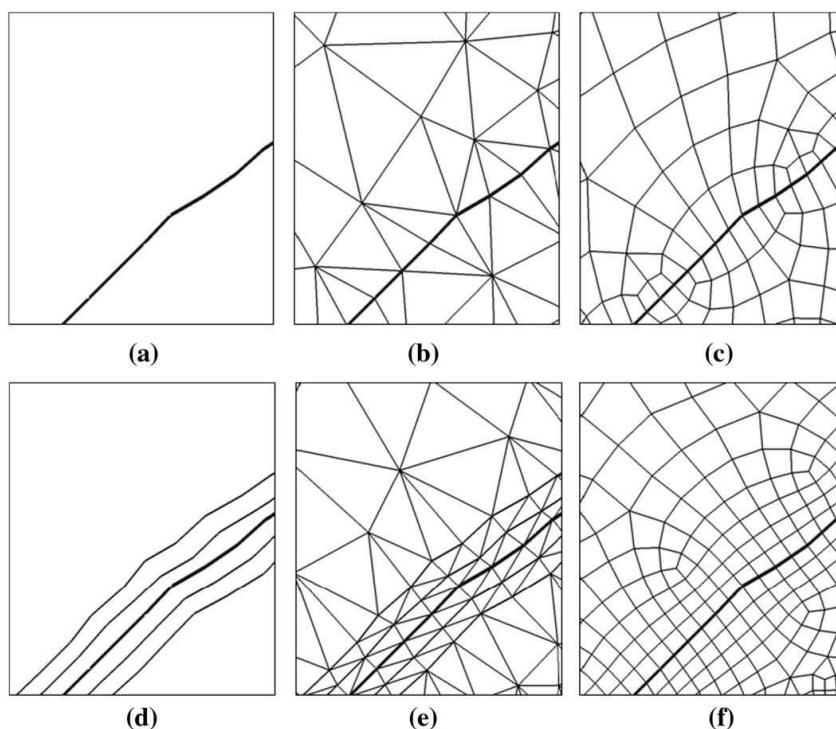


Fig. 2. Quadrilateral mesh generation: (a) is a line constraint; (b) and (c) are the triangular and quadrilateral meshes according to (a); (d) is the line constraint with geodesic isolines; (e) and (f) are the triangular and quadrilateral meshes according to (d).

The mesh generation method proposed in this paper is an extension of the work of Liu et al. [27]. A simple example in Fig. 2(a) is utilized here to demonstrate the improvement.

Concerning the method proposed by Liu et al. [27], it takes the boundary in Fig. 2(a) as a line constraint, then generates an initial triangular mesh, as shown in Fig. 2(b). In the next step, a quadrilateral mesh is created in Fig. 2(c). As the element sizes around the boundary are smaller than the one in the mesh inner, a number of irregular nodes exist in the transitional areas (i.e. vicinity of the boundary). These nodes significantly affect the element quality around the boundary.

The method proposed in this paper employs geodesic isolines [29–31] to improve element quality as well as generate well-aligned boundary elements. Specifically, two layers of geodesic isolines (Fig. 2(d)) are built around the boundary in Fig. 2(a). In the next step, the corresponding triangular mesh is generated (Fig. 2(e)). Finally, a quadrilateral mesh (as shown in Fig. 2(f)) is created with well-aligned features parallel to the boundary. Comparing with Fig. 2(c), the number of irregular nodes close to boundaries is decreased and the quality of corresponding elements is improved (Fig. 2(f)).

2.3. Quadrilateral mesh optimization

A pattern named “Pisces” is proposed here to further improve the local mesh topological structure. It is a general pattern with levels and covers most of the specified patterns proposed by authors in Liu et al. [27].

Before introducing the Pisces pattern three criteria are illustrated: (1) performing Pisces pattern only if it reduces the number of irregular nodes; (2) performing Pisces pattern only if no generated quadrilateral has an inner angle larger than π ; (3) the removing of line constraints is prohibited.

To introduce Pisces pattern, “fish” is firstly described in Fig. 3(a). One side fish has a three-valence node, which is called the head of fish. And the other side is called tail. A Pisces consists of two fishes with opposite directions as illustrated in Fig. 3(b). The length of a Pisces is defined as the number of quadrilaterals between head and tail of one fish. And the width of a Pisces is defined as the number of quadrilaterals between head of one fish and tail of the other one. The level of a Pisces is defined as $level = width - 2$, which starts from 0 and has no upper bound. For instance, the length, width and level of the Pisces in Fig. 3(b) are five, four and two respectively.

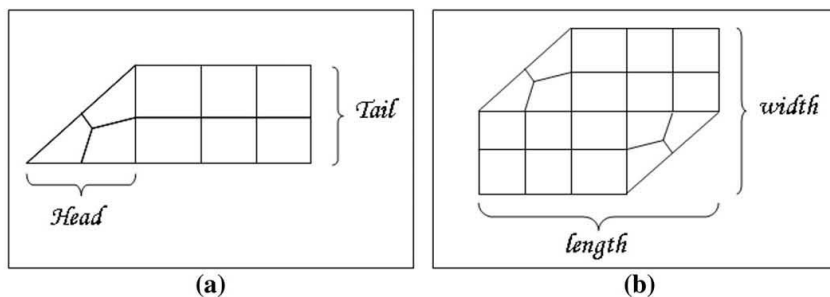


Fig. 3. Fish and Pisces: (a) fish; (b) Pisces.

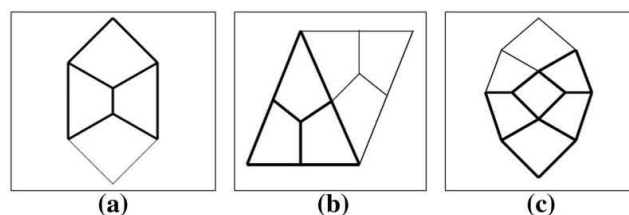


Fig. 4. Specified patterns in Liu et al. [27].

Pisces pattern is such a general pattern that most specified patterns proposed in Liu et al. [27] could be categorized into its particular levels. Fig. 4 demonstrates the patterns in Liu et al. [27]. To be clear, one fish of the Pisces is described in bold lines. Fig. 4(a) is the local mesh case 2 of Liu et al. [27], which can be categorized into level-0 Pisces. The local mesh case 3 of Liu et al. [27] (Fig. 4(b)) is a level-2 Pisces. And Fig. 4(c) is the local mesh case 4 in Liu et al. [27], which is level-1 Pisces with a fish-length of 3.

Pisces with levels from 0 to 3 are illustrated in Fig. 5(a)–(d) respectively. Pisces pattern reconnects Pisces to construct $length \times level$ quadrilaterals. Results of Pisces patterns for Pisces level 0–3 are illustrated in Fig. 6(a)–(d) respectively.

Specifically, level-0 Pisces pattern has another two reconnection modes. As shown in Fig. 7(a) and (b), the two reconnection modes for the level-0 Pisces pattern in Fig. 6(a) are illustrated.

3. Numerical applications

The meshing method in this paper is designed for multi-material images with complex boundaries. Examples are presented as below to compare with some existing approaches and describe the proposed method in detail.

Examples with artificial line constraints are firstly illustrated. As shown in Fig. 8, six segments and a square hole are utilized as constraints. Fig. 8(a) created by Lee et al. [24] includes 44 irregular inner nodes, while Fig. 8(b) result of the proposed method has only 15 irregular inner nodes. Obviously, the mesh generated by the proposed method is better than the one created by Lee et al. [24]. Fig. 9(a) and (b) are quadrilateral meshes generated by Park et al. [26] and the proposed method respectively. Fig. 9(b) performs better aligned elements than Fig. 9(a) referring to the constraint lines. And the statistic data in Table 1 proof that the proposed method is more effective than Park et al. [26] to generate high-quality elements for domain with complex line constraints.

In practice, a digital image of a cracked rock and a close-up with jagged boundaries are illustrated in Fig. 10(a). According to the pixel colours, boundaries are extracted and constructed in the form of segments as shown in Fig. 10(b). To smooth these jagged boundaries, the phase-based boundary smoothing method is employed and the smoothed result is illustrated in Fig. 10(c).

Taking Fig. 10(a) as input, the quadrilateral mesh generation result of Catmull and Clark [28] and Liu et al. [27] are illustrated in Fig. 11(a) and (b). And their close-ups are shown in Fig. 11(c) and (d) respectively. Both of them perform poor-quality elements in the vicinity of boundaries. However, the algorithm proposed in this paper has high element quality and well-aligned features around the boundaries compared with the above two methods. And it is demonstrated step by step in the same close-up area. Firstly, instead of jagged lines, smoothed ones are utilized to describe boundaries between different colours and the corresponding quadrilateral mesh is shown in Fig. 11(e). Then, to improve the element quality around

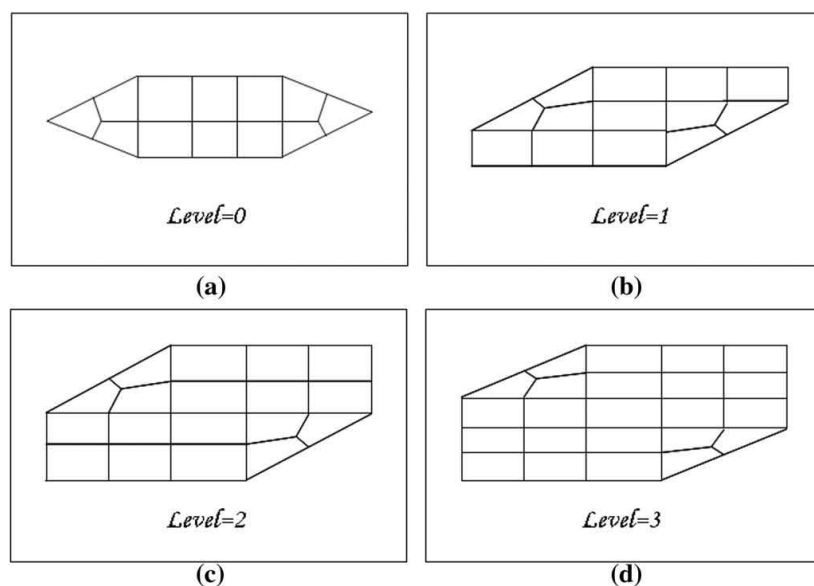


Fig. 5. Pisces patterns with different levels (a) 0; (b) 1; (c) 2 and (d) 3.

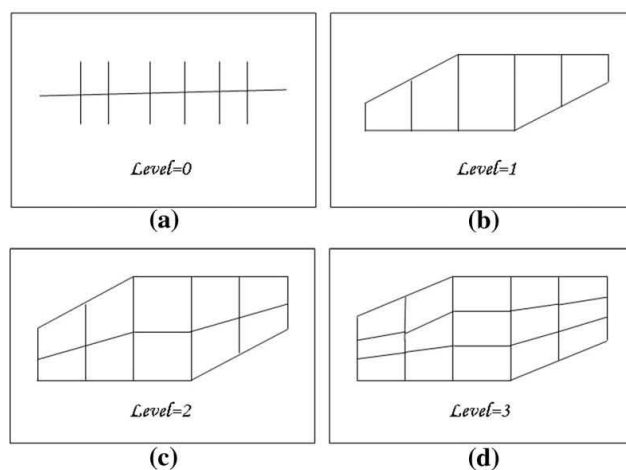


Fig. 6. Optimised mesh for the Pisces pattern as detailed in Fig. 5 with different levels (a) 0, (b) 1, (c) 2 and (d) 3.

boundaries, geodesic isolines are employed to generate layers of the quadrilateral mesh with well-aligned features as shown in Fig. 11(f). Finally, Pisces patterns are utilized to decrease the number of irregular nodes as shown in Fig. 11(g). The entire quadrilateral mesh of Fig. 11(g) is illustrated in Fig. 11(h).

As this paper focuses on generating well-quality quadrilateral elements around boundaries, in quality statistics, a quadrilateral is counted only if the distance between its centroid and the boundaries is less than 3-pixel length. The minimum and maximum inner angles and the valence of inner nodes are utilized to analyse quadrilateral meshes generated by different methods based on the image of Fig. 10(a). As shown in Fig. 12(a), compared with Catmull and Clark [28] and Liu et al. [27], the proposed method generates more quadrilaterals with the minimum inner angles between 70° and 90° . As shown

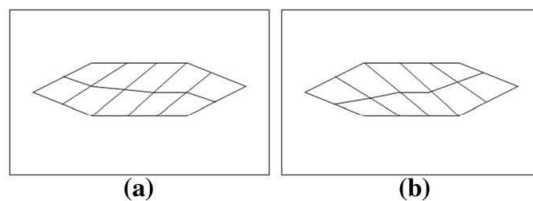


Fig. 7. Another two reconnection modes for level-0 Pisces pattern.

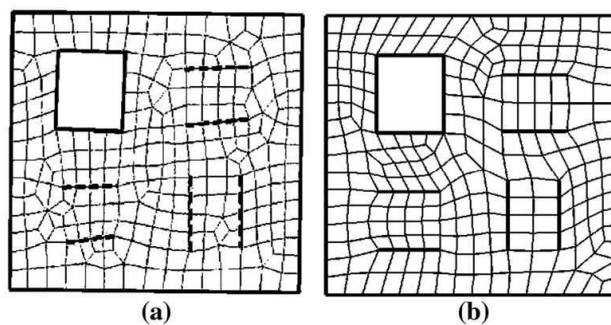


Fig. 8. Mesh comparison between Lee et al. [24] (a) and the proposed method (b). Bold lines are the constraints and borders.

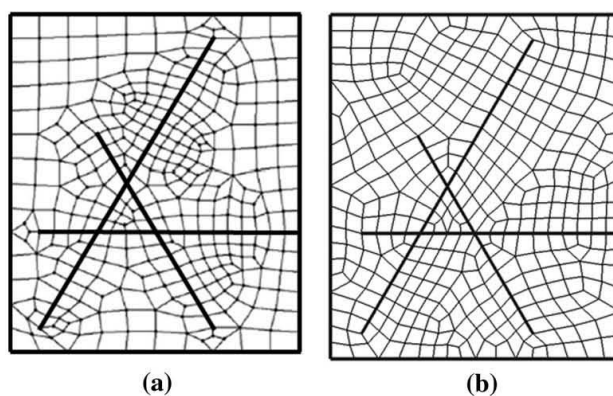


Fig. 9. Mesh comparison between Park et al. [26] (a) and the proposed method (b). Bold lines are the constraints and borders.

Table 1
Element quality comparison.

	Park et al. [26] Fig. 9(a)	The proposed method Fig. 9(b)	Case of exact square mesh
Distortion	0.67	0.71	1
Uniformity	1.19	1.11	1
Aspect ratio	1.18	1.16	1
Taper degree	0.81	0.91	1
Skewness	13.08	11.32	0

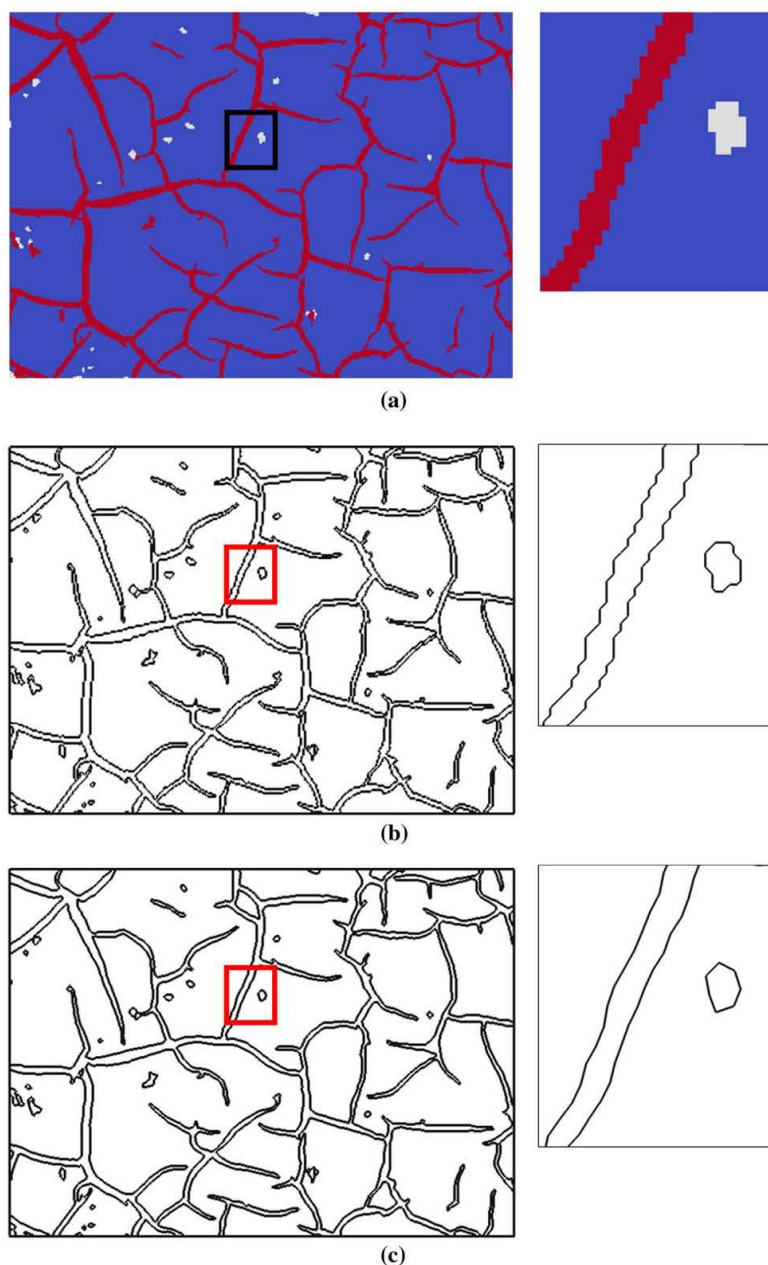


Fig. 10. Boundary smoothing: (a) the original image; (b) the extracted boundaries; (c) the smoothed boundaries.

in Fig. 12(b), in terms of quadrilateral maximum inner angles, the result of the proposed method is also better than Catmull and Clark [28] and Liu et al. [27]. Regarding to the percentage of regular inner nodes (whose valence is four) in the entire quadrilateral mesh, the result of proposed method is proximate 90% while it is 75% in Liu et al. [27] and 50% in Catmull and Clark [28], as shown in Fig. 12(c).

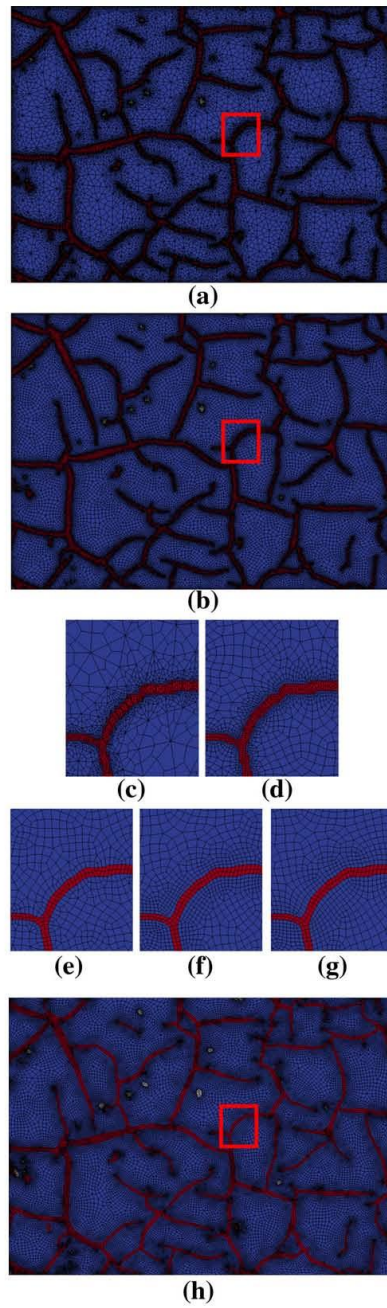


Fig. 11. Quadrilateral mesh generation for a cracked rock image: (a) the mesh generated by Catmull and Clark [28]; (b) the mesh generated by Liu et al. [27]; (c) a close-up of (a); (d) a close-up of (b); (e)–(g) are meshes of the proposed method in the close-up area; (h) the mesh generated by the proposed method.

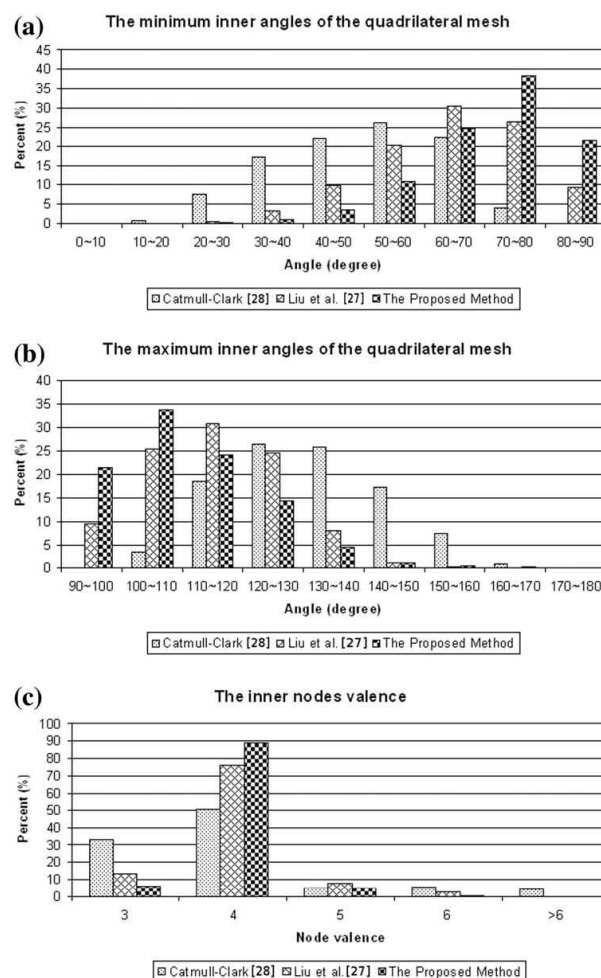


Fig. 12. Element quality: (a) the minimum inner angles; (b) the maximum inner angles; (c) the inner nodes valence.

Another application example is utilized to illustrate the proposed method. A slice of a coal stick with crack lines is shown in Fig. 13(a) and its close-up is in Fig. 13(e). Fig. 13(b) and (c) are the quadrilateral mesh result of Catmull and Clark [28] and Liu et al. [27] respectively. Fig. 13(d) is the result of the proposed method. Close-ups of these three quadrilateral meshes are shown in Fig. 13(f)–(h) respectively. It is evident that the result of proposed method is better than Catmull and Clark [28]. Compared with Liu et al. [27], although there is no significant difference in a global view, in the area around boundaries, the mesh in Fig. 13(h) generated by the proposed method performs better aligned features than the one in Fig. 13(g) generated by Liu et al. [27]. The difference of element quality around boundaries (in 3-pixel length) among Catmull and Clark [28], Liu et al. [27] and the proposed method are illustrated in Fig. 13(i) and (j). Their inner node valence statistics are shown in Fig. 13(k).

4. Conclusion

This paper proposes an automatic quadrilateral mesh generation algorithm for multi-material structures. The examples demonstrate its effectiveness and robustness. Therefore, the following conclusions are drawn:

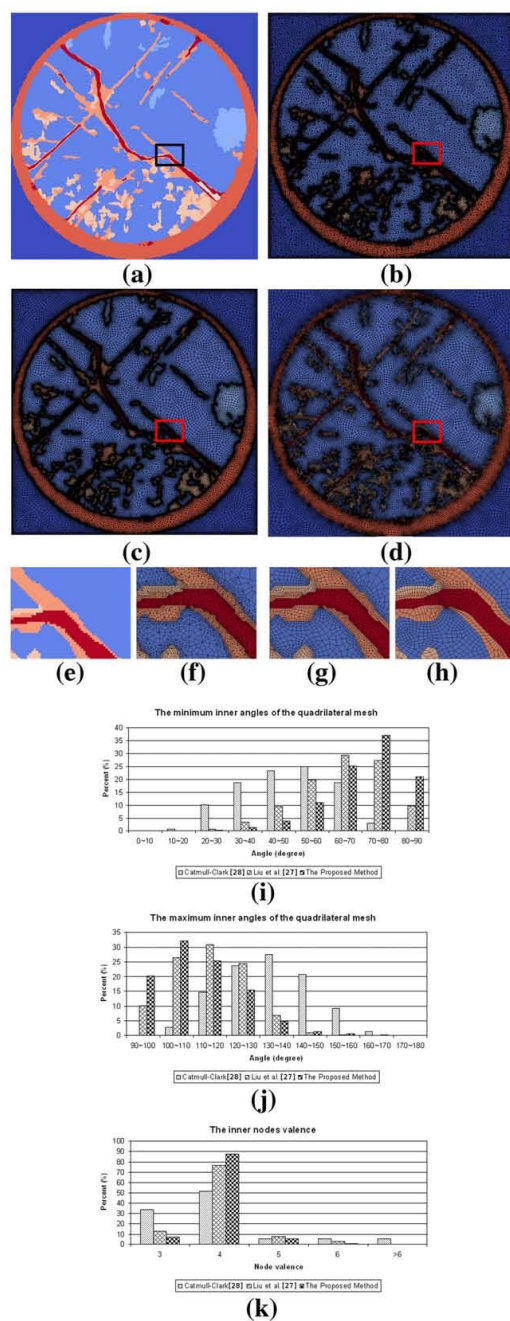


Fig. 13. A slice of a coal stick: (a) the original image; (b) the mesh generated by Catmull and Clark [28]; (c) the mesh generated by Liu et al. [27]; (d) the mesh generated by the proposed method; (e)–(h) are close-ups for (a)–(d) respectively; (i) the minimum inner angles; (j) the maximum inner angles; (k) the inner nodes valence.

- (1) The proposed phase-based smoothing process and geodesic-isoline-aided meshing approach significantly improves the element quality and creates layers of well-aligned elements around complex image boundaries.
- (2) The Pisces valence clear-up pattern proposed in this paper, is effective in reducing the number of irregular inner nodes and improving the element quality across the mesh including close to the boundaries.
- (3) The proposed quadrilateral mesh generation method can generate higher quality elements than the methods of Lee et al. [24] and Park et al. [26]. Additionally, it is more effective in improving element quality around material boundaries than the methods of Liu et al. [27] and Catmull and Clark [28], since it generates more high-quality elements and more regular inner nodes.

Future work could include extending the method to 3D surface mesh construction based on parameterization approaches [32], as well as using the idea of indirect mesh generation to achieve hex-tet hybrid volume meshing for 3D digital images.

Acknowledgements

The authors are grateful to Dr Jianping Zuo from China University of Mining and Technology for providing the think section image data used in this paper. Support is gratefully acknowledged by the Australian Research Council (Grant No. ARC-LX0989423 and ARC DP110103024).

References

- [1] W. Xu, Z. Yue, R. Hu, Study on the mesostructure and mesomechanical characteristics of the soil-rock mixture using digital image processing based finite element method, *International Journal of Rock Mechanics and Mining Sciences* 45 (2008) 749–762.
- [2] R. Hambli, Multiscale prediction of crack density and crack length accumulation in trabecular bone based on neural networks and finite element simulation, *International Journal for Numerical Methods in Biomedical Engineering* 27 (2011) 461–475.
- [3] L.L. Mishnaevsky, Automatic voxel-based generation of 3D microstructural FE models and its application to the damage analysis of composites, *Materials Science and Engineering: A* 407 (2005) 11–23.
- [4] G. Legrain, P. Cartraud, I. Perreard, N. Moës, An X-FEM and level set computational approach for image-based modelling: application to homogenization, *International Journal for Numerical Methods in Engineering* 86 (2011) 915–934.
- [5] Y. Zhang, T.J.R. Hughes, C.L. Bajaj, An automatic 3D mesh generation method for domains with multiple materials, *Computer Methods in Applied Mechanics and Engineering* 199 (2010) 405–415.
- [6] A.C.E. Reid, S.A. Langer, R.C. Lua, V.R. Coffman, S.J. Haan, R.E. García, Image-based finite element mesh construction for material microstructures, *Computational Materials Science* 43 (2008) 989–999.
- [7] Y. Zhang, C. Bajaj, Adaptive and quality quadrilateral/hexahedral meshing from volumetric data, *Computer Methods in Applied Mechanics and Engineering* 195 (2006) 942–960.
- [8] J.H. Kim, M.G. Lee, R.H. Wagoner, A boundary smoothing algorithm for image-based modeling and its application to micromechanical analysis of multi-phase materials, *Computational Materials Science* 47 (2010) 785–795.
- [9] H. Xing, Y. Liu, Automated quadrilateral mesh generation for digital image structures, *Theoretical and Applied Mechanics Letters* 1 (2011) 061001.
- [10] S.J. Owen, A survey of unstructured mesh generation technology, in: *The Seventh International Meshing Roundtable*, Dearborn, MI, USA, 1998, pp. 239–267.
- [11] H. Zhang, W. Xu, S. Di, P. Thomson, Quadratic programming method in numerical simulation of metal forming process, *Computer Methods in Applied Mechanics and Engineering* 191 (2002) 5555–5578.
- [12] H. Xing, W. Yu, J. Zhang, 3D Mesh Generation in Geocomputing, in: *Advances in Geocomputing*, Springer-Verlag GmbH, 2009, pp. 27–64.
- [13] H. Xing, A. Makinouchi, P. Mora, Finite element modeling of interacting fault systems, *Physics of the Earth and Planetary Interiors* 163 (2007) 106–121.
- [14] P. Wang, Modeling material responses by arbitrary Lagrangian Eulerian formulation and adaptive mesh refinement method, *Journal of Computational Physics* 229 (2010) 1573–1599.
- [15] Z. Li, M.W. Kindig, D. Subit, R.W. Kent, Influence of mesh density, cortical thickness and material properties on human rib fracture prediction, *Medical Engineering & Physics* 32 (2010) 998–1008.
- [16] H. Xing, A. Makinouchi, C. Zhao, Three-dimensional finite element simulation of large-scale nonlinear contact friction problems in deformable rocks, *Journal of Geophysics and Engineering* 5 (2008) 27–36.
- [17] D. Sohn, J.H. Lim, Y.S. Cho, J.H. Kim, S. Im, Finite element analysis of quasistatic crack propagation in brittle media with voids or inclusions, *Journal of Computational Physics* 230 (2011) 6866–6899.
- [18] E.J. Garboczi, A.R. Day, An algorithm for computing the effective linear elastic properties of heterogeneous materials: three-dimensional results for composites with equal phase Poisson ratios, *Journal of the Mechanics and Physics of Solids* 43 (1995) 1349–1362.
- [19] K. Terada, T. Miura, N. Kikuchi, Digital image-based modeling applied to the homogenization analysis of composite materials, *Computational Mechanics* 20 (1997) 331–346.
- [20] R.E. Guldberg, S.J. Hollister, G.T. Charras, The accuracy of digital image-based finite element models, *Journal of Biomechanical Engineering* 120 (1998) 289–295.
- [21] Z. Wu, J.M. Sullivan Jr, Multiple material marching cubes algorithm, *International Journal for Numerical Methods in Engineering* 58 (2003) 189–207.
- [22] Y. Zhang, C. Bajaj, G. Xu, Surface smoothing and quality improvement of quadrilateral/hexahedral meshes with geometric flow, in: *Proceedings of the 14th International Meshing Roundtable*, Springer, 2005, pp. 449–468.
- [23] T. Blacker, M. Stephenson, Paving – a new approach to automated quadrilateral mesh generation, *International Journal for Numerical Methods in Engineering* 32 (1991) 811–847.
- [24] K.Y. Lee, Kim, II, D.Y. Cho, T. Kim, An algorithm for automatic 2D quadrilateral mesh generation with line constraints, *Computer-Aided Design*, 35 (2003) 1055–1068.
- [25] S.J. Owen, M.L. Staten, S.A. Canann, S. Saigal, Q-Morph: an indirect approach to advancing front quad meshing, *International Journal for Numerical Methods in Engineering* 44 (1999) 1317–1340.
- [26] C. Park, J.S. Noh, I.S. Jang, J.M. Kang, A new automated scheme of quadrilateral mesh generation for randomly distributed line constraints, *Computer-Aided Design* 39 (2007) 258–267.
- [27] Y. Liu, H.L. Xing, Z. Guan, An indirect approach for automatic generation of quadrilateral meshes with arbitrary line constraints, *International Journal for Numerical Methods in Engineering* 87 (2011) 906–922.
- [28] E. Catmull, J. Clark, Recursively generated B-spline surfaces on arbitrary topological meshes, *Computer-Aided Design* 10 (1978) 350–355.
- [29] R. Kimmel, J.A. Sethian, Computing geodesic paths on manifolds, in: *The National Academy of Sciences of the USA*, 1998, pp. 8431–8435.
- [30] J.S.B. Mitchell, D.M. Mount, C.H. Papadimitriou, The discrete geodesic problem, *SIAM Journal on Computing* 16 (1987) 647–668.

- [31] V. Surazhsky, T. Surazhsky, D. Kirsanov, S.J. Gortler, H. Hoppe, Fast exact and approximate geodesics on meshes, *ACM Transactions on Graphics (TOG)* 24 (2005) 553–560.
- [32] M.S. Floater, K. Hormann, Surface parameterization: a tutorial and survey, in: N.A. Dodgson, M.S. Floater, M.A. Sabin (Eds.) *Advances in multiresolution for geometric modelling*, Springer Berlin Heidelberg, 2005, pp. 157–186.

2.3 Conclusions

An automatic quadrilateral mesh generation algorithm is proposed here for heterogeneous rock. The algorithm overcomes difficulties in meshing rock images by (1) a phase-based smoothing strategy which is designed to remove staggered features on material boundaries and (2) geodesic-isoline-aided meshing scheme which is utilized to indirectly guarantee well-aligned elements parallel to the boundaries. Examples from practice demonstrate the effectiveness of the proposed method. Concerning the element quality, the proposed Pisces valence clear-up pattern is effective in reducing the number of irregular inner nodes and improving the element quality across the mesh including close to the boundaries. Moreover, compared with the methods of Lee et al. [43] and Park et al. [168], the proposed meshing method can generate elements with a higher quality. The numerical examples also yield high quality meshes around material boundaries superior to those generated by the methods of Liu et al. [152] and Catmull-Clark [37].

Chapter 3 Three-Dimensional Mesh Generation for Fractured Rock

3.1 Overview

With the development of advanced imaging techniques, structures of fractured rock mass can be clearly captured by high-resolution digital images in 3D [3, 4]. However, such images have a huge data set, which is difficult and even impossible to be applied in both visualization [103] and simulation [1, 104]. A substitute for digital images is meshes whose data set is small but the generation process is challenging.

This chapter focuses on developing an effective mesh generation algorithm for 3D rock masses with arbitrary fractures. Fractures in rocks are naturally complicated. As they may meet at arbitrary angles at junctions, and the topological defects, geometric errors and/or local connectivity flaws could be derived on mesh models. Regarding mesh generation for fractures, there are two major problems: (1) how to identify junctions of different fractures and (2) how to construct elements on fractures.

In terms of junction identification, we assign each fracture voxel a junction weight by a disk scanning method and then recognize fracture junctions by an adequate threshold. In terms of element construction, we propose a pseudo-surface assumption together with a simplified centroidal Voronoi diagram to initially generate surface meshes representing fractures and design an innovative umbrella operation to further repair mesh topology structures. The fractured rock mass is represented by a tetrahedral mesh model with the above fracture surface mesh constraints. Compared with the digital image models, the generated mesh models can significantly reduce the data size and well preserve the fracture features.

Three practical fractured rocks are taken as application examples to be analysed in this chapter to demonstrate the usefulness and capability of the proposed meshing approach. Numerical experiments show that the proposed meshing algorithm is effective to handle complicated fracture

structures. Moreover, the generated mesh representing a fractured rock has a high shape similarity 64.57% and its data size is merely 1/6000 as much as that of the image data.

3.2 Digital rock imaging

Rocks are naturally inhomogeneous materials which consist of various constituents such as minerals, grains, voids, fractures, et al. The digital imaging process for rocks is difficult. This is because during the production of the images, ambiguities may happen if there is no prior knowledge about the constructive minerals [100]. Besides, partial volume effect is another reason of generating poor quality digital images. Once the rock images are obtained, segmentation is performed for identification and labelling mineral phases and rock structures, which includes spatial filtering, noise removal, morphological operations and cluster analysis. With regard to fractured rocks, the fracture thickness is usually much smaller than the sample mass scale. Thus high resolution images together with adequate segmentations are required to achieve an accurate quantitative description of the fractures [103]. For a comprehensive review of imaging techniques and related segmentations, readers are referred to [3, 101, 102].

3.3 3D Fracture junction identification

3D fractured rock images obtained from scanning electron microscopy are utilized as input of our image meshing approach. One key character of fractures is that the thickness is much smaller than the length and width. Based on this character, we can assume that fractures are somehow surfaces, but such a pseudo-surface assumption is not always satisfied as far as fracture junctions are concerned. Therefore, one key process of our meshing approach is to identify junctions and adapt them to the pseudo-surface assumption in the related mesh generation as detailed below.

3.3.1 Fracture medial surface extraction

Voxel is the basic unit of 3D digital images, which has a position and a scalar value describing its material property. In practice, as fractures in the form of voxels have different thicknesses, a thinning method [169] is employed to represent fractures by their medial surfaces which share a same thickness. To carry out a robust implementation, a 26-connection is used here and we release the surface point identification conditions in [169] by Formula 3.1.

Definition 1. A voxel v is a surface voxel if $\forall i, i \in \{1, \dots, 8\}$,

$$|N_i^2(v)| \leq 6 \quad (3.1)$$

Where $N(v)$ denotes neighbours of v , $N_i^2(v)$ is the i th octant of $N(v)$ and $|\cdot|$ is the number of voxels in the octant.

Figure 3.1 (a) is a part of fractures obtained from a rock mass, where fractures have different thicknesses and intersect with each other. The fracture medial surfaces Figure 3.1 (b) are extracted under the condition in Formula 3.1 and their thicknesses are almost even everywhere. The thinning process is necessary, as it could reduce numeric errors caused by the thickness difference concerning the junction identification and mesh generation.

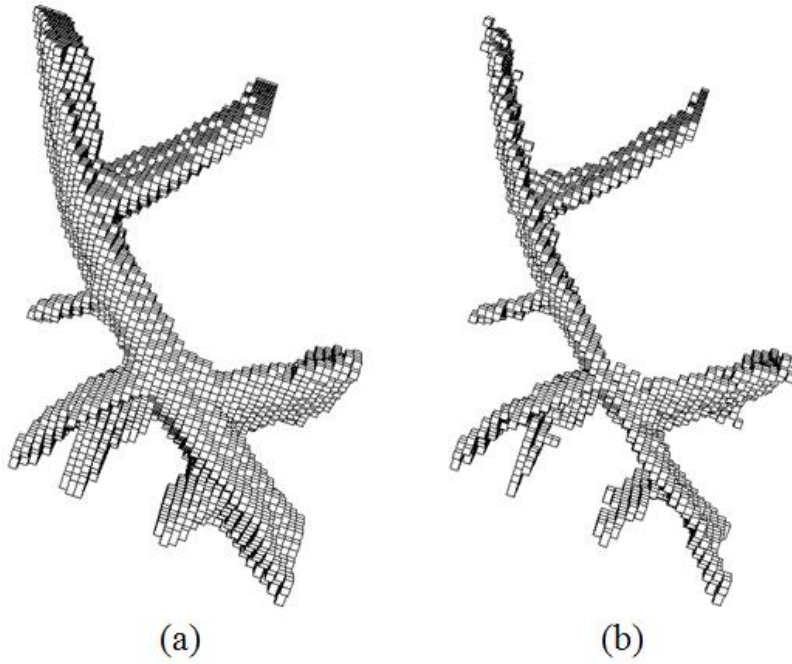


Figure 3.1: Medial surface extraction: (a) fractures extracted from a rock and (b) the medial surface

3.3.2 Disk scanning method for fracture junction identification

In this paper, a Junction Weight (JW) is designed to identify whether a fracture voxel locates at the junctions or not. For a voxel v , the calculation of its JW is achieved by Formula 3.2.

$$JW = (1.0 - W_2)W_1 \quad (3.2)$$

Here, W_1 is the number of fracture voxels within a cubic of $5 \times 5 \times 5$ voxels surrounding v . W_2 is calculated by a disk scanning process which will be described in details as below.

For each voxel on fractures, a scanning disk is created by the Breadth First Search (BFS) with a volume criterion in Formula 3.3.

$$\text{Disk Volume} < t(1+2r(r-1)) \quad (3.3)$$

Where t is the fracture thickness and r is the disk radius. On the disk, m triangles $\{T\}_m$ are randomly generated by two rules: (1) each vertex is on the disk border and (2) the length of each edge is larger than $\sqrt{3}r$. We associate $W_2 = \{\min(\vec{n}_i \cdot \vec{n}_j) \mid i, j \in \{T\}_m, i \neq j\}$ with all the voxels on the disk. A voxel on fractures will be associated with W_2 for a couple of times, and thus the average value is adopted. The property of W_2 is the flatter the disk, the higher the W_2 . For instance, a flat disk in Figure 3.2 (a) on fracture surfaces has a higher W_2 compared to a staggered or bended disk in Figure 3.2 (b) at fracture junctions.

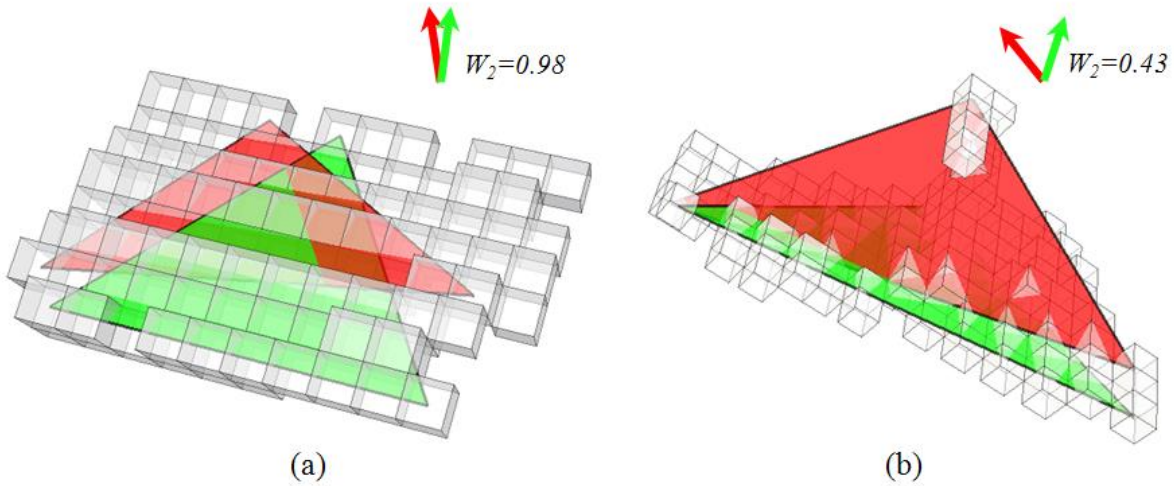


Figure 3.2: Scanning disks with different W_2 values: W_2 of a flat disk (a) is higher than that of a non-flat disk (b).

JWs of fractures for Figure 3.1 (b) are obtained through Formula 3.2 and demonstrated in Figure 3.3 from two different view angles. Obviously, JW values decrease from junctions to surfaces, or in other words, voxels having higher JW are closer to junctions.

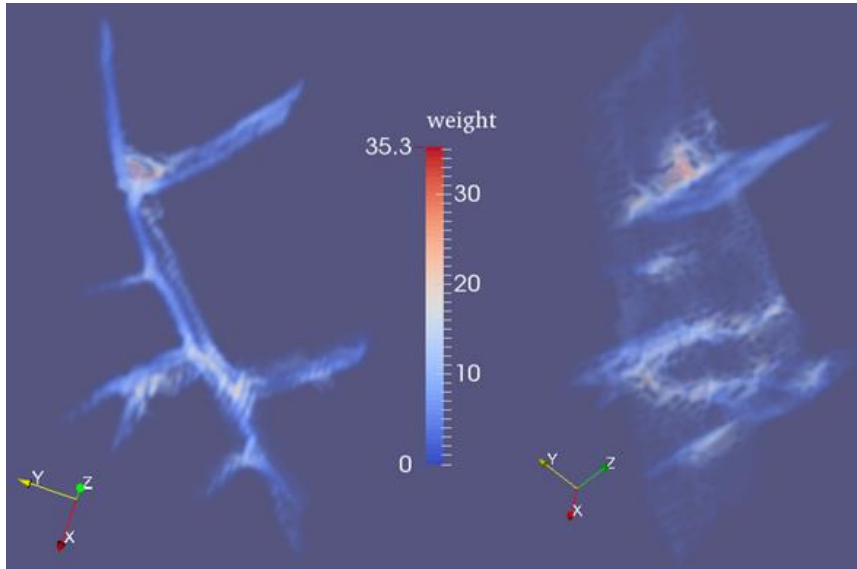


Figure 3.3: Junction identification: left and right are the same fractures with different view angles and colours indicate different JWs on the fractures.

3.4 Simplified centroidal Voronoi diagram and mesh generation

Based on the pseudo-surface assumption for fractures, Voronoi diagram is expected to be constructed on fractures to achieve the corresponding mesh generation. However, one difficulty of the Voronoi diagram construction on a voxel-based surface is the distance calculation. Here, an alternative approach is designed for generating the Voronoi diagram, which avoids calculating distance between two points.

3.4.1 Simplified Centroidal Voronoi Diagram (SCVD) construction for fractures

Given an open set $\Omega \subseteq R^N$, and n different generators $\{z_i\}_{i=1}^n$. Let $dis(\cdot)$ denote the distance function on R^N , the Voronoi diagram (whose dual is well-known as Delaunay triangulation) is defined as $\{V_i\}_{i=1}^n$:

$$V_i = \{x \in \Omega \mid dis(x, z_i) < dis(x, z_j) \text{ for } j = 1, \dots, n, j \neq i\} \quad (3.4)$$

Centroidal Voronoi diagram is firstly proposed by Du et al. [29] where the generator z_i is also the mass centroid of its Voronoi cell:

$$z_i = \frac{\int_{V_i} x \cdot \rho(x) dx}{\int_{V_i} \rho(x) dx} \quad (3.5)$$

Where $\rho(x)$ is a density function of V_i .

We propose a simplified centroidal Voronoi diagram to construct Voronoi diagram on fractures. In 3D rock images, fractures are represented by a set of voxels sharing the same volume and density, so in the proposed SCVD construction $\rho(x)=1$ for Formula 3.5. According to the pseudo-surface assumption, the Voronoi diagram is generated by propagating Voronoi cells from their generators in the manner of BFS. Formula 3.4 is automatically satisfied in the process of BFS and the distance calculation $dis(\cdot)$ is thereby avoided. Pseudo-code in Algorithm 3.1 describes the simplified Voronoi diagram construction where 6-voxel connectivity is employed. Take a patch in Figure 3.4 for example, Figure 3.4 (a)-(c) are three stages from the generators to the final Voronoi cells.

Algorithm 3.1: *Simplified Voronoi diagram construction*

Treat voxels linked with z_i as the initial Voronoi cell V_i

WHILE *there is a voxel not belonging to $\{V_i\}_{i=1}^n$*

FOR EACH V_i *in $\{V_i\}_{i=1}^n$*

Progress V_i by one voxel in the manner of BFS

END

END

SCVD is an approximate implementation of centroidal Voronoi diagram, which bases on the theory proposed by Du et al. [29]. Firstly, n Voronoi generators $\{z_i\}_{i=1}^n$ are randomly selected from the voxels on fractures. Then locations of these generators are iteratively optimized by Formula 3.5 until the energy error [29] is achieved. The generator number n is calculated by the following formula.

$$n = \frac{C_{vol}}{V_{vol}}, V_{vol} = t(1 + 2r(r - 1)) \quad (3.6)$$

Where C_{vol} is the total volume of the structure, t is the average thickness and r is the customized radius of a Voronoi cell. As C_{vol} and t are known, r is the only variable to define the generators as well as the SCVD.

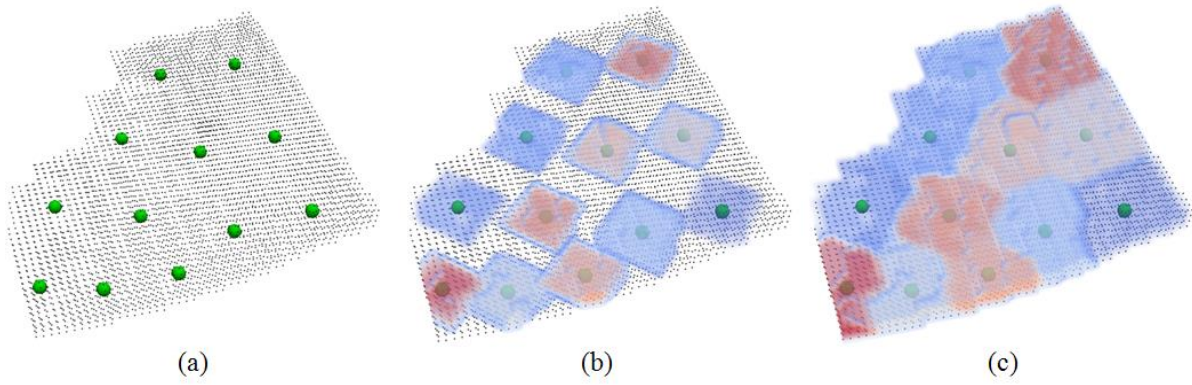


Figure 3.4: Simplified Voronoi diagram construction: (a) a patch and its generators; (b) the growing Voronoi cells; (c) the final Voronoi diagram.

Directly involving SCVD to construct a triangular mesh for fractures may lead to a number of topology defects and geometric errors at fracture junctions. Alternatively, we enhance the SCVD construction process through three steps: (1) identifying junctions through a JW threshold, (2) separately constructing SCVD at fracture junctions and surfaces and (3) merging them together. The enhanced process is demonstrated in Figure 3.5, and (a)-(c) are the SCVD at fracture junctions, the SCVD at fracture surfaces and the result combining (a) with (b). As fracture surfaces without junctions could satisfy the pseudo-surface assumption, the enhanced SCVD construction will reduce the chance of deriving connectivity flaws at the corresponding initial triangular mesh.

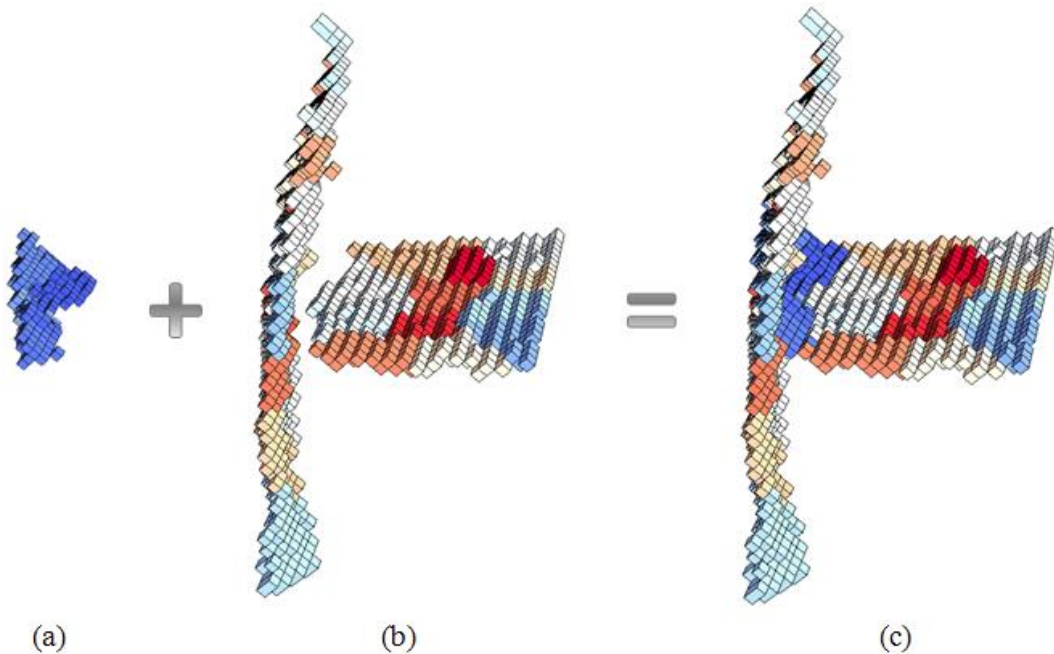


Figure 3.5: The enhanced construction of SCVD for fractures: (a) the SCVD at fracture junctions, (b) the SCVD at fracture surfaces and (c) the SCVD for the fractures.

3.4.2 Mesh generation for fractures

The surface mesh generation for fractures is based on the SCVD. The generating route is similar to the Delaunay triangulation but ambiguities caused by the fuzzy cell boundaries need to be further refined. In Figure 3.6, A , B , C and D represent IDs of Voronoi cells and the dots represent voxels within a cubic. For a regular case, in Figure 3.6 (a), there are only three IDs in the cubic and a triangle is constructed by connecting the corresponding generators. For an ambiguous case, in Figure 3.6 (b), more than three IDs exist in the cubic and the constructed triangles will cause a topological defect.

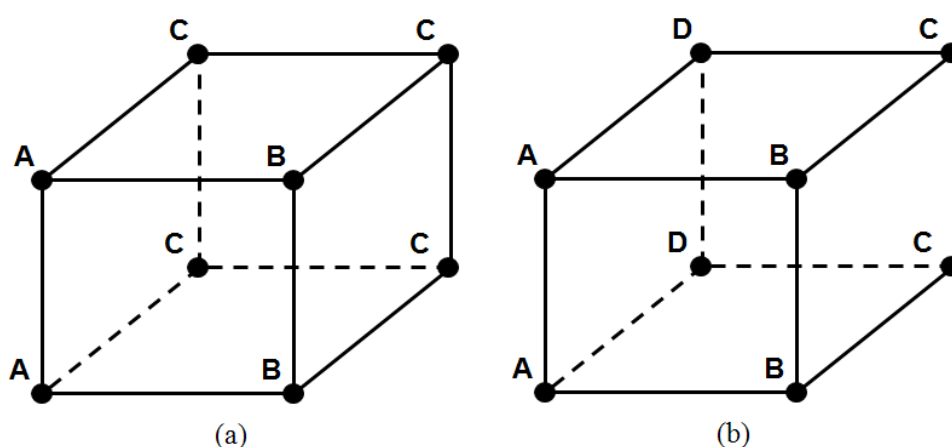


Figure 3.6: Triangular element construction: (a) a regular case and (b) an ambiguous case

As fractures are represented by surface meshes rather than volume meshes, dual contouring-based meshing methods [170, 171] are not suitable to resolve the topology ambiguity here. Therefore, an amending strategy is proposed to remove such ambiguity in triangular element construction. As shown in Figure 3.7 (a), the SCVD has four generators A , B , C and D and the ambiguity is highlighted in a black circle. The amending strategy is processed during the SCVD construction. Specifically, two generators are connected whenever their corresponding Voronoi cells meet each other in the propagation. In Figure 3.7 (b)-(e), $B-D$, $C-D$, $A-C$ and $A-B$ are connected serially and a polygon $ABCD$ is constructed simultaneously. Based on the polygon, triangles ACD and ABD in Figure 3.7 (f) are created.

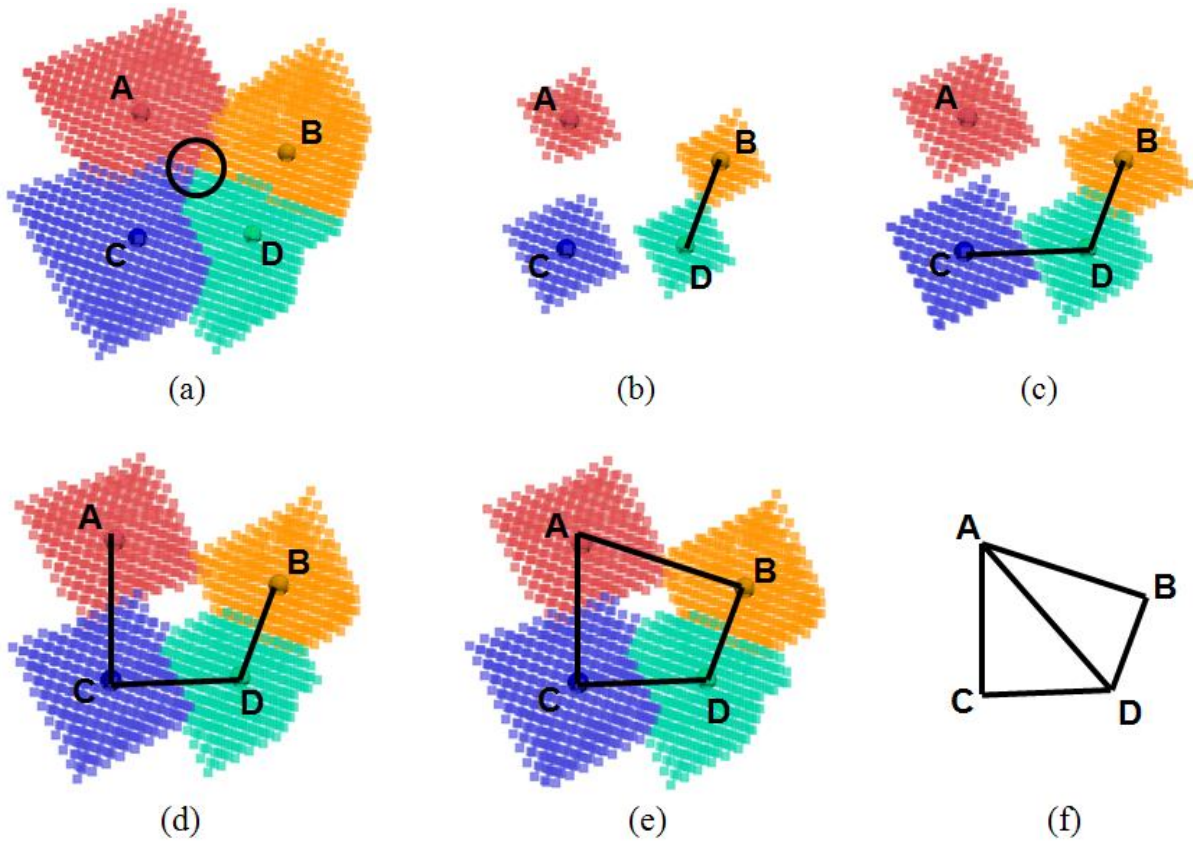


Figure 3.7: Amending strategy for triangular element construction: (a) the SCVD with ambiguity; (b)-(f) the proposed amending processes based on the proposed strategy

3.5 Mesh repairing

Due to the inherent discreteness of the voxel models, topological and geometric errors are not avoidable in the generated mesh model. Especially at fracture junctions, ambiguously connected triangles lead an incorrect mesh representation of fractures. Hence, an effective mesh repairing algorithm is desired.

Before a detailed description of the mesh repairing method, the following definitions and notions have to be clarified:

Manifold edge: an edge shared by at most two triangles.

Non-manifold edge: an edge shared by more than two triangles.

Junction edge: an edge with two junction nodes.

Junction triangle: a triangle with three junction nodes.

2D disk of a node: the incident triangles parameterized to a 2D domain.

Conventional criteria [172] of a valid mesh are not suitable for a mesh representing fractures. As holes, non-manifold edges, inconsistent orientation (caused by the Mobius strip) are reasonable structures for fractures. Focusing on adequately representing fractures by mesh models, we propose three criteria for a valid surface mesh of fracture.

Valid Mesh Criterion (VMC):

- (a) Any edge with a fracture surface node must be manifold;
- (b) Any junction edge must distinctly describe the corresponding fracture junction;
- (c) There are no self-intersections.

3.5.1 Umbrella operation

An umbrella operation is proposed here to reconstruct topology structure around a fracture surface node. The input for an umbrella operation is a surface node N and edge constraints $\{EC\}$. The initial $\{EC\}$ are junction edges.

Algorithm 3.2: Umbrella Operation

Step 1: Collect incident triangles $\{T\}$ for a surface node N and collect related edge constraints $\{ec\}$ from $\{EC\}$

Step 2: Parameterize $\{T\}$ to $\{t\}$ in a 2D domain

Step 3: Break edges $\{e\}$ in $\{t\}$ by their intersections $\{i\}$, then update $\{e\}$

Step 4: Taking $\{e\}$ as line constraints, generate a mesh M from $\{i\}$ and nodes in $\{t\}$ by a 2D constrained Delaunay triangulation

*Step 5: Suppress $\{i\}$ in M and recovery $\{ec\}$; If $\{ec\}$ are not fully recovered, then return **FALSE***

Step 6 : Reconstruct $\{T\}$ by the topology of M ; push edges on the 2D disk of N into $\{EC\}$

*Step 7 : Return **TRUE***

We demonstrate the process of an umbrella operation in Figure 3.8. Firstly, the incident triangles in Figure 3.8 (a) of a surface node N are parameterized to a 2D domain in Figure 3.8(b). As some triangles overlap with each other, one of the edge constraints in red is broken on the 2D disk. Secondly, to reconstruct the disk mesh, we invoke a 2D constrained Delaunay triangulation together with the intersection node suppression and the edge constraint recovery. Finally, the reconstructed mesh Figure 3.8 (c) is projected back to the original surface as shown in Figure 3.8 (d). It is

worthwhile to note that only edges (the blue ones in Figure 3.8 (d)) on the 2D disk of node N is utilized to update the edge constraints $\{EC\}$.

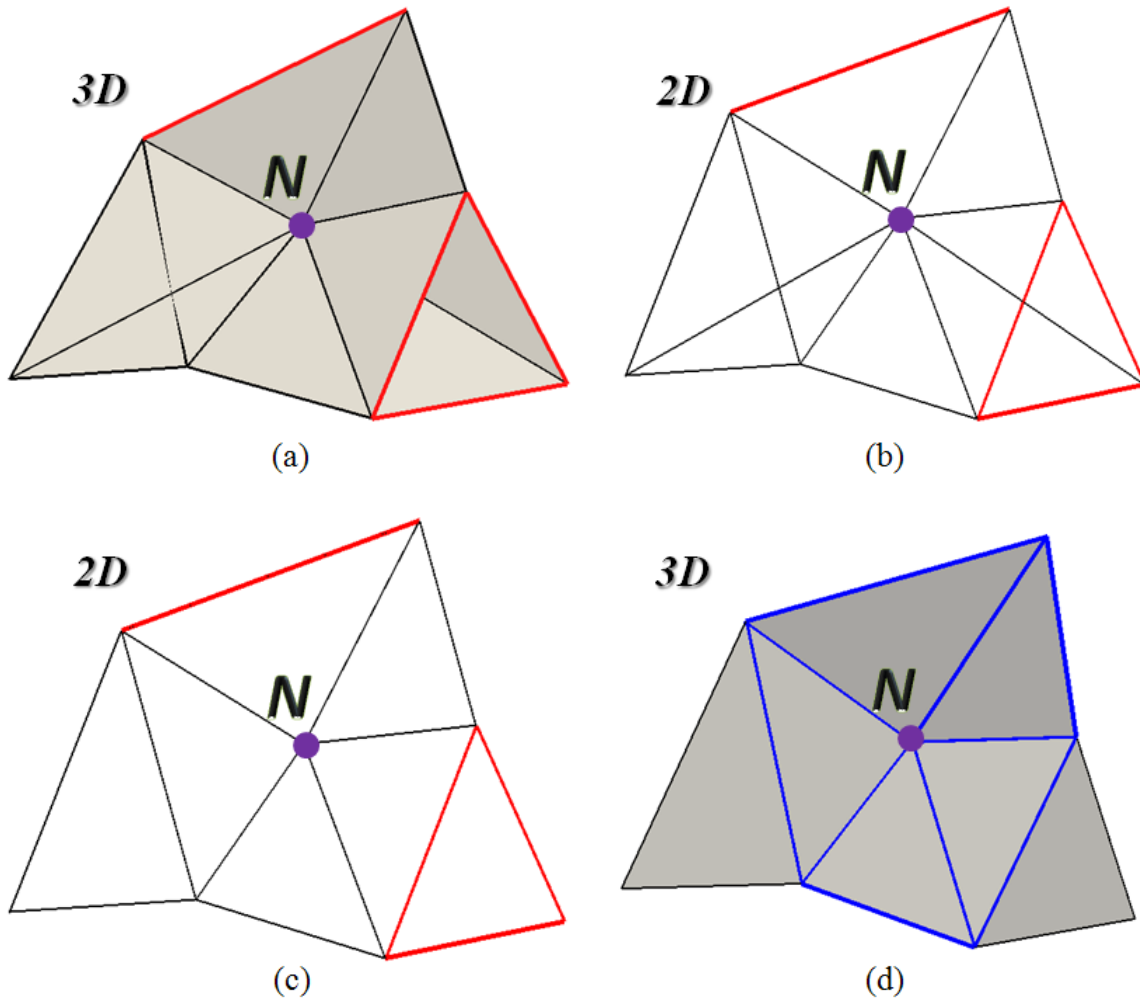


Figure 3.8: An umbrella operation on a surface node N : (a) incident triangles and edge constraints in red, (b) the parameterized mesh in 2D domain, (c) the 2D mesh with recovered edge constraints and (d) reconstructed triangles and new generated edge constraints in blue.

3.5.2 Effectiveness evaluation

In this section, the effectiveness of the umbrella operation is further evaluated by both its advantages and limitations.

If all the umbrella operations for the surface nodes are successful, the following propositions are drawn.

Proposition 3.1: An edge with two surface nodes is manifold.

Proof: As the umbrella operations on both of the edge nodes are successful, the maximum number of triangles connected with the edge is two. In other words, the edge is manifold.

Q.E.D.

Proposition 3.2: If a junction node has no more than two junction neighbours, then there are no overlaps on the 2D disks of its surface neighbours.

Proof: There are three cases. (1) A junction node has no junction neighbours. The umbrella operation guarantees the correctness of the proposition. (2) A junction node has only one junction neighbour. If there are overlaps, only the junction edge has a chance of intersecting with an edge on one of the 2D disks. However, as a constraint in the umbrella operation, no edges will intersect with the junction edge. (3) A junction node has two junction neighbours. There are at most three junction edges which consist of the junction node and its two junction neighbours. As the three nodes have different locations, the junction edges cannot intersect with each other on any of the 2D disks. Thus Proposition 3.2 is correct.

Q.E.D.

Evidently, the VMC (a) and (b) are guaranteed by Propositions 3.1 and 3.2. Concerning VMC (c), we assume an edge ab intersect with a triangle ABC in the initial fracture mesh. Since the mesh is generated from a volumetric image, the five nodes a, b, A, B and C must connect with each other by triangles. The VMC (c) is satisfied if there are not junction triangles overlapping with each other. In summary, to satisfy VMC (a), (b) and (c), two conditions must be achieved: (1) all the surface node umbrella operations are successful and (2) there are no overlapped junction triangles.

In practice, the failure of umbrella operation is mainly caused by the intersection of junction edges. As shown in Figure 3.9 (a), junction edges in red are intersected on the 2D disk of node N . The corresponding umbrella operation fails as it is impossible to recover all junction edges. Besides, three overlapped junction triangles ABC , ACD and BCD are also demonstrated in Figure 3.9 (b). Due to these structures, manual procedure is still required to fix the repaired surface mesh of fracture.

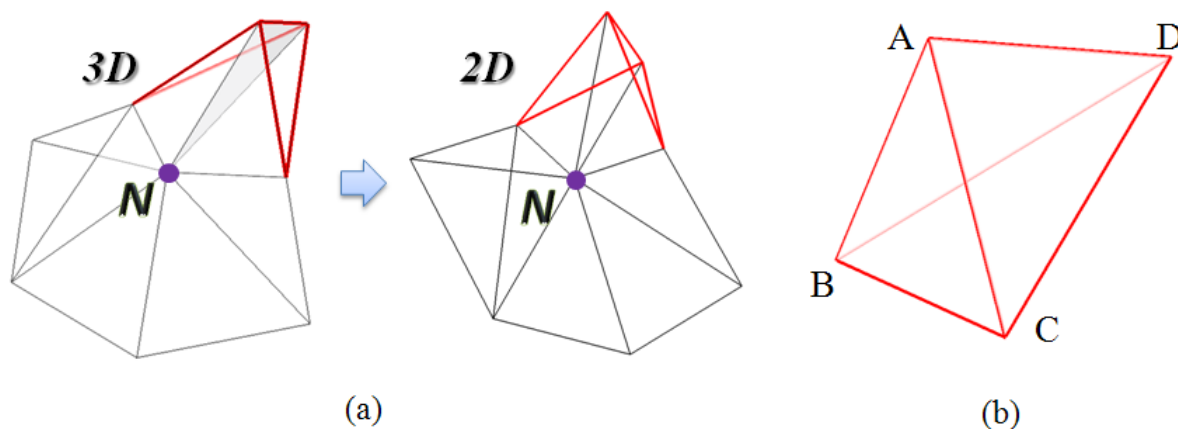


Figure 3.9: Cases failed to satisfy the VMC: (a) a failed umbrella operation; (b) overlapped junction triangles.

3.6 Mesh optimization

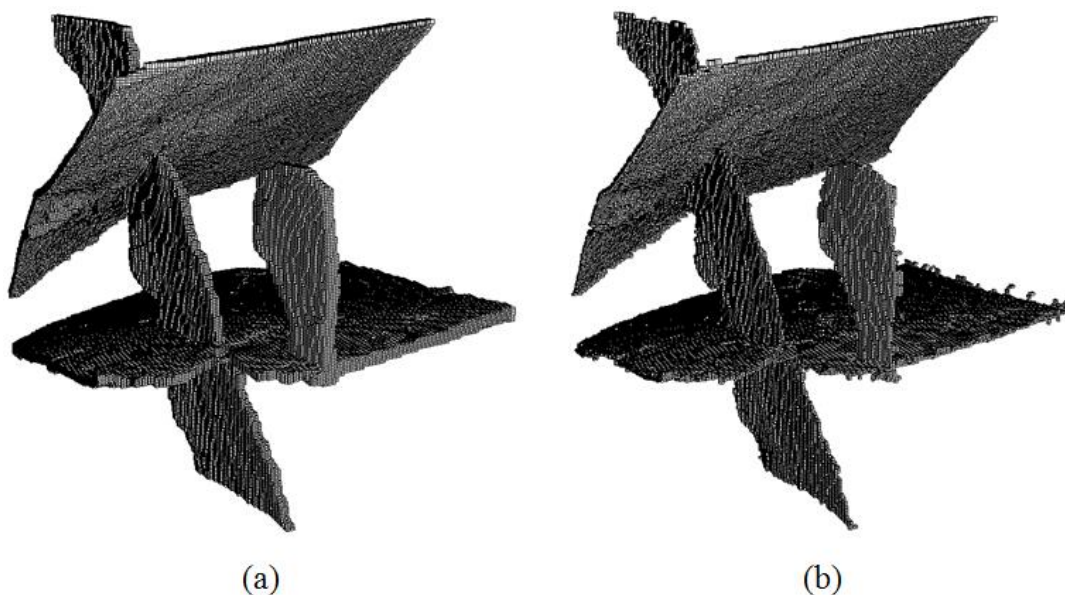
To further improve the element quality, we proposed a local optimization method for the repaired mesh. The junctions and surface boundaries are firstly smoothed. For each junction, the smoothing procedure is achieved by the following steps: (1) detaching incident element patches from the junction edges, (2) parameterizing these patches to a 2D domain and smoothing the junction respectively and (3) projecting the patches back to 3D and assembling them together. The surface boundary smoothing is similar with the junction smoothing. Concerning the optimization of surface elements, it is implemented by extracting N-ring elements of a surface node and optimizing these elements through the isotropic remeshing algorithm in [28].

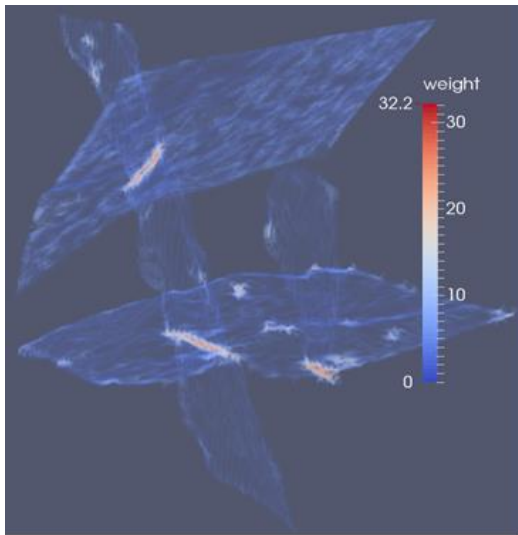
3.7 Numerical applications

We use three application examples to demonstrate the effectiveness of the proposed meshing approach. The first one is a rock with four fractures, which is utilized to illustrate the workflow of meshing fractures intersecting with each other. The second one is utilized to choose an optimal Voronoi cell radius r based on a shape similarity measurement. The last example is a rock mass with complicated structures (216 fractures). Based on this rock mass, issues such as the choice of JW threshold, the effectiveness of the umbrella operation as well as the element quality of the mesh representation are discussed.

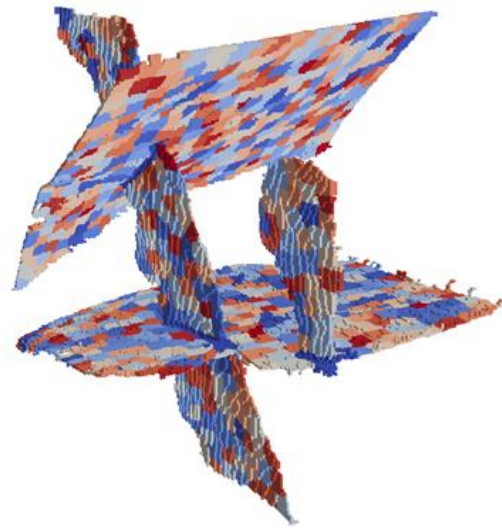
3.7.1 The workflow of the proposed algorithm

The first example, Figure 3.10 (a), is fractures within a box of $160 \times 175 \times 200$. The fractures have four patches intersecting with each other. We demonstrate the workflow of the meshing strategy as below. At the first stage, our mesh approach extracts medial surfaces (in Figure 3.10 (b)) of the fractures and calculates JW values for the surfaces. In Figure 3.10 (c), high JWs are represented by red and low JWs are represented by blue. Fracture junctions are roughly depicted by red lines, while there are also several red spots which are caused by local uneven structures. We use $JW=11$ to distinguish fracture junctions from surfaces and Voronoi cell radius $r=7$ to create a SCVD (in Figure 3.10 (d)) on the fractures. At the next stage, an initial surface mesh is generated from the SCVD. The mesh is demonstrated in Figure 3.10 (e), where junction nodes are in red and surface nodes are in blue. The proposed umbrella operations are applied to the surface nodes to repair the mesh topology. In this sample, all the umbrella operations are successfully processed. Thus the mesh model in Figure 3.10 (f) is a valid mesh which satisfies VMC (a), (b) and (c). To further improve the element quality, we optimize the surface mesh and smooth the fracture junctions highlighted by red lines in Figure 3.10 (g). The close-ups in Figure 3.10 (e)-(g) demonstrate the structure changing of a part of fracture junctions in the processes of mesh generation, repairing and optimization. At the last stage, taking the surface mesh Figure 3.10 (g) as constraints, a volume mesh is generated and shown in Figure 3.10 (h), where the surface mesh of fracture is consistent with the volume mesh.

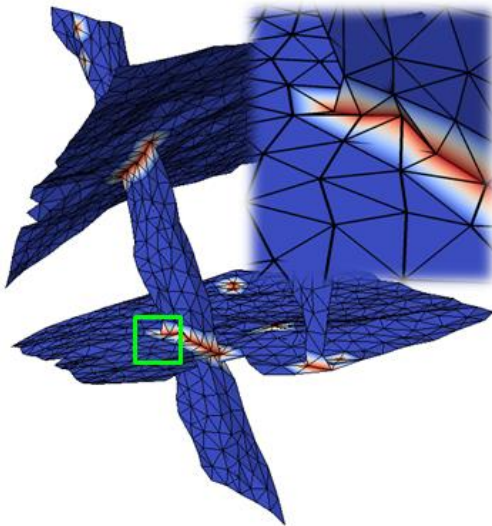




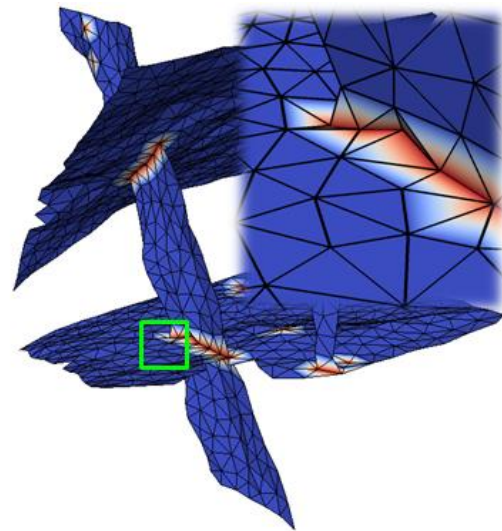
(c)



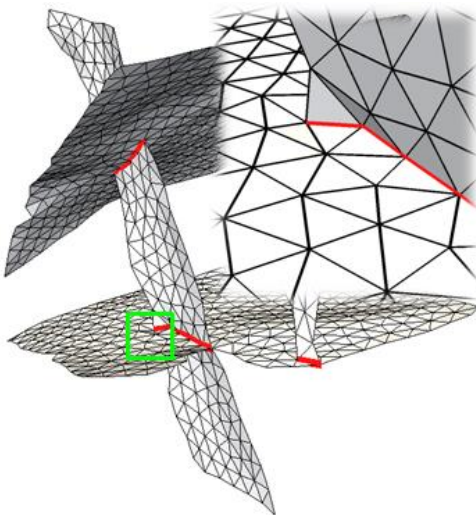
(d)



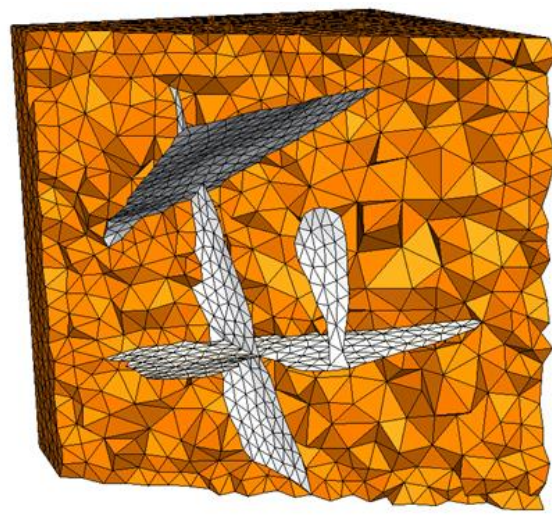
(e)



(f)



(g)



(h)

Figure 3.10: Fractures of a rock mass: (a) the fractures in voxel format, (b) medial surfaces of the fractures, (c) the JW diagram, (d) the SCVD, (e) the initially generated mesh, (f) the repaired mesh, (g) the optimized mesh and (h) the volume mesh for the fractures.

3.7.2 The choice of an optimal Voronoi cell radius

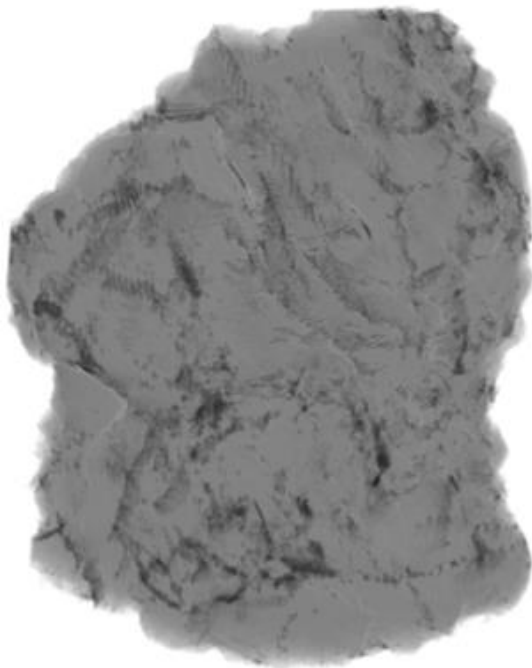
The purpose of this example is to find an optimal Voronoi cell radius concerning a shape similarity. Hence, the similarity measurement is firstly introduced, which evaluates how the generated mesh model is close to the input 3D image. For a surface mesh, each element has a thickness value, which is gained from the input image. Specifically, each fracture voxel has a thickness value, obtained by the smallest thickness in its three directions. The thickness of a triangular element is the average thickness of voxels intersecting with it. Letting the triangle be the mid plane and its thickness be the height, a prism is constructed for the element. We convert each element of the surface mesh to a volumetric representation by labelling voxels within its prism. Then a volumetric description of the surface mesh is generated. Compared with the input image, voxels of the mesh volumetric representation could be grouped into two sets: C_{mesh}^{in} coincident with the input image and C_{mesh}^{out} different from the input image. Taking into account both C_{mesh}^{in} and C_{mesh}^{out} , a similarity measurement is defined as:

$$Similarity = \frac{|C_{mesh}^{in}| - |C_{mesh}^{out}|}{|C_{image}|} \quad (3.7)$$

Where C_{image} is the set of fracture voxels in the input image and operator $|\cdot|$ calculates the number of voxels. The range of the similarity is $[1.0, -\infty]$ and a larger value denotes better matching with the original data.

The first example in Figure 3.11 (a) is a rock image and its size is 1012×1024×931. The rock has complex internal structures that are individually shown in Figure 3.11 (b). The major fractures extracted in Figure 3.11 (c) are utilized to represent the model as they primarily affect the mechanical behaviour of the rock and are focus of the further numerical analysis. Additionally, models built based on the major fractures improve our understanding of the rock structure and reduce the scale of dataset. Figure 3.11 (d)-(f) show the ability of the proposed method to control element size and quantity in meshing rock images (where fractures are in white and rock boundaries are in golden). Table 3.1 gives an overview of element size, number and similarity between the meshes and its 3D image model in Figure 3.11 (c). Consequently, the features of the generated

mesh is controlled by Voronoi cell radius r in Formula 3.6, where with the increasing of r the element number is reduced but the similarity is decreased as well.



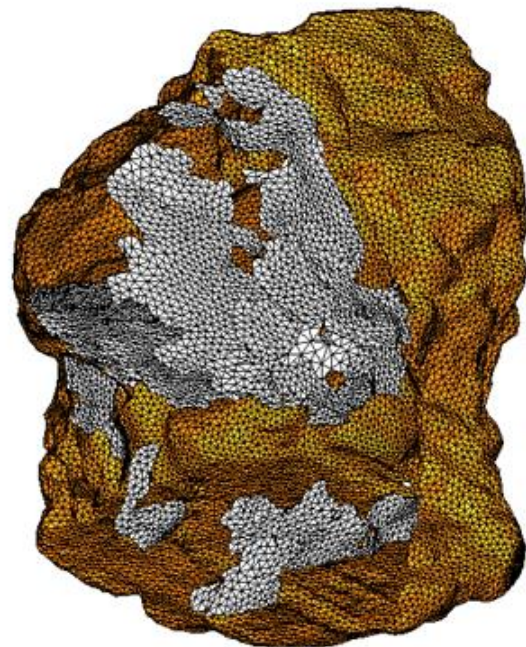
(a)



(b)



(c)



(d)

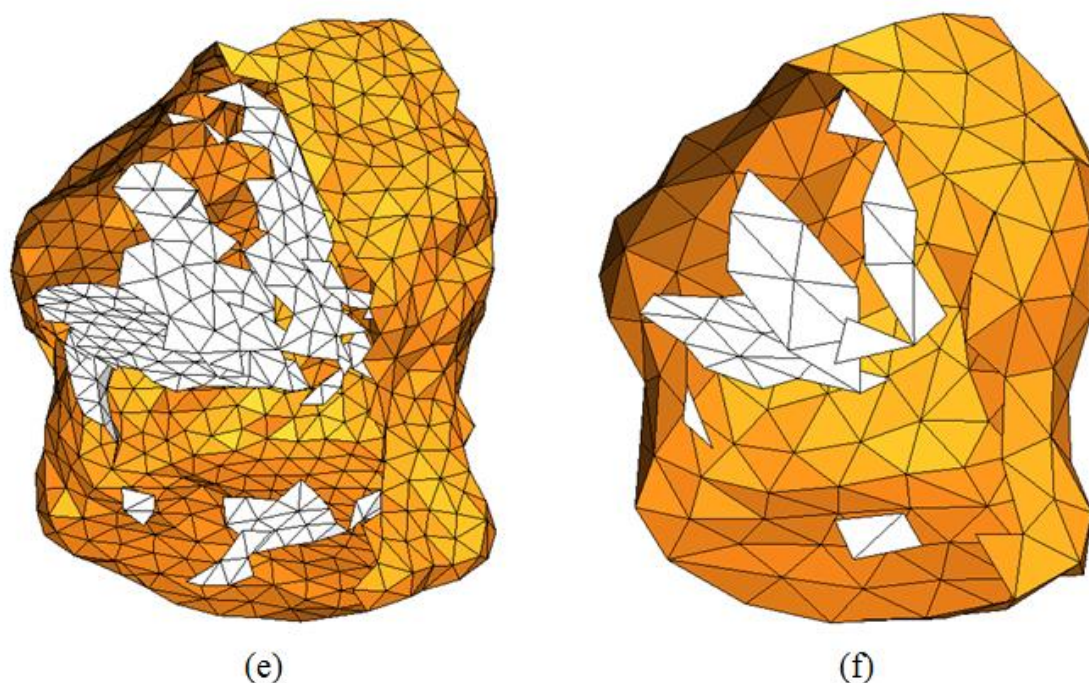


Figure 3.11: A 3D rock image meshed with different element sizes: (a) the 3D rock image with a size of $1012 \times 1024 \times 931$; (b) the internal structures; (c) the major fractures; (d)-(f) are triangular meshes generated by different Voronoi cell radii where the major fractures are shown in white colour and the outside rock boundaries in golden.

Table 3.1: Summary for surface meshes in Figure 3.11 (d)-(f)

Figure 3.11	(d)	(e)	(f)
Voronoi Cell Radius	11	51	107
Element Size	14.88	66.49	135.75
Element Number	40,204	1,777	368
Similarity	63.28%	29.46%	11.66%

A chart in Figure 3.12 is obtained through meshing the fractures in Figure 3.11 (c), which further reveal the relationship between Voronoi cell radius r and the corresponding mesh similarity. On one hand, once r is close or less than the thickness the pseudo-surface assumption is not true and thus fractures cannot be correctly represented. On the other hand, if r is large then some details of fractures are lost. According to Figure 3.12, Voronoi cell radius $r=7$ is the best choice with respect to the highest shape similarity 64.57%, which generates a surface mesh with 69,394 elements. Considering the image models in the form of grids, evenly sampling the grids to reduce image resolution could simplify the model and reduce its dataset scale, but the similarity will drop dramatically as shown in Table 3.2. Additionally, the resolution reduction approach is not as effective as the proposed image meshing algorithm in representing fractures for visualization.

Compared with the mesh model with $r=7$, grid models whose sampling rates are larger than 2 have a lower similarity and a larger grid number. Although the similarity of grid model with sampling rate 2 is comparable with the mesh mode similarity, its grid quantity is 9.6×10^8 which is 1.4×10^4 times as much as that in the mesh model.

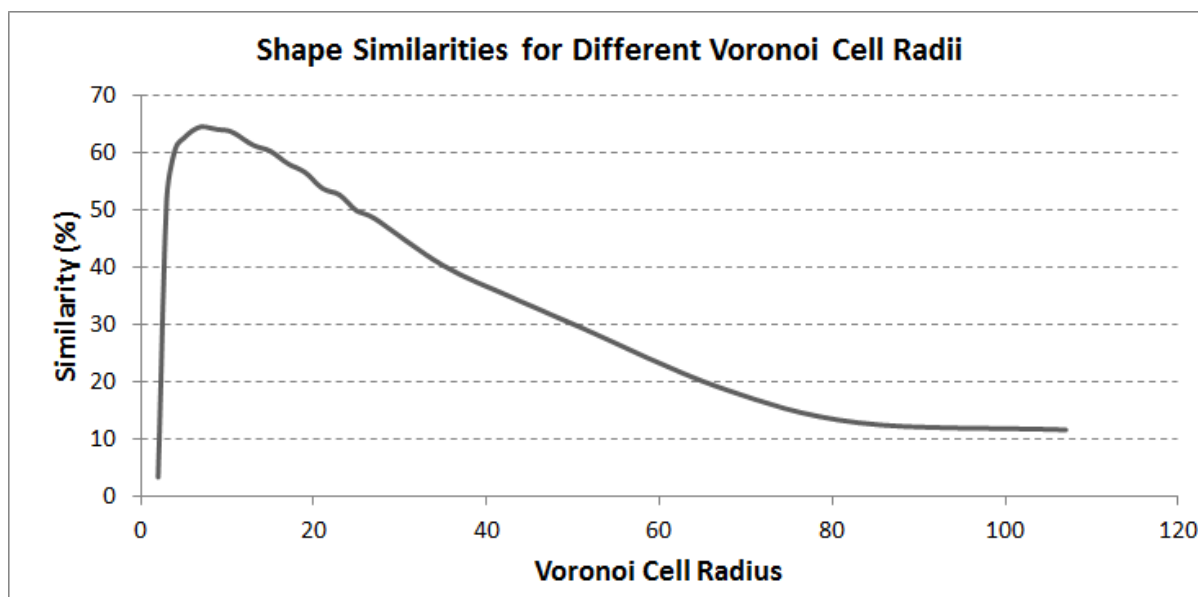


Figure 3.12: Relationship between shape similarity and Voronoi cell radius: the highest similarity is 64.57% when the Voronoi cell radius is 7

Table 3.2: Grid model for Figure 3.11 (c) with different sample rates

Sample Rate	1	2	3	4	≥ 5
Similarity	100.0%	65.5%	37.8%	15.4%	$\leq 0.0\%$
Grid Quantity	9.6×10^8	1.2×10^8	3.6×10^7	1.5×10^7	7.7×10^6

Besides visualization, another important application of the proposed method is numerical simulation, which needs a volume mesh model rather than a surface mesh to describe the rock and its fractures. Mesh with shape similarity above 60% could be considered as an acceptable approximation of the rock image. According to the chart in Figure 3.12, we choose surface meshes generated by $r=15$ where the similarity is 60.3% and the mesh for the major fracture structure is individually shown in Figure 3.13 (a). In fact, the proposed similarity calculation method is a strict measurement. Figure 3.13 (b) includes both the surface mesh Figure 3.13 (a) and the input 3D image Figure 3.11 (c), where the mesh almost completely approximates the structure from the aspect of visualization. Figure 3.13 (c) is the surface mesh with its thickness property. Elements with 0 thickness indicate holes or gaps for the input image model. Taking the surface mesh and corresponding rock boundaries as constraints, a tetrahedral mesh Figure 3.13 (d) is constructed by

the own in-house developed mesh generator. The surface mesh is consistent with the volume mesh, shown in the close-up in Figure 3.13 (d). The volume mesh has 28,631 nodes as well as 143,901 elements. In general, compared with grid models, the generated volume mesh achieves a better similarity with fewer elements with respect to Table 3.2.

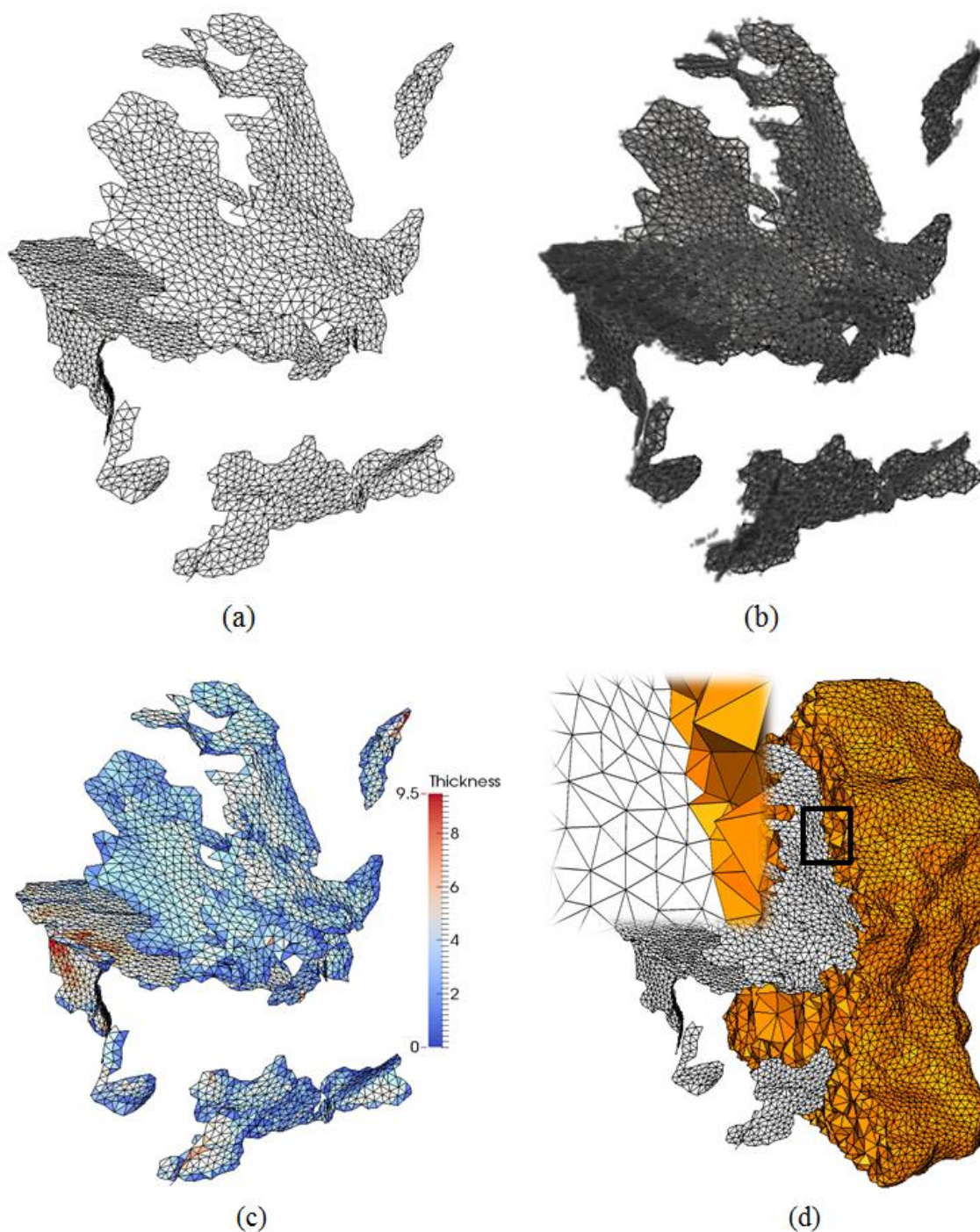


Figure 3.13: Mesh generation for a rock image: (a) surface mesh of the main structure; (b) surface mesh with the input image; (c) surface mesh with thickness property and (d) the volume mesh with 28,631 nodes and 143,901 elements.

In Table 3.3, four methods [173, 174] are adopted to measure the element quality of the generated volume mesh in Figure 3.13 (d). Statistics in Table 3.3 show that the average element qualities of the generated mesh are close to the regular tetrahedron. Consequently, the generated volume mesh model is considered as analysis-suitable for finite element simulation.

Table 3.3: Element quality for Figure 3.13 (d)

Quality Measurement	Minimum Quality	Average Quality	Regular tetrahedron
Minimum Dihedral Angle	8.18°	49.06°	70.53°
Gamma Quality	0.14	0.81	1.00
Edge Aspect	0.20	0.66	1.00
Radius Aspect	0.06	0.84	1.00

3.7.3 The application to a complicated fracture structure

The last example is a 3D fractured rock with a complicated fracture structure. There are 216 major fractures with different thicknesses. Concerning the image of the rock, the resolution is 4 μm and the image size is 1012×1024×609. The fractures within the rock are demonstrated in Figure 3.14 (a) and one slice of the rock fractures is shown in Figure 3.14 (b). According to the above outcomes, Voronoi cell radius $r=7$ is utilized to generate SCVDs for the fractures.

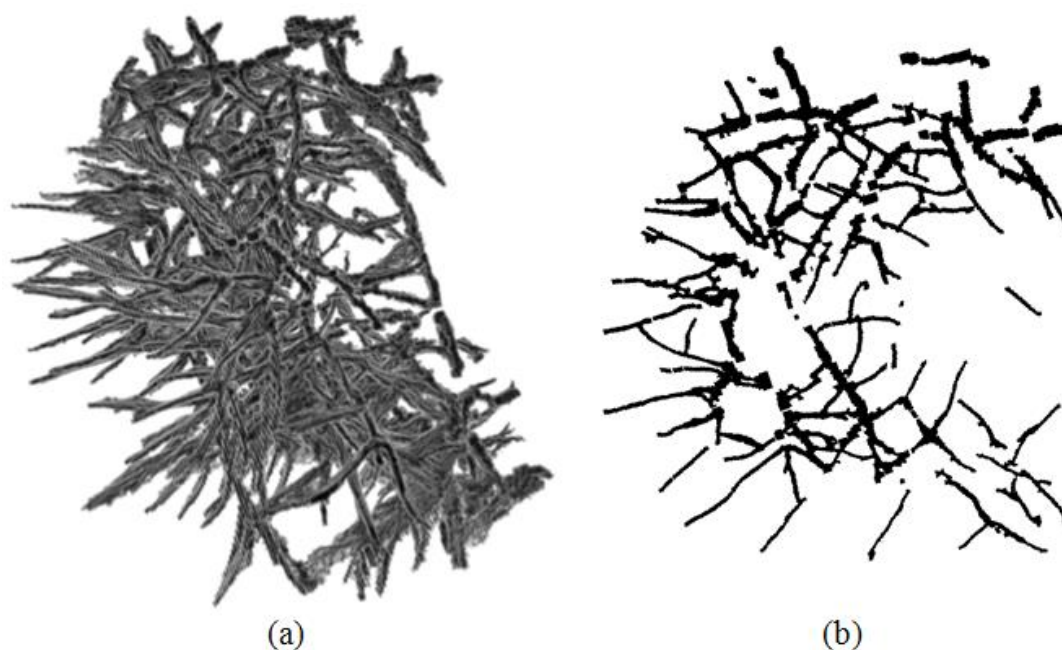


Figure 3.14: Fractures of a rock mass: (a) 216 fractures within the rock and (b) one slice of the fractures.

An appropriate JW threshold is crucial to correctly detect fracture junctions. Moreover, it has a significant impact on the success of umbrella operations. Based on the fractures in Figure 3.14 (a), a serial of numerical experiments are carried out to reveal the relationship between the JW threshold and the percentage of failed umbrella operations. In these experiments, different JW thresholds slightly affect the node quantity in initial meshes, but the amount is approximately 37,000. As shown in Figure 3.15, the percentage of failed umbrella operations rises with the increasing of the JW threshold. The fundamental reason of this trend is that an umbrella operation tends to be successfully implemented to a node if the incident triangles are approximately on a flat disk. A low JW threshold restricts umbrella operations to fracture surface nodes, where the corresponding disks are flat. Therefore, the chance of failure is low. For instance, only 0.1% umbrella operations are failed when the JW threshold is 5. In contrast, high JW threshold leads nodes at junctions involved in umbrella operations. Hence, the operations are likely to fail due to the uneven geometry at junctions. For instance, when $JW=15$ is used as the threshold, the percentage of failed umbrella operations increases to 1.92%.

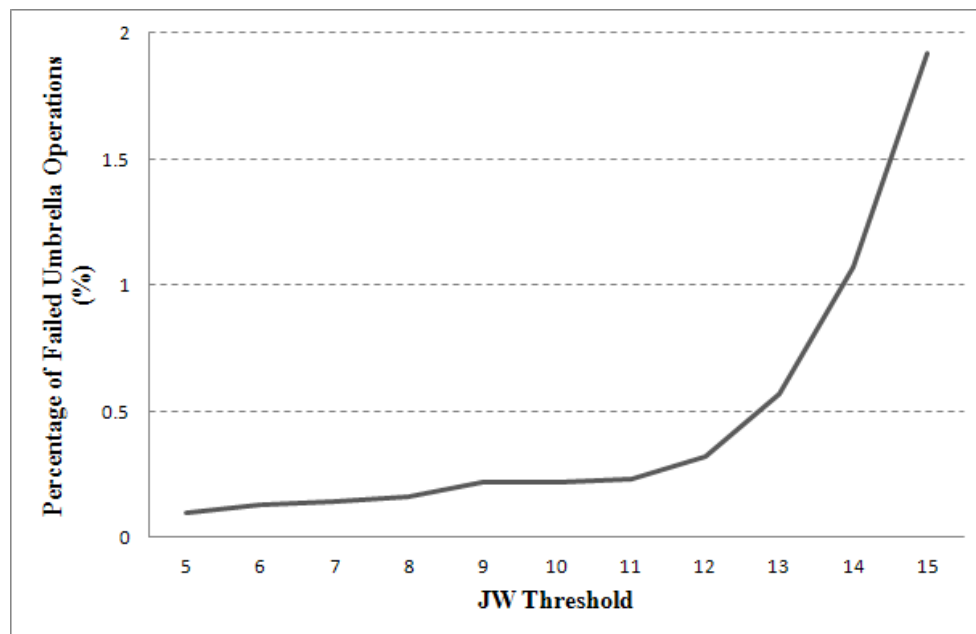


Figure 3.15: Relationship between the JW threshold and the percentage of failed umbrella operations

Besides failed umbrella operations, overlapped junction triangles are the other reason that induces topology and geology flaws concerning VMC (a), (b) and (c). The solution we adopted is discarding all junction triangles of the surface mesh. On the one hand, this solution will remove all possible overlapped junction triangles, but on the other hand, some structures are eliminated from the

junctions. Therefore, a higher junction residual ratio is required concerning the choice of a better JW threshold. Figure 3.16 illustrates the trend of junction residual ratio with the increasing of JW thresholds. A low threshold will identify a large junction zone, thereby leading a low junction residual ratio. On the contrary, a high threshold restricts junction nodes to thin and long areas where fractures meet, and thus the junction residual ratio is high. As seen in the chart, once junction residual ratio is higher than 90%, it increases much slower than that lower than 90%. This phenomenon implies that some common structures are removed from the mesh in spite of the increasing of the threshold. In fact, the removed structures are fracture blocks which should be represented by volume elements rather than surface elements. Therefore, it is reasonable to discard them during the surface meshing process. For this rock mass, junction residual ratios higher than 90% are accepted.

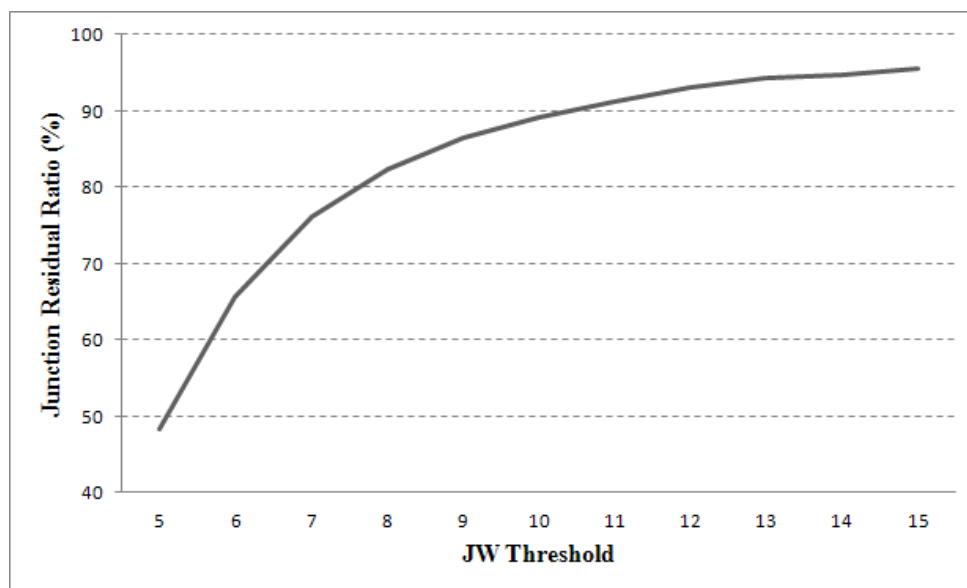


Figure 3.16: Relationship between the JW threshold and the junction residual ratio.

An appropriate JW threshold should satisfy two conditions: lower percentage of failed umbrella operation and higher junction residual ratio. Based on the charts in Figure 3.15 and Figure 3.16, a JW threshold between 10 and 12 is considered as a reasonable choice for this example. It is because the percentage of failed umbrella operations is from 0.22% to 0.32% and the junction residual ratio is over 90%. JW thresholds within this range significantly reduce the manually repairing work and preserve the key geometry features of the fracture junctions. Therefore, we use $JW=11$ as the threshold to generate a surface mesh for representing the fractures in Figure 3.14 (a). The surface mesh result is demonstrated in Figure 3.17 (a) and (b) in different view angles. In the mesh, there are 37,707 nodes including 1897 junction nodes and 35,810 surface nodes. 0.23% umbrella operations are failed during the mesh repairing process. We fix the failed operations manually and

take the surface mesh as constraints to construct a volume mesh for the rock mass. The generated volume mesh Figure 3.17 (c) contains 193,144 nodes and 1,089,010 elements and a close-up is shown in Figure 3.17 (d) to demonstrate the consistency concerning the surface mesh.

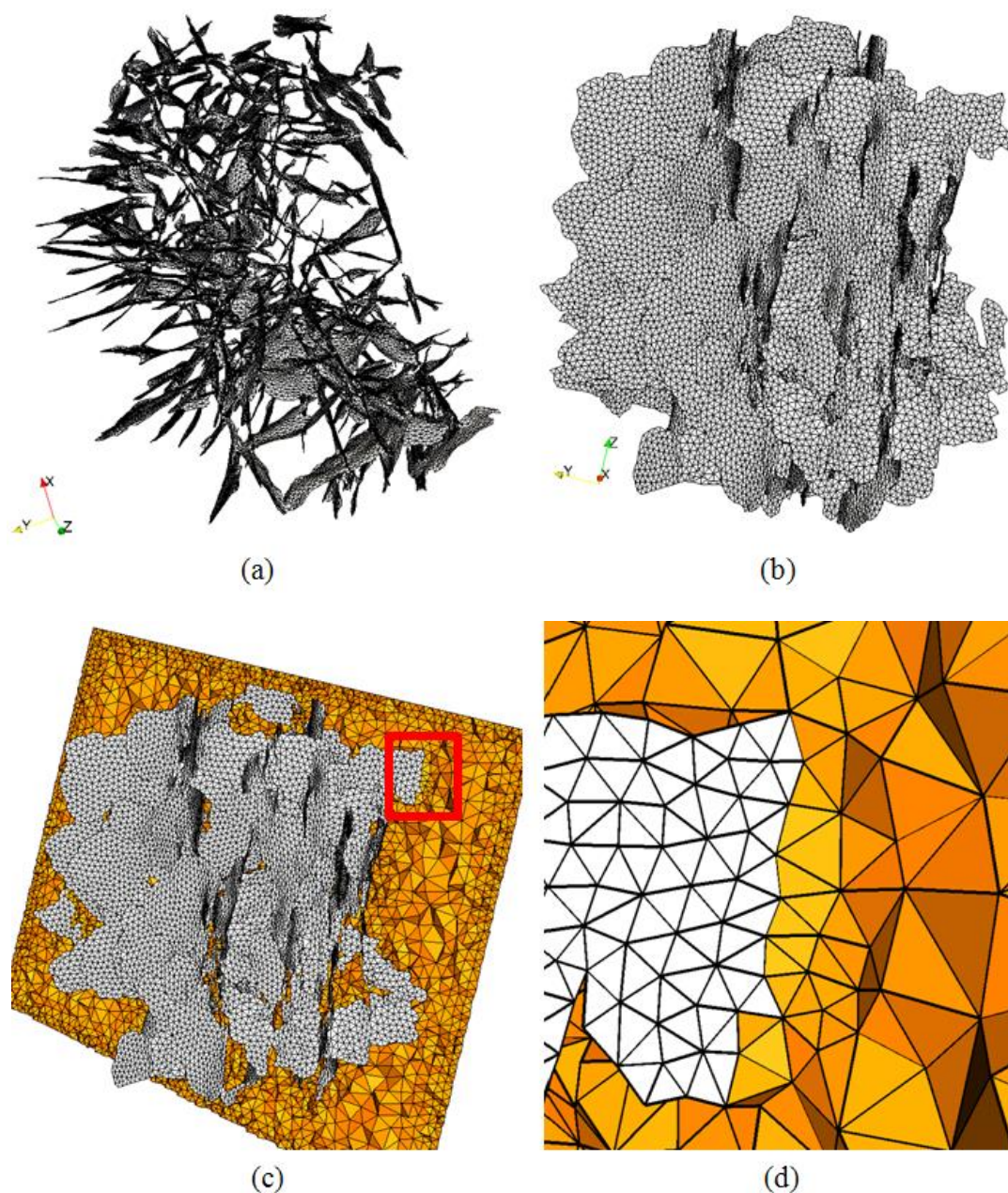


Figure 3.17: Mesh models for the fractures in Figure 3.14: (a) and (b) are the surface meshes with different view angles, (c) is the corresponding volume mesh containing 193,144 nodes and 1,089,010 elements and (d) is a close-up of the part marked in (c).

Concerning the manual repairing work, it is easy to handle as locations where umbrella operation fail can be directly detected by the corresponding surface node indexes. For instance, N in Figure 3.18 (a) is one of nodes with failed umbrella operations and Figure 3.18 (b) is the local mesh which

has been repaired manually. As only the mesh topology is required to be repaired and failed operations are rare, the repairing can be achieved by either directly modifying the data file or using software with mesh repairing functions.

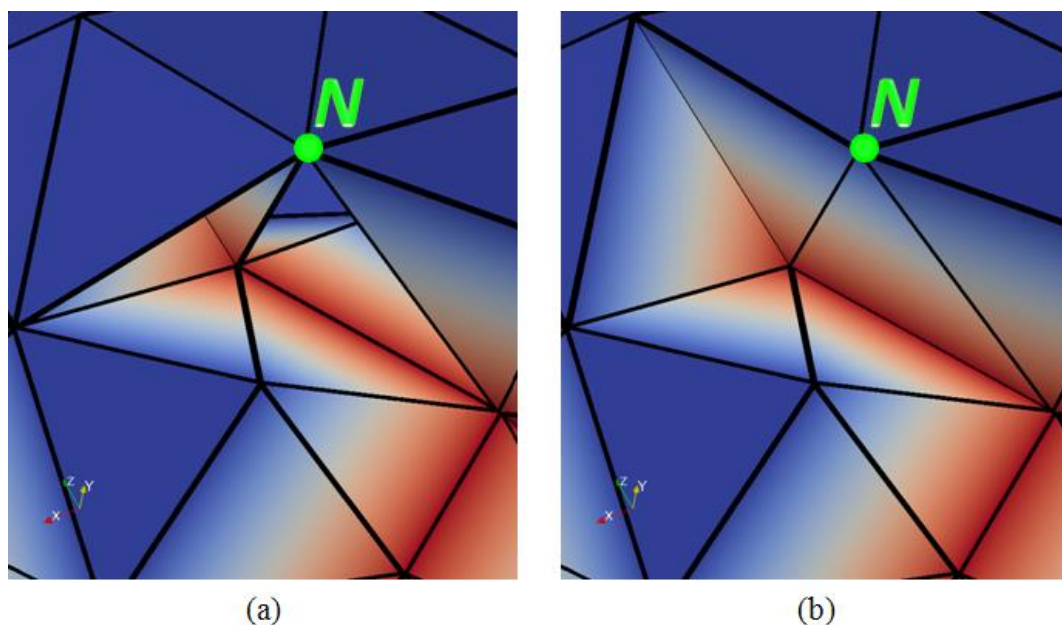


Figure 3.18: Manually repairing a failed umbrella operation: (a) the local mesh before repairing and (b) the local mesh after repairing. Junction node is red and surface node is blue. N is the node where the umbrella operation fails.

In Table 3.4, the element quality of the volume mesh in Figure 3.17 (c) is measured by four different methods [173, 174]. In terms of the average element qualities, they are close to a regular tetrahedron. Thus the mesh model for the fractures could be recognized as an analysis-suitable model for finite element simulation. The minimum element qualities for this model are low, probably due to fractures meeting at sharp angles.

Table 3.4: Element quality for Figure 3.17 (c)

Quality Measurement	Minimum Quality	Average Quality	Regular tetrahedron
Minimum Dihedral Angle	6.87°	47.55°	70.53°
Gamma Quality	0.07	0.78	1.00
Edge Aspect	0.16	0.64	1.00
Radius Aspect	0.02	0.81	1.00

3.7.4 Time efficiency analysis

All the numerical experiments in this chapter are carried out on a super computer in the Centre for Geoscience Computing (<http://earth.uq.edu.au/centre-geoscience-computing>). Table 3.5 demonstrates the computing time used by SCVD construction, surface meshing and volume meshing respectively. Evidently, SCVD construction cost most of the computing time. It is because the 3D images have a huge dataset which requires a long time to process.

Table 3.5: Time efficiency (unit: s)

Dataset	SCVD Construction	Surface Meshing	Volume Meshing
Figure 3.10	6	0.3	2
Figure 3.13	552	10	10
Figure 3.17	303	6	108

3.8 Conclusions

In this chapter, an effective image meshing method is proposed to generate finite element mesh models for rocks with arbitrary fractures. The application examples in real world demonstrate its usefulness and effectiveness.

In terms of data set reduction, the proposed algorithm can generate meshes with less element number than image grids to approximate fractures. For the rock sample, the ratio between the tetrahedral mesh element number and the grid number is 1:6704. A shape similarity measurement is also proposed and the optimal Voronoi cell radius used for generating surface mesh for the rock sample is 7 with the corresponding similarity 64.57%. In practice, surface meshes with shape similarity above 60% are considered as close approximations for fractured rocks.

In terms of effectiveness, we prove that if umbrella operations are successfully implemented to all surface nodes, the generated surface mesh is valid concerning preserving mesh topology structure and representing geometry features of fracture. Although umbrella operations could fail around junctions in extremely complicated fracture structures, an adequate JW threshold can reduce the chance of failure. Based on the numerical experiment results, the range of an appropriate JW threshold is from 10 to 12. We involve JW=11 as the threshold to generate a surface mesh for fractures in the rock mass. As a result, 0.23% of the 35,810 umbrella operations fail and the junction residual ratio is above 90%. Although manually repairing work may be required, it is

limited to the vicinity of failed nodes and easy to achieve. Constrained with the above fracture surface mesh, a tetrahedron mesh model consisting of 193,144 nodes and 1,089,010 elements is constructed and evaluated to represent the rock mass with 216 fractures inside.

The generated surface mesh can be utilized as constraints to generate corresponding volume mesh. The element quality of the volume mesh is high concerning a variety of measurements and the element quantity is reasonable for future finite element simulations. In general, the generated mesh models are competitive with grid models and have wide applications in both visualization and finite element simulation.

Chapter 4 Three-Dimensional Mesh Generation for a Geological Reservoir

4.1 Overview

With the advanced field observation, image and drilling technology, geological structure of reservoirs can be described in more details. Geological reservoirs in voxel format are popular and somewhat 3D digital images. Concerning application of such reservoir models to FEM-based applications, there are two difficulties: (1) the complicated stratigraphic surfaces and (2) the huge data set of reservoir models.

In this chapter, we carry out a strategy for meshing 3D geological reservoirs with arbitrary stratigraphic surface constraints. To handle complicated geometries on stratigraphic surfaces, a geodesic-based procedure is designed to provide a robust implementation. Regarding reduction of data set, an advancing front technique is proposed to achieve adaptive surface remeshing, which not only decreases the element quantity but also increases the element quality.

The implementation of the proposed strategy includes the following steps: model import, stratum interfaces and constraints extraction, background mesh generation, surface remeshing and volume mesh generation. The workflow is shown in Figure 4.1.

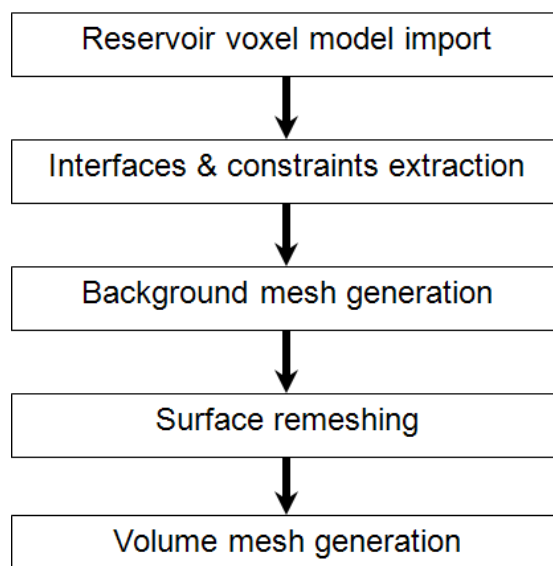


Figure 4.1: Workflow of the proposed method.

A reservoir geological model of the Lawn Hill in Queensland, Australia is converted to a mesh by the proposed method. The data set of the original model is reduced from 7.1×10^7 voxels to a volume mesh with only 1.7×10^5 nodes. Moreover, the element quality of the generated mesh is high, which is analysable for FEM-based applications.

4.2 Background mesh generation

The background mesh generation begins with a surface extraction. Because surfaces representing interfaces of strata are essential for describing geo-objects and generating mesh models, they are initially extracted by multi-material marching cubes algorithm [175]. As shown in Figure 4.2, surfaces are extracted in the format of triangular meshes and their junctions (i.e. constraints) are indicated by bolder lines. Along these constraints, the initial meshes are separated from each other.

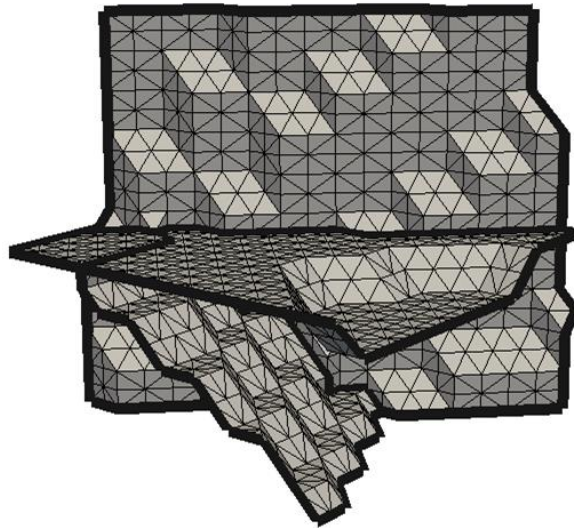


Figure 4.2: Surfaces extracted from a reservoir model. The border lines indicate surface junctions.

Concerning a separated surface mesh, its topology structure is manifold. The above junctions become boundaries of the surface mesh and constraints in the downstream processes. To remesh current surface with a desired element quality and quantity, a size field is required which could be constructed on the surface mesh. Specifically, junction lines are firstly segmented by a customized size S_{seg} which is also the size of nodes on the constraints and then size h_i for node i within the background mesh is calculated by the following function.

$$h_i = \frac{\sum s_j / l_{i,j}}{\sum 1.0 / l_{i,j}}, \quad s_j = S_{\max} \cdot t + (1.0 - t) \cdot h_j, \quad t = \frac{l_{i,j} \cdot (1.0 - q)}{h_j - S_{\max} \cdot q} \quad (4.1)$$

Where node j is one of the vicinities of i , $l_{i,j}$ is the distance between node i and j , h_j is the size of node j , S_{\max} is the expected maximum size, q is the gradation ratio. Once a size field is obtained, the length $e_{i,j}$ of edge (i, j) is defined by the sizes of its two ends (i.e. node i and j).

$$e_{i,j} = \frac{2l_{i,j}}{h_i + h_j} \quad (4.2)$$

4.3 Surface remeshing

The basic idea of the surface remeshing approach is iteratively creating geodesic isolines [30] from boundaries to the interior of the stratigraphic surface mesh. In the iteration, the coming isolines are named as fronts. The key technique of the remeshing is the generation of fronts, which includes the following steps: (1) detection zone generation; (2) front mergence; (3) front construction and (4) surface mesh generation.

4.3.1 Detection zone generation

Region between two adjacent fronts is somewhat a belt and its width is defined by a customized parameter ζ . A layer of nodes in front of the current front forms a detection zone (DZ) and the width of DZ is ζ . Although ζ must be larger than ζ concerning the later collision detection, large ζ could induce heavy geodesic distance calculation and cost long CPU time. Therefore, it is crucial to choose an appropriate choice of ζ with regard to the efficiency of the detection zone generation.

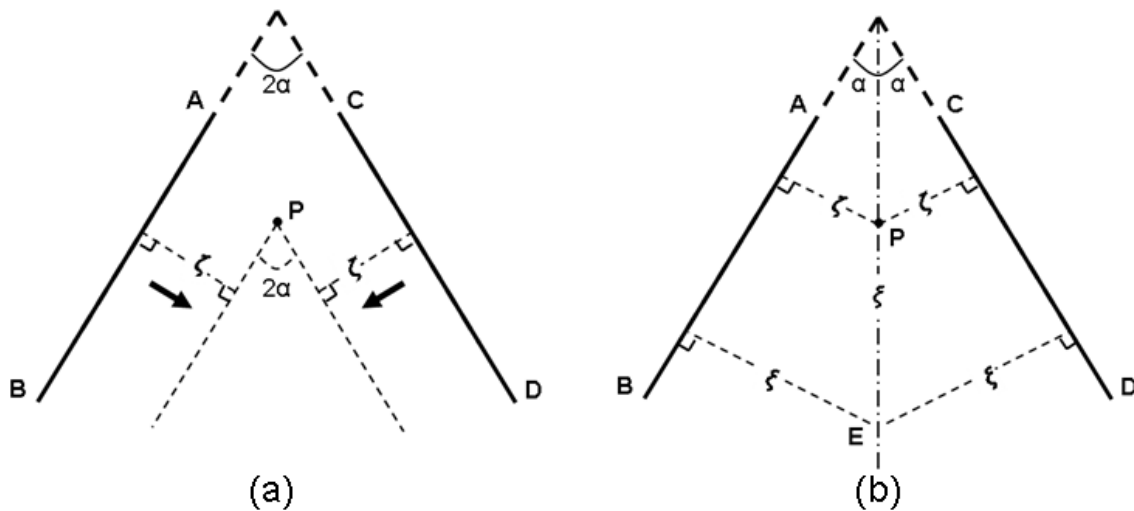


Figure 4.3: The appropriate choice of ζ for front generation.

As shown in Figure 4.3 (a), AB and CD are current fronts and the angle between them is 2α . With nodes on AB and CD as source (where geodesic distance is 0), front AB and CD are propagated by a distance ζ . P is the intersection of new fronts. If 2α is too sharp, the quality of elements around P will be poor. To smooth the new front and improve element quality, nodes around P will be utilized as new source to update related geodesic distances in DZ. It is expected that the updated nodes are still in DZ. As shown in Figure 4.3 (b), when P is taken as a new source, E is the farthest node affected by P and the distance between them is ξ . Therefore, ξ could be calculated by the following formula.

$$\xi = \frac{\zeta}{1 - \sin(\alpha)} \quad (4.3)$$

In this document, we choose $\alpha=45^\circ$, hence ξ is approximately 3.4ζ .

A mesh example is illustrated to demonstrate the geodesic distance updating process with different ξ . As shown in Figure 4.4 (a) and (b), current fronts are the legs of a isosceles triangle; DZ is represented by colours from light-blue (low distance) to light-red (high distance); nodes in deep blue are non-calculated; the green point is the intersection point P ; area in deep red indicates nodes updated by P . Figure 4.4 (a) is the result of $\xi = \zeta$ and a portion of the nodes in red are not in DZ. In contrast, if $\xi = 3.4\zeta$, the updated nodes are all in the DZ as shown in Figure 4.4 (b).

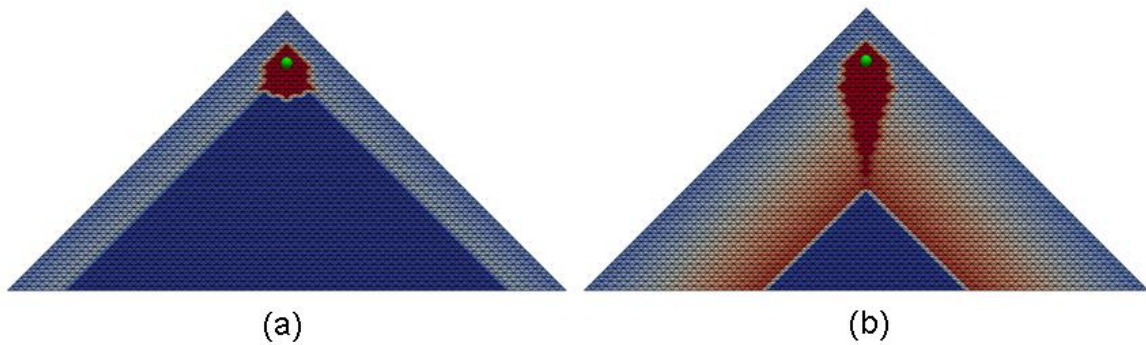


Figure 4.4: geodesic distance updating with different DZ widths: (a) $\xi = \zeta$; (b) $\xi = 3.4\zeta$

4.3.2 Front mergence

The front mergence process is utilized to address collisions when two fronts encounter, which is indirectly achieved by DZ updating. Specifically, a set of collision nodes in DZ are firstly detected by their geodesic distance information. Then the collision-related nodes are treated as new source to

update DZ. The detection and updating process are invoked alternatively until no collisions exist in DZ.

Collision detection

After generating DZ by ζ , every node n in DZ contains a geological distance $G(n)$. For instance, node P (in Figure 4.5) has 8 vicinities v_i ($i=1, 2, \dots, 8$). Vector V_i ($i=1, 2, \dots, 8$) are the geological distance increasing speed from v_i to P and are defined as below:

$$V_i = \frac{G(P) - G(v_i)}{|P - v_i|} \cdot \frac{P - v_i}{|P - v_i|} \quad (4.4)$$

The collision detector vector (CDV) of node P is defined by $C(P)$.

$$C(P) = \frac{\sum V_i}{\sum |V_i|} \quad (4.5)$$

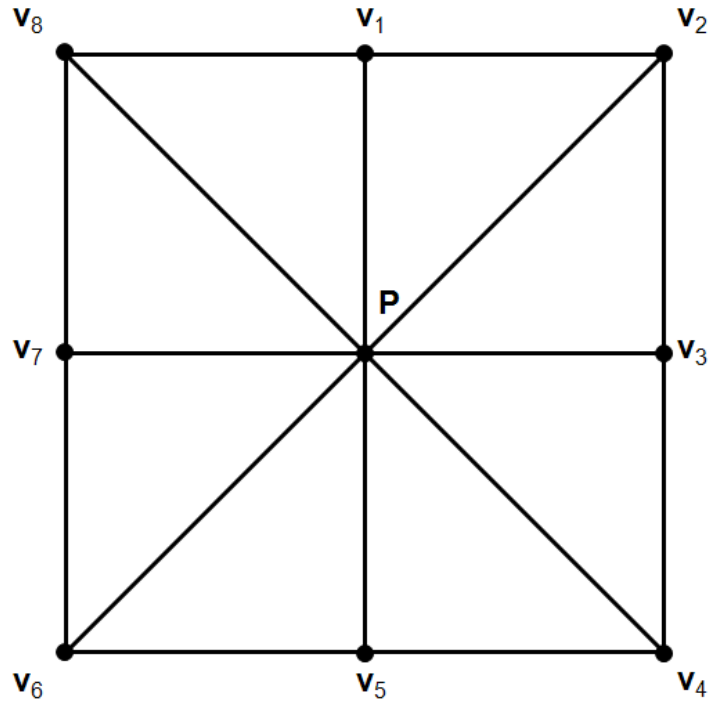


Figure 4.5: A node P and its 8 vicinities v_i ($i=1, 2, \dots, 8$).

As shown in Figure 4.6 (a), the two green points are the source where geological distance is 0. DZ is generated by ζ and colours indicate the magnitude of node CDVs. The close-up in Figure 4.6 (b) reveals that potential collision nodes always have small CDVs. Therefore, the detection of collisions is achieved by checking the magnitude of CDV. Based on our numerical experiments, a node P is a collision node if it satisfies the following criteria:

$$\begin{cases} 0.7 \leq G(P) \leq 1.2 \\ |C(P)| < 0.45 \end{cases} \quad (4.6)$$

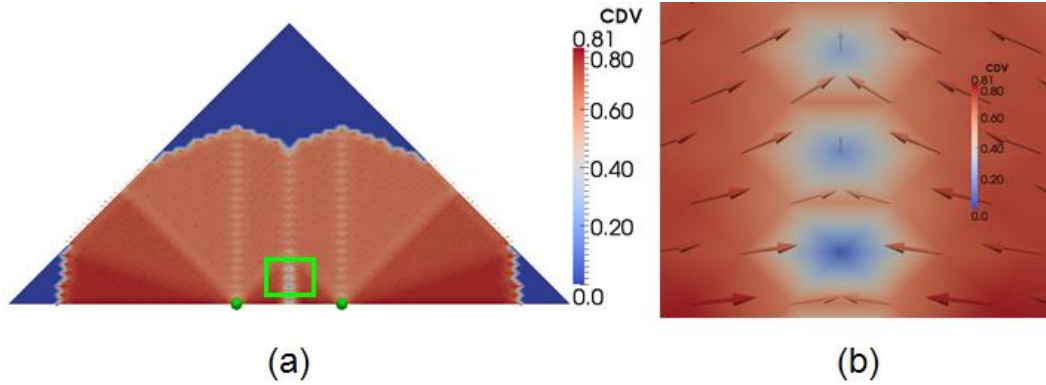


Figure 4.6: collision detection: (a) DZ is generated according to the source points which are in green. Colours indicate the magnitude of node CDVs; (b) a close-up of (a).

Detection zone updating

The updating process has two functions: (1) merging fronts and (2) smooth new front. In Figure 4.7, the current fronts are AB and CD while P is the collision node. PE is the perpendicular to AB through E and PF is the perpendicular to CD through F . Nodes on EF are collision-related, which is utilized as new source to update DZ. As a result, AB and CD are merged together by EF . Besides, the next front will be parallel to polyline $BEFD$, which avoids generating sharp angles.

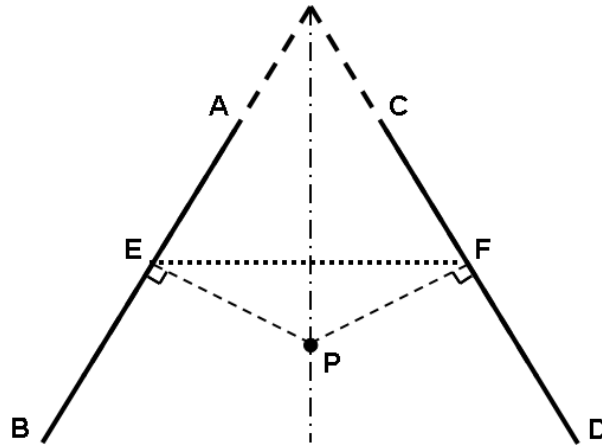


Figure 4.7: DZ mergence.

Geodesic path is utilized to calculate EF (in Figure 4.7) for the implementation of DZ mergence to a triangular surface. As shown in Figure 4.8 (a), the two green points are the initial source and the DZ is generated by $\zeta = 3.4\zeta$, where $\zeta = 8.5$ is the customized belt layer width. New belts are indicated by

bright blue and they encounter around the middle of the source points. To achieve the front merging operation, collision-related nodes are collected as new source to update the DZ and the result is shown in Figure 4.8 (b). Consequently, the two belts in Figure 4.8 (a) are merged into one in Figure 4.8 (b) and the fronts are merged together as well.

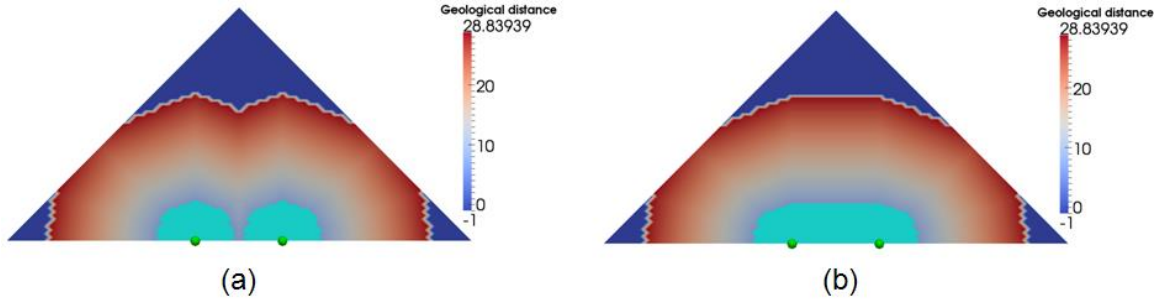


Figure 4.8: Front merging: (a) the green points are source and bright blue zones are current layer;
(b) the result of detection zone updating.

4.3.3 Front construction

Boundaries of the belts are actually the new fronts. As shown in Figure 4.9 (a) and (b), the two green points are source nodes. The fronts are constructed based on $\zeta=8.5$ and $\zeta=4.3$ respectively. In Figure 4.9 (b), there are two fronts in the first two layers. In the third layer, the fronts encounter with each other and then the merge happens as shown in Figure 4.9 (b).

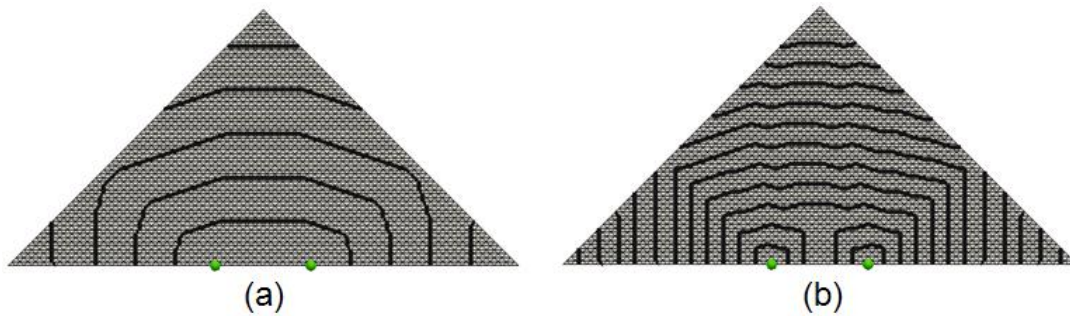


Figure 4.9: Front construction: (a) two green points are source and belt width is $\zeta=8.5$; (b) belt width is $\zeta=4.3$

4.3.4 Surface mesh generation

The generated geodesic isolines divide the surface into a number of belts. Triangular elements are independently constructed for each belt, which is based on the background mesh established by Formulas 4.1 and 4.2. Specifically, boundaries of a belt in Figure 4.10 (a) are firstly segmented with

length 1 and the belt width is set as $\zeta = 2$. In the next stage, a front propagation method [31] is employed to generate a Voronoi diagram (in Figure 4.10 (b)) for the belt. As shown in Figure 4.10 (c), a triangular mesh is created in the final step according to the Voronoi diagram.

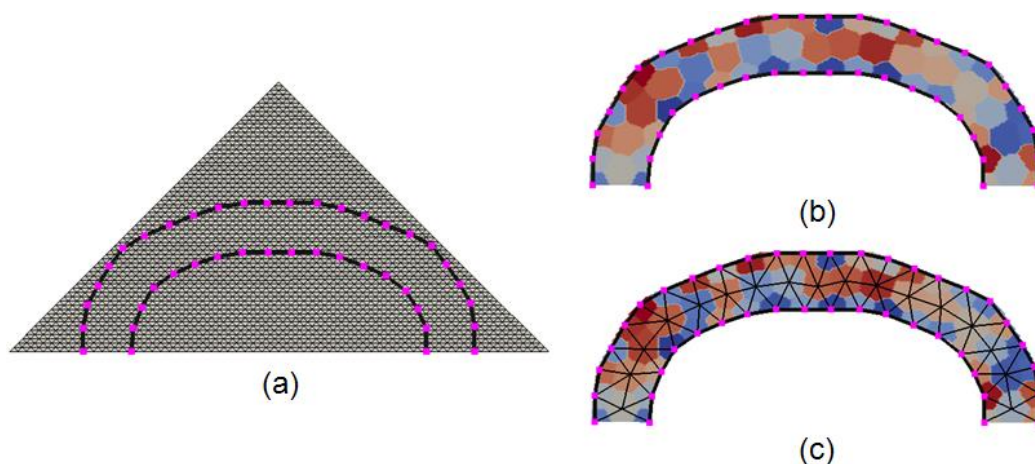


Figure 4.10: Triangular mesh generation for belts: (a) the segmented fronts; (b) the Voronoi diagram for the belt; (c) triangular mesh of the belt.

4.4 Volume mesh generation

Taking the above surface meshes as constraints, a tetrahedral mesh is generated to represent the corresponding reservoir model. Based on tetrahedral mesh techniques[73, 84], our own in-house developed mesh generator is employed to adaptively create elements from the boundaries to the interior.

4.5 Numerical applications

A reservoir geological model of Lawn Hill in Queensland of Australia is utilized to demonstrate the capability of the proposed meshing method.

4.5.1 Lawn Hill and its geological model

Lawn Hill platform lies in the Northwestern Queensland, Australia. The Isa superbasin within this platform hosts the world-class Century Zn-Pb-Ag deposits and is also well known for the Iron Oxide Copper and Gold deposits. The mineral exploration and related subjects attract interests of numerous researchers [176-178]. Integration of the knowledge- and data-driven models is considered as an effective way to assist the resource exploration and environmental assessment.

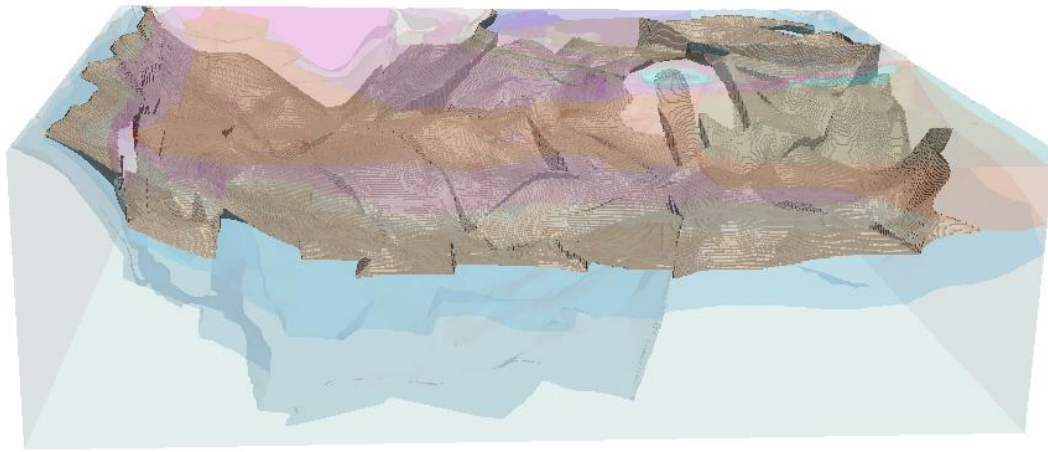
Lawn Hill model constructed by using GoCAD (Figure 4.11) is taken here as an application example. It covers $140.5 \times 161.5 \times 19.4 \text{ km}^3$ (where depth is doubled in the visualization data) and is described by a 3D digital image with 7.1×10^7 voxels (Figure 4.11).



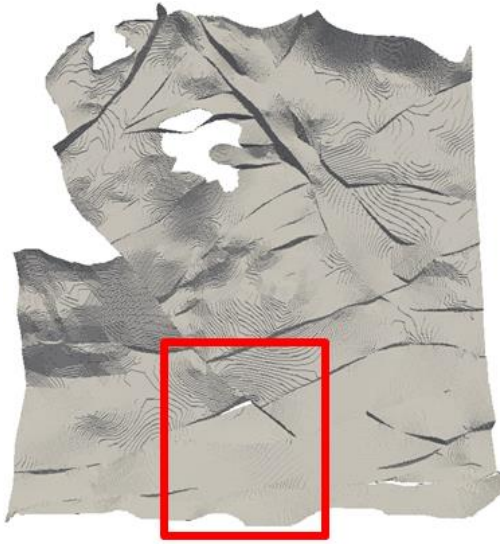
Figure 4.11: The Lawn Hill model which is built by GoCAD with 7.1×10^7 voxels.

4.5.2 Surface remeshing for the Lawn Hill model

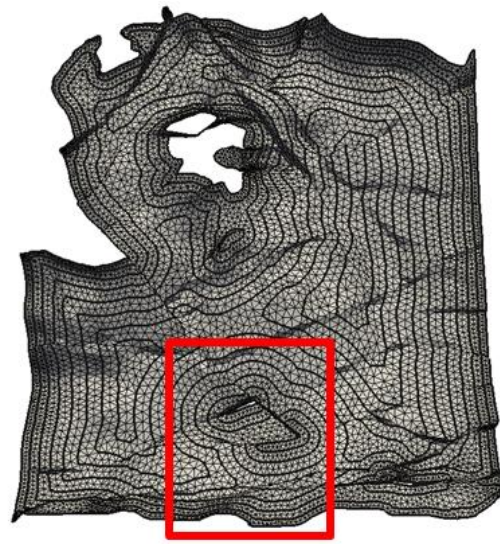
In Figure 4.12 (a), a stratigraphy surface is utilized to demonstrate the proposed surface remeshing approach. The initial surface mesh is extracted by the marching cube method [175] and shown in Figure 4.12 (b). Due to the inherent of 3D images, the mesh is staggered, which is shown in its close-up in Figure 4.12 (d). Besides, it contains a huge number of elements which is 2.8×10^6 . Compared with Figure 4.12 (b), there is only 1.5×10^4 elements in the mesh (Figure 4.12 (c)) generated by the proposed remeshing method. Moreover, as the remeshing method takes the advantages of geodesic isolines highlighted by bold lines in Figure 4.12 (c), the created elements are aligned and parallel to the boundaries. To demonstrate the process of front mergence in detail, a close-up of Figure 4.12 (c) is shown in Figure 4.12 (e). Isolines in blue independently propagate from the boundaries of two holes towards the interior. When these two isolines encounter with each other, the front mergence is invoked to merge them into one which is highlighted in red.



(a)



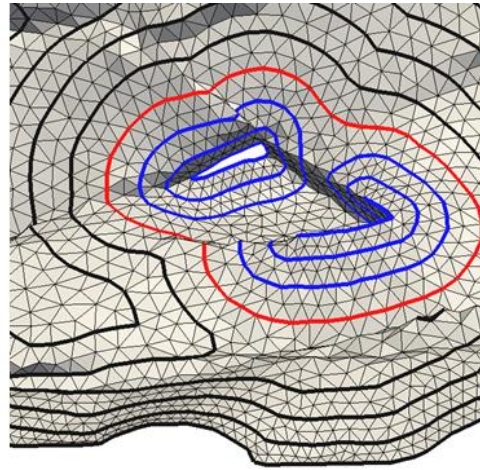
(b)



(c)



(d)



(e)

Figure 4.12: Remeshing for a rock stratum interface: (a) is a stratigraphy surface; (b) is the surface mesh (2.8×10^6 elements) extracted by the marching cube method [175]; (c) mesh (1.5×10^4 elements) created by the proposed remeshing method; (d) and (e) are the close-ups of (b) and (c) respectively.

Figure 4.13 shows the ability of adaptive mesh generation which are controlled by parameters in Formula 4.1 and 4.2. The surface mesh in Figure 4.12 (a) is remeshed by three groups of parameters and Figure 4.13 (a)-(c) and their close-ups (d)-(f) are the meshes affected by the parameters. Comparing Figure 4.13 (a) with (b), they have the same $S_{max}=20$ and $S_{seg}=2.5$ but different q which is 1.1 in (a) and 1.2 in (b). As small q leads to a low gradation, the element size in Figure 4.13 (a) increases slower than that in Figure 4.13 (b). In terms of the parameters S_{max} and S_{seg} , they affect the element size and quantity of meshes. For instance, Figure 4.13 (c) is generated by $S_{max}=30$ and $S_{seg}=5$ which are larger than that of Figure 4.13 (a) and thus the mesh is sparser compared to the mesh of Figure 4.13 (a). Additionally, the element numbers of Figure 4.13 (a) and (c) are 12,872, and 5,639 respectively.

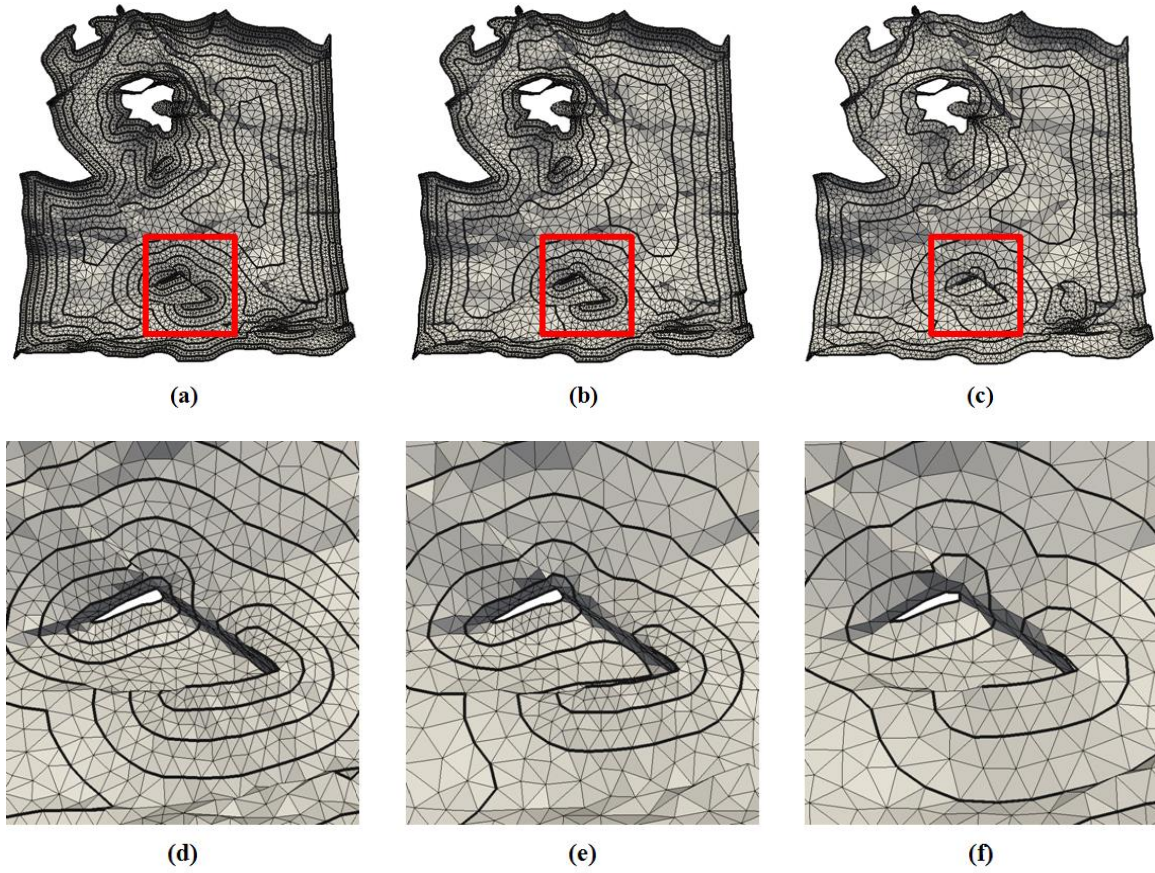
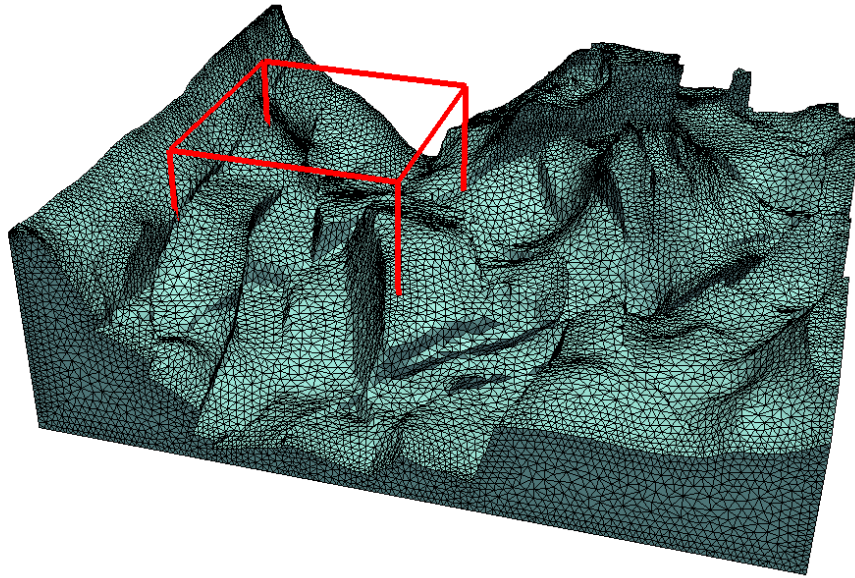


Figure 4.13: Remeshing by different size fields: (a) $S_{max}=20$, $q=1.1$ and $S_{seg}=2.5$; (b) $S_{max}=20$, $q=1.2$ and $S_{seg}=2.5$; (c) $S_{max}=30$, $q=1.1$ and $S_{seg}=5$; (d), (e) and (f) are the close-ups of (a), (b) and (c) respectively.

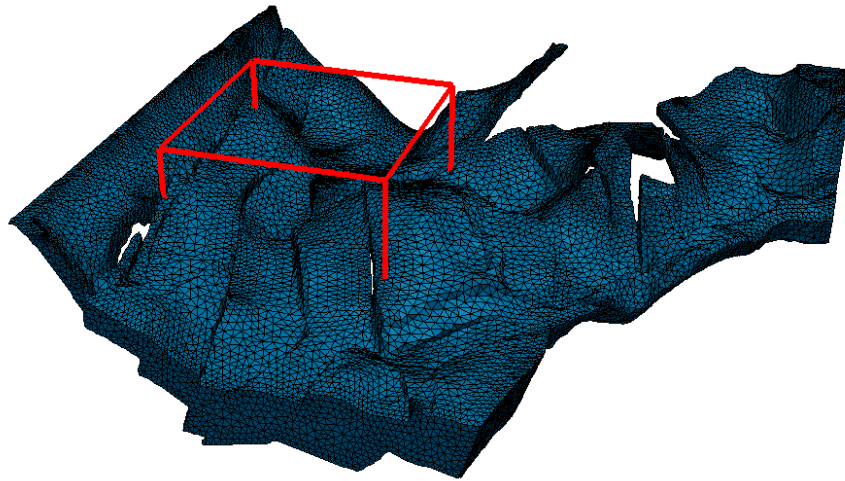
4.5.3 Volume mesh generation for the Lawn Hill model

Stratigraphy surface meshes are utilized as constraints to generate a volume mesh for the reservoir

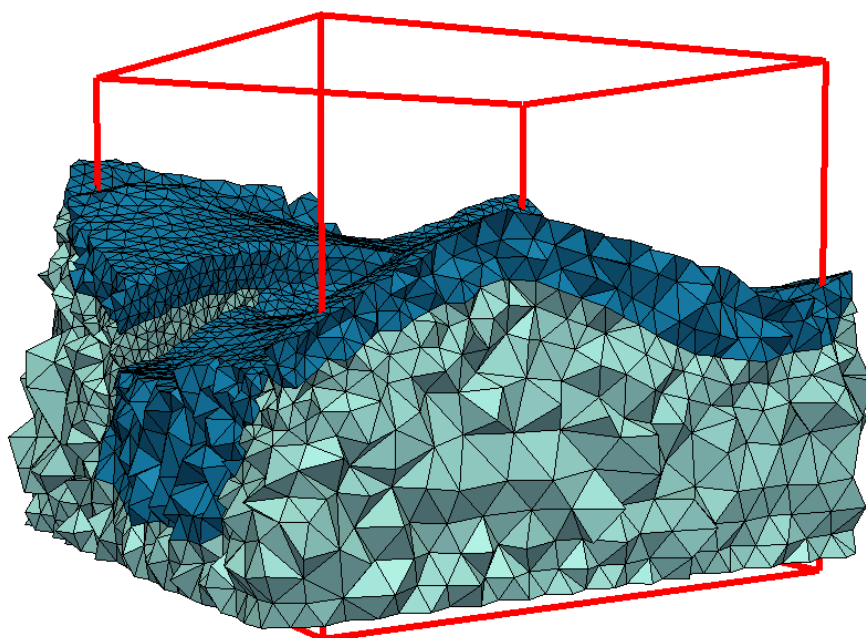
model. As shown in Figure 4.14 (a) and (b), they are two adjacent strata which are meshed by the proposed method respectively. Figure 4.14 (c) is a close-up of the volume meshes demonstrates the mesh consistency.



(a)



(b)

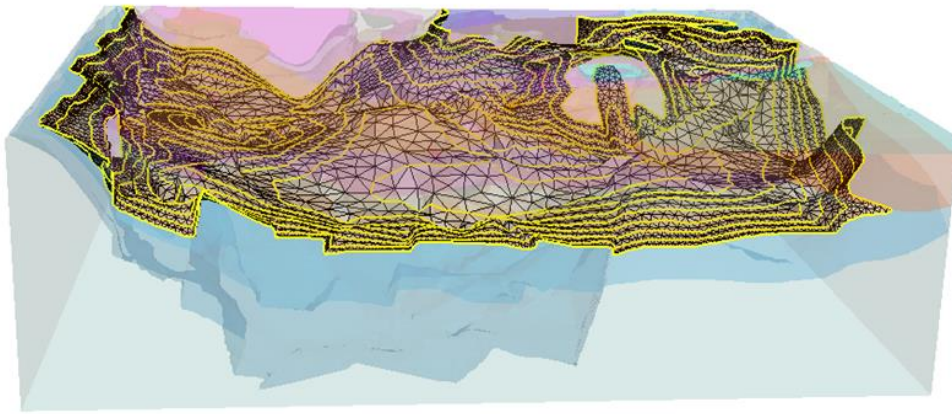


(c)

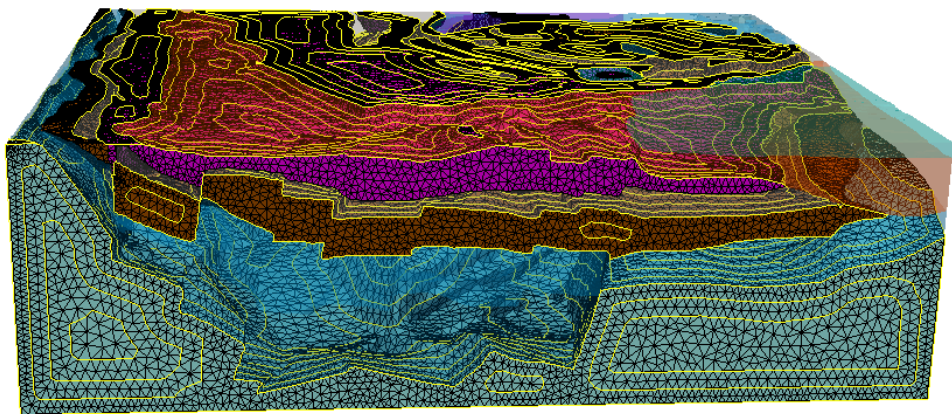
Figure 4.14: Volume mesh generation for the reservoir model: (a) and (b) are two adjacent strata; (c) is a close-up of the volume meshes.

4.5.4 Integrated meshing process for the Lawn Hill model

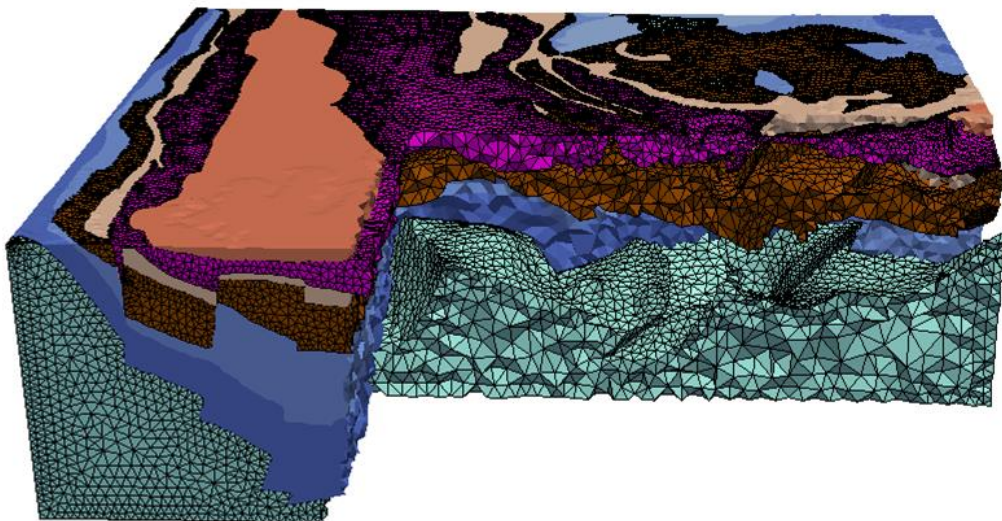
We achieve the process of meshing the Lawn Hill model on a super computer in the Centre for Geoscience Computing (<http://earth.uq.edu.au/centre-geoscience-computing>). In total, the surface mesh generation costs 106 minutes and the volume mesh generation costs 77 seconds. The integrated process of mesh generation for the Lawn Hill model is demonstrated as below. Firstly, the interfaces of rock strata are extracted and meshed by the proposed method. One of such interface meshes is shown in Figure 4.15 (a). Secondly, these interface meshes are combined together according to constraints. Figure 4.15 (b) is the combined surface mesh with 9.0×10^4 nodes and 1.9×10^5 elements. Lastly, taking Figure 4.15 (b) as input, the tetrahedral volume mesh is generated in Figure 4.15 (c). The volume mesh has only 1.7×10^5 nodes and 9.7×10^5 elements, which is much smaller than the original voxel model (7.1×10^7 voxels). Additionally, the 10 components of this model and their volume meshes can be identified in the volume meshing process, which are illustrated in Figure 4.15 (d).



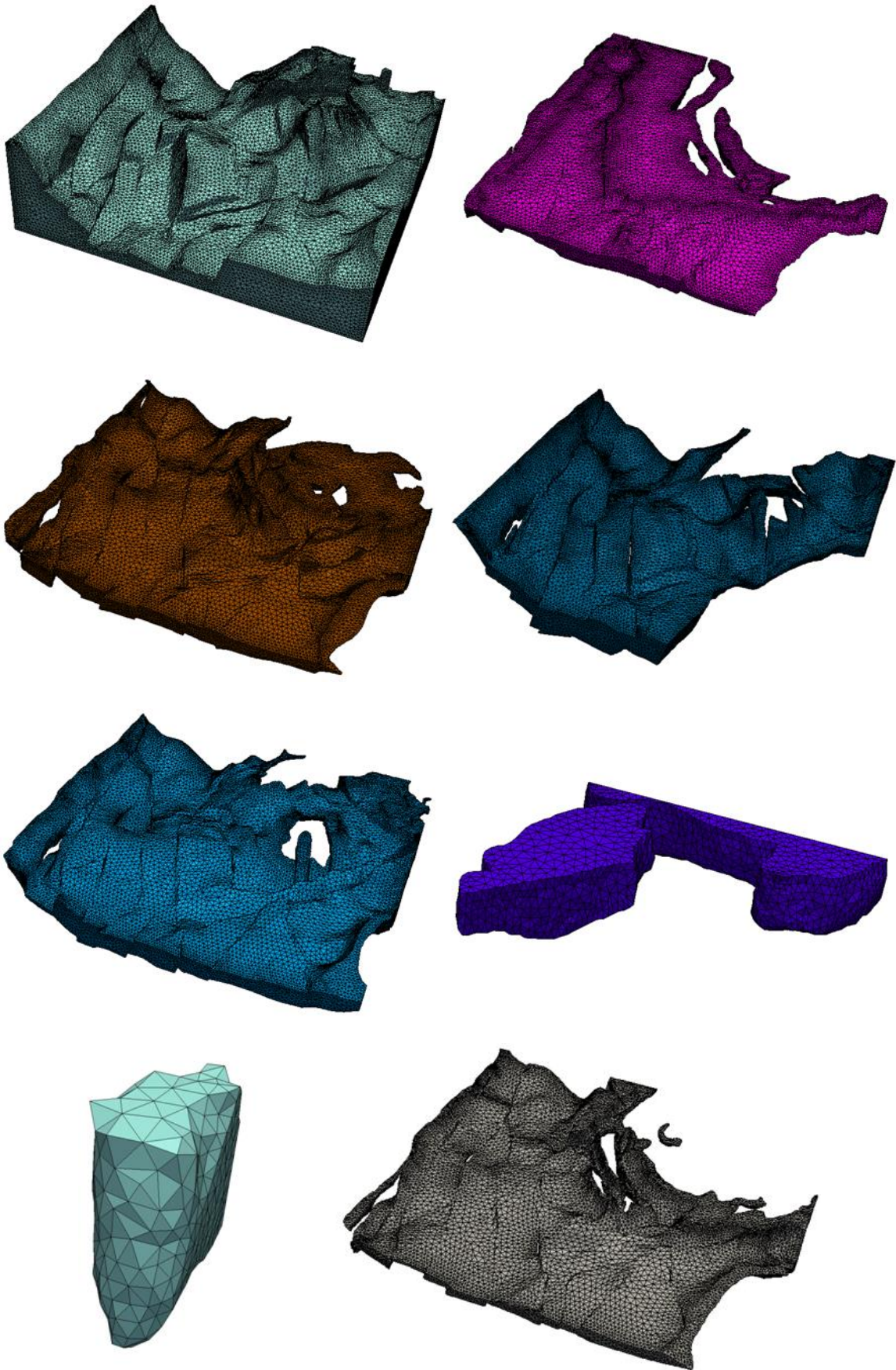
(a)



(b)



(c)



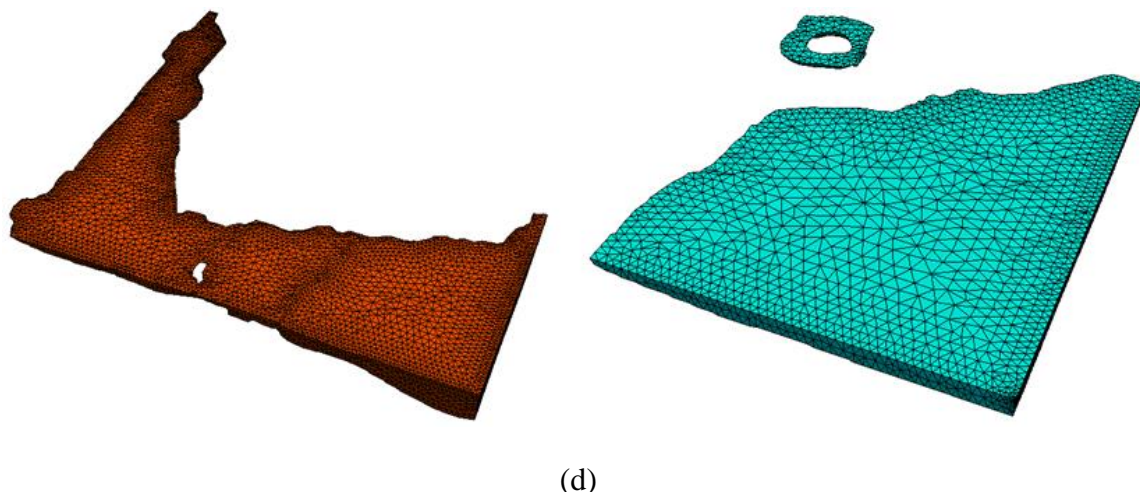


Figure 4.15: Lawn Hill geological model: (a) a rock stratum interface remeshed by the proposed method; (b) the surface mesh; (c) the volume mesh with 1.7×10^5 nodes and 9.7×10^5 elements; (d) 10 meshed components of the geological model.

In Table 4.1, four methods [173, 174] are adopted to measure the element quality of the generated volume mesh in Figure 4.15 (c). The average element qualities of the volume mesh are close to that of a regular tetrahedron, which are considered as analysis-suitable for future FEM-based applications.

Table 4.1: Element qualities of mesh in Figure 4.15 (c)

Quality Measurement	Minimum Quality	Average Quality	Regular tetrahedron
Minimum Dihedral Angle	3.18°	44.43°	70.53°
Gamma Quality	0.03	0.74	1.00
Edge Aspect	0.08	0.61	1.00
Radius Aspect	0.01	0.77	1.00

4.6 Conclusions

This paper proposes an approach for meshing 3D geological reservoir models with arbitrary stratigraphic surface constraints. The approach has been successfully applied to generate mesh for a Lawn Hill reservoir model. Based on the numerical results, the following conclusions are drawn:

- (1) The proposed geodesic-based surface remeshing approach is effective in generating aligned

elements parallel to surface junction lines. The front mergence technique together with detection zone generation can robustly generate elements on stratigraphic surface with complicated geometries.

(2) The remeshing process can be flexibly controlled customized parameters such as the gradation ratio q , the allowable maximum mesh size S_{\max} and the allowable maximum boundary segment size S_{seg} . Specifically, large gradation ratio q leads to a high gradation. Maximum element size S_{\max} and boundary segment size S_{seg} control the element quantity and the larger they are, the less the element quantity is.

(3) Compared with the model in voxel format, the generated mesh model has smaller data set. For instance, the data set of the Lawn Hill model is reduced from 7.1×10^7 voxels to a volume mesh with only 1.7×10^5 nodes. Besides, the element quality of the generated mesh is high concerning four different measurements, which is analysable for FEM-based applications.

Chapter 5 An Adaptive Remeshing Approach for Geological structure with Stratum Interface Constraints

5.1 Overview

With the development of geological modelling and computing techniques, geological structure of reservoirs can be described in more details and the corresponding numerical simulations allows for better engineering process ahead of design [2]. Different from meshes with a single material, geological mesh models have several strata and the stratum interfaces are needed to be clearly represented and preserved at any steps of numerical simulation. Regarding remeshing, it is difficult in itself [154-159] and the requirement of maintaining stratum interfaces makes it more challenging. Besides, working areas in geo-engineering always introduce fine elements to describe area of interesting in the corresponding mesh model. How to adapt these elements to the existing model is another issue of remeshing for geological analysis. Therefore, the objective of this chapter is to develop an adaptive remeshing approach which is conformable to stratum interfaces.

Particularly, both 2D and 3D algorithms are carried out to achieve a comprehensive solution for remeshing with the consistency of stratum interfaces. In 2D, nodes close to interfaces are repositioned on these interfaces during the centroidal Voronoi diagram construction. In 3D, the stratum interfaces are remeshed respectively, which take account of effects of working areas in geo-engineering. A volumetric mesh generation is proposed, which consists of a constrained Delaunay triangulation and an adaptive long-edge breaking strategy. As the remeshing for a geological structure is complicated, a number of current meshing techniques such as surface remesh [28], centroidal Voronoi diagram [29], boundary recovery [74, 179] as well as mesh optimization methods [180-182] are integrated into our approach to achieve the goal of adaptive remeshing. At the end of this chapter, remeshing applications in a near well bore drilling and a long wall mining model are utilized to demonstrate the capability of the proposed remeshing approach..

5.2 Mesh density control and centroidal Voronoi diagram

5.2.1 Mesh density control

To simulate dynamic processes such as drilling and caving in geo-engineering, the adaptive remeshing should have an ability to effectively involve bore holes or working faces into geological models. Concerning areas of interest, a relatively small element size is expected to achieve an accurate analysis. An appropriate size map is applied to adapt these small element size to the existing mesh model. In this chapter, the size map H is an association of a global structure size map H_g and a local size map H_l . Besides, H is restricted by a customized minimum size S_{min} . Formally, the element size of a point P is defined as below.

$$H(P) = \min(H_g(P), H_l(P)), \text{ if } H(P) < S_{min}, \text{ then } H(P) = S_{min} \quad (5.1)$$

The detection of remeshing zone is an essential issue. In 3D domain, this zone is governed by an elliptic cylinder as shown in Figure 5.1. On its surface ellipse, $2f$ is defined by the length of diameter of a well or the width of a working face. The semi-major axis a and the cylinder height h are obtained by the following equation.

$$h = d + b, a = f + b, b = \frac{S_{min} - q \cdot S_{max}}{1 - q} \quad (5.2)$$

Where S_{max} is the customized maximum size, q is the adaptive gradation and d is the length of drilling or caving. Elements whose barycentre is within this elliptic cylinder are collected to be remeshed.

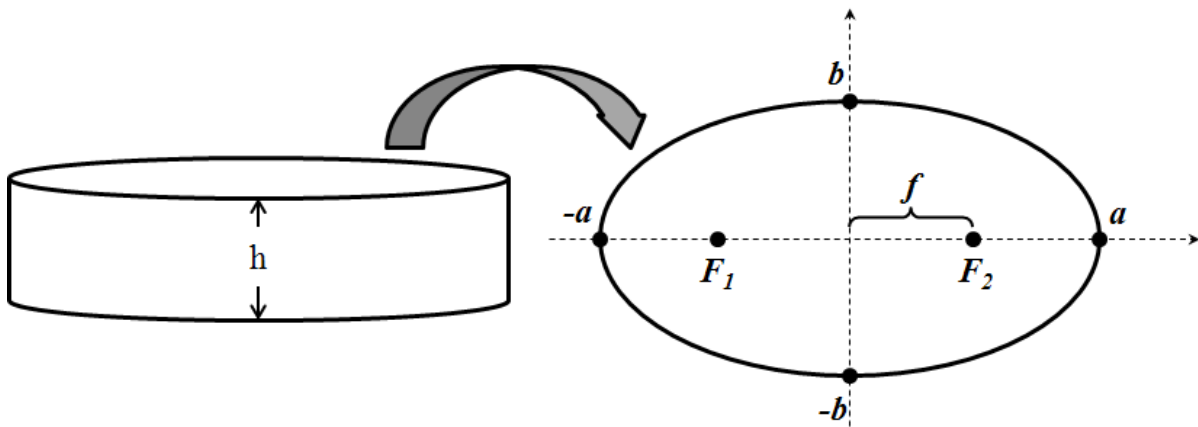


Figure 5.1: An elliptic cylinder for the governing remeshing zone

Moreover, the elliptic cylinder is also utilized to define the local size map H_l . Specifically, we a point P in this zone is mapped onto the base and then its size is calculated by

$$H_l(P) = \frac{(S_{\min} + \frac{|PF_1| + |PF_2|}{2} - f) \cdot (q - 1) + S_{\min}}{q} \quad (5.3)$$

In terms of the definition of size map H_g , we assume that $\{N_i\}$ and $\{T_i\}$ are respectively the sets of nodes and elements within the governing elliptic cylinder. For a node N_i of $\{N_i\}$, its size $H_g(N_i)$ is the average length of its incident edges. For a point P , we firstly locate it in one element T_i of $\{T_i\}$ and then obtain the interpolated value by:

$$H_g(P) = \sum a_j \cdot H_g(N_j), N_j \in T_i \quad (5.4)$$

Where N_j are the nodes in T_i and a_j are the volume coordinates of T_i .

5.2.2 Centroidal Voronoi diagram based on mesh density control

Given an open set $\Omega \subseteq R^N$, and n different generators $\{z_i\}_{i=1}^n$. Let $dis(\cdot)$ denote the distance function on R^N , the Voronoi diagram (whose dual is well-known as Delaunay triangulation) is defined as $\{V_i\}_{i=1}^n$:

$$V_i = \{x \in \Omega \mid dis(x, z_i) < dis(x, z_j) \text{ for } j = 1, \dots, n, j \neq i\} \quad (5.5)$$

Centroidal Voronoi diagram is firstly proposed by Du et al. [29] where the generator z_i is also the mass centroid of its Voronoi cell:

$$z_i = \frac{\int_{V_i} x \cdot \rho(x) dx}{\int_{V_i} \rho(x) dx} \quad (5.6)$$

Where $\rho(x)$ is a density function of V_i .

An approximation of Formula 5.6 adopted here is:

$$z_i = \frac{\sum C_j \cdot |T_j|}{\sum |T_j|} \quad (5.7)$$

Where $\{T_j\}$ are the elements discretising the Voronoi cell (a 2D case is shown in Figure 5.2) and C_j is the barycentre of T_j . $|T_j|$ is the area/volume of T_j , which is calculated by Heron-type formula. Specifically, the length of an edge ab of T_j is calculated by:

$$l(a,b) = \frac{2|a-b|}{H(a)+H(b)} \quad (5.8)$$

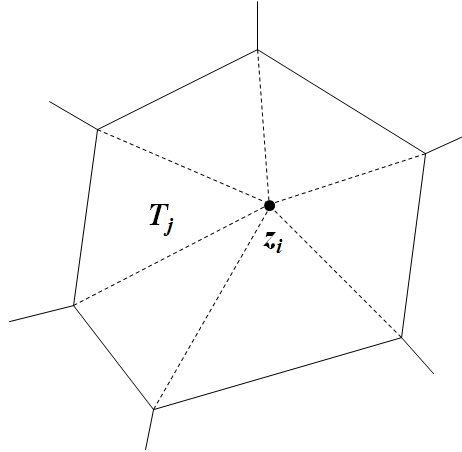


Figure 5.2: A Voronoi cell in 2D domain

5.3 2D remeshing with confirmed stratum interface

Stratum interfaces in 2D domain are represented by constraint lines. In this chapter, the 2D remeshing process consists of the following two major steps: (1) node reposition and (2) edge removal.

5.3.1 Node reposition

We consider a triangular mesh patch MP_{old} (Figure 5.3 (a)), where red lines are constraint lines $\{CL\}$ representing stratum interfaces. Based on the size map H , an isotropic surface remeshing [28] is firstly employed to generate a new mesh MP_{new} (Figure 5.3 (b)) within the domain defined by MP_{old} . In this model, a long wall mining process is undertaken and the remeshing result is demonstrated in Figure 5.3 (b). Obviously, mesh in Figure 5.3 (b) is not consistent with stratum interface constraints. Hence, the following algorithms are involved to recovery these constraints.

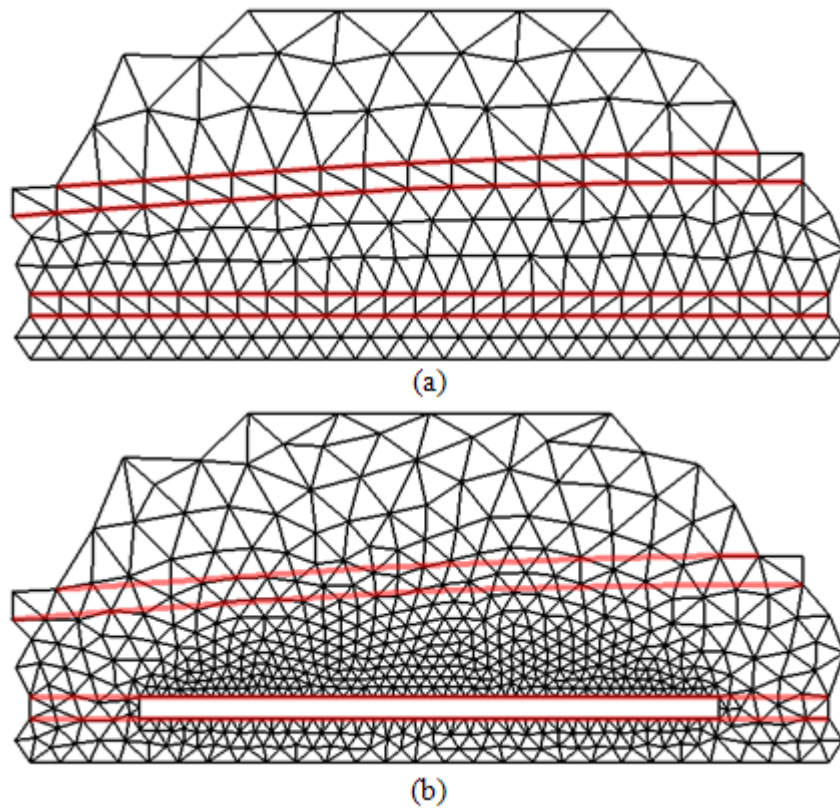


Figure 5.3: remeshing for a patch of geological mesh model: (a) is an old mesh to be remeshed; (b) is an isotropic remeshing result based on the proposed size map H .

To represent $\{CL\}$ in MP_{new} , there must be a set of nodes on the constraints. Therefore, a reposition algorithm is proposed here to adjust nodes around $\{CL\}$. Specifically, the algorithm is implemented as below:

Algorithm 5.1: Node reposition

STEP 1: Assign each node n_i in MP_{new} an array NP_i

STEP 2: Detect candidate points

FOR EACH edge e_i in MP_{new}

The ends of e_i are node n_i and n_j

IF e_i is intersected with $\{CL\}$ on a point P THEN

IF P is closer to n_i THEN

Push P into NP_i

ELSE

Push P into NP_j

ENDIF

END IF

END FOR

STEP 3: Reposition

FOR EACH node n_i in MP_{new}

IF NP_i is empty; THEN CONTINUE; END IF

Choose a point closest to n_i in NP_i to update n_i

END FOR

It is necessary to reposition nodes based on the closet intersection points. As $\{CL\}$ are curves, the operation of arbitrarily repositioning a node to an intersection point may lead to a long distance moving, which will be blocked by mesh topological structures.

To further improve element quality, a mesh optimization method based on Formula 5.7 is performed after Algorithm 5.1. As Formula 5.7 will offset nodes from $\{CL\}$, an amending step is mapping the calculated position onto $\{CL\}$. Consequently, $\{CL\}$ could still be described by a set of nodes in MP_{new} . Algorithm 5.1 and the mesh optimization method are iteratively invoked to guarantee a high quality mesh with stratum interface constraints. It is worthwhile to note that the mesh topological structure needs to be updated during the node reposition to satisfy the Delaunay triangulation criterion [75].

5.3.2 Edge removal

Due to the property of Delaunay triangulation, nodes close to each other are automatically connected in the generated triangular mesh. Consequently, most of the nodes on $\{CL\}$ are linked with its neighbours to make up the stratum interfaces. However, there is still no theoretical guarantee that the stratum interfaces are fully recovered. The recovery of stratum interfaces is achieved by remove edges intersected with $\{CL\}$. We collect the intersected edges and randomly flip them. Based on the theory in [183], these edges will be finally removed by flipping operations and then the stratum interfaces are recovered.

Figure 5.4 is the result of the proposed node reposition and edge removal algorithms. Obviously, compared with Figure 5.3 (b) the stratum interfaces are well represented in the mesh.

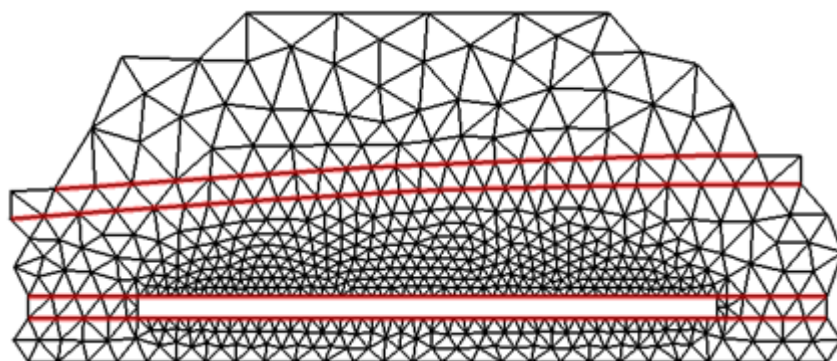


Figure 5.4: A remeshed model conforming to stratum interfaces

5.4 3D remeshing with confirmed stratum interface

The above 2D remeshing technique cannot be extended to the 3D case. It is because the node reposition in 3D is more difficult than that in 2D concerning the correctness of mesh topological structure. In our 3D remeshing algorithm, a set of nodes and facets are generated and inserted into the volumetric model according to 3D stratum interfaces as well as human intervention in geo-engineering. Combining these facets with the surface of remeshing zone as constraints, a long-edge-breaking operation is developed to generate a tetrahedral mesh and then fit it into the global model.

5.4.1 Stratum interface remeshing

In geo-engineering such as the drilling and caving, cross-sections of the working faces are usually regular geometries and convex, which can be automatically recovered in the Delaunay triangulation.

In terms of well drilling, a well will pass through stratum interfaces and cut a hole on the corresponding surfaces and rock mass. Figure 5.5 is a case of well drilling, where the bore hole is a circle. We choose the points on the circle to be inserted in the corresponding surface remeshing. As a result, the boundaries are recovered after the adaptive remeshing.

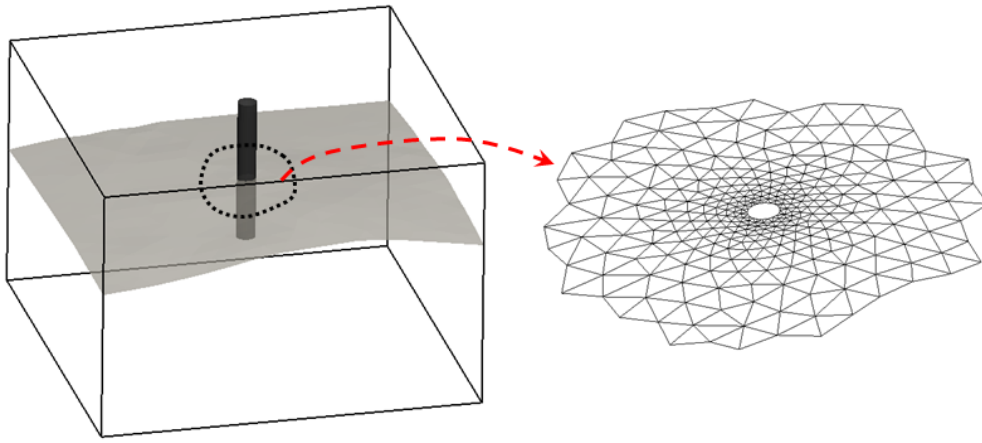


Figure 5.5: A well pass through a stratum interface

In terms of the long wall mining, the working face will parallel to a coal seam. Therefore, the mode of the modification of stratum interfaces is different from the one of drilling. As seen in Figure 5.6, the stratum interface is eroded from its boundary rather than centre. However, the caved zone is still convex, which can be easily recovered in the corresponding surface remeshing. The remeshing result is demonstrated in Figure 5.6.

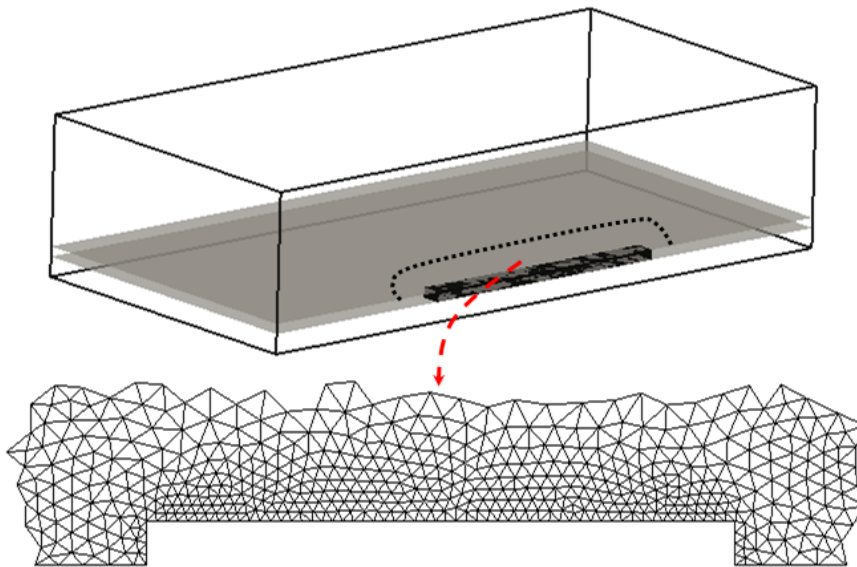


Figure 5.6: A long wall mining example

5.4.2 Volumetric mesh generation

Let VM_{old} of R^3 be the local mesh detected by an elliptic cylinder defined by Formula 5.2, which is going to be remeshed according to the size map H defined by Formula 5.1. We suppose the corresponding new mesh is VM_{new} . Nodes in the new mesh VM_{new} consist of two parts: (1) nodes $N_{constraint}$ on constraints including mesh boundaries and stratum interfaces and (2) nodes N_{in} within

VM_{new} . Since $N_{constraint}$ is known, the amount of interior nodes can be calculated through an assessment of the node quantity in VM_{new} .

We consider a domain Ω of R^3 filled with V cubes with the same edge length. As shown in Figure 5.7, a cube can be divided into five tetrahedra and thereby the number of tetrahedral elements is $NE=5V$. Regarding the number of nodes in Ω , it is approximately $NN \approx V$, since a cube has 8 nodes and most of nodes are shared by 8 cubes. Therefore, the relationship between NE and NN is defined as $NN = 0.2aNE$, where a is a relaxation factor. In this paper, $a=0.94$ is adopted.

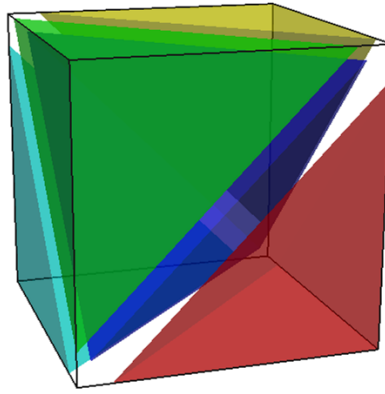


Figure 5.7: A cube consists of five tetrahedra

Let $\{T_i\}$ be the set of tetrahedral elements within the remeshing zone. The size map is defined by the Formula 5.1 and the number of tetrahedral elements in the new mesh is calculated by $NE = 6\sqrt{2} \sum |T_i|$. Hence, the number of nodes within VM_{new} is

$$N_{in} = 1.2\sqrt{2}a \sum |T_i| - N_{constraint} \quad (5.9)$$

Where $|T_j|$ is the volume of T_i , which is calculated by Heron-type formula based on Formula 5.8.

The generation of VM_{new} is achieved by the following algorithm.

Algorithm 5.2: Mesh generation by breaking long-edges

STEP 1: Generate a constrained Delaunay triangulation based on the VM_{old} boundaries and stratum interfaces;

STEP 2: Insert interior nodes

WHILE N_{in} is greater than 0

Collect edges $\{EL_i\}$ whose lengths are greater than 1.0 concerning Formula 5.8 and then sort them in a decreasing order.

FOR EACH edge EL_i

IF EL_i does not exist THEN

CONTINUE

ELSE

Insert a node at the middle of EL_i and decrease N_{in} by 1

END IF

END FOR

END WHILE

STEP 3: Optimize the element quality by Formula 5.7

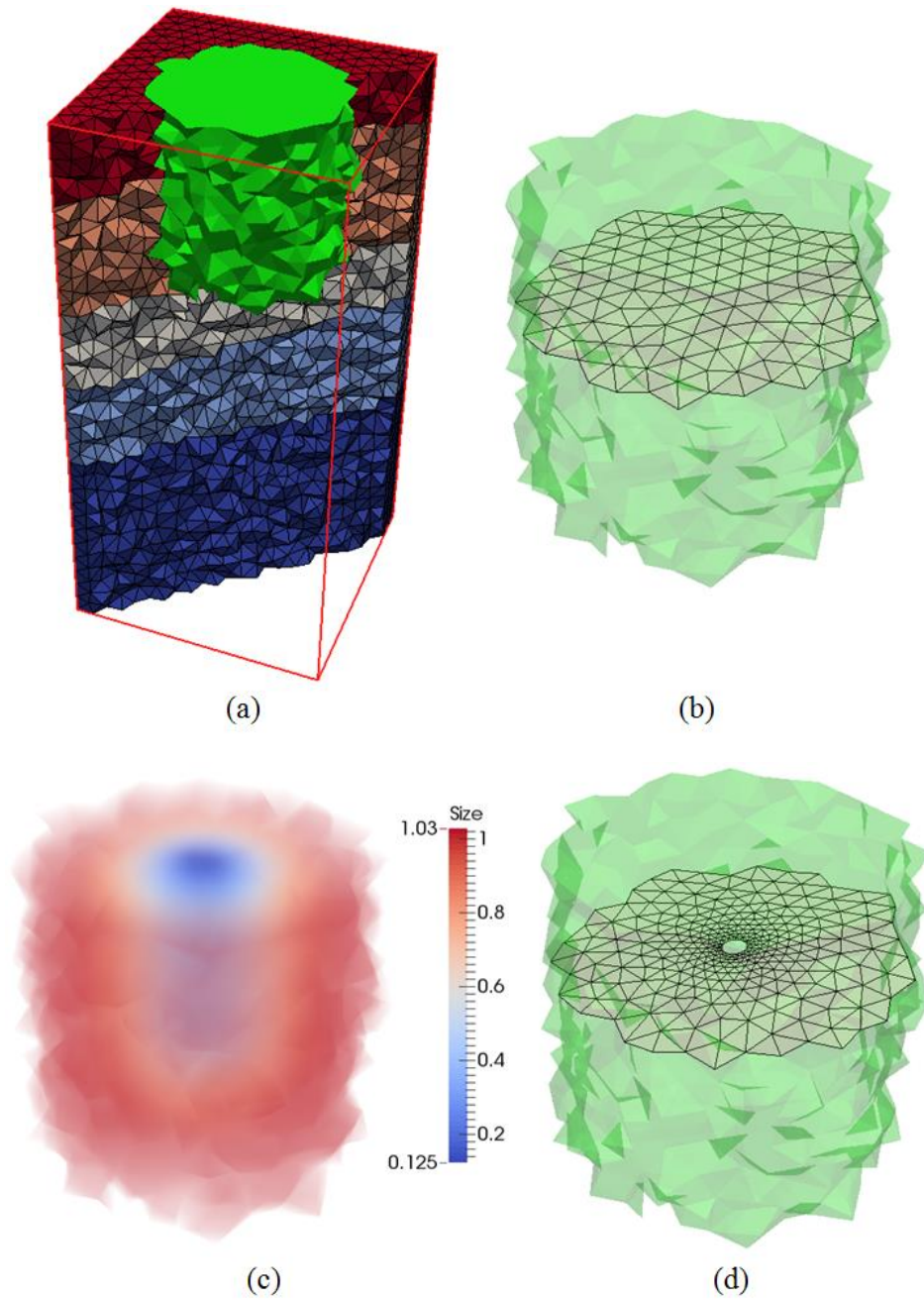
5.5 Numerical applications

We use two application examples to demonstrate the capability of the proposed adaptive remeshing technique for geological structures. The first one is a vertical well drilling process. As a well will vertically drill through stratum interfaces, the process only involves 3D remeshing with confirmed stratum interfaces. The second example is for a horizontal long wall caving. Therefore, both 2D and 3D interface preservations are utilized to maintain the integrity of stratum interfaces in the corresponding adaptive remeshing process.

5.5.1 Remeshing for a vertical well drilling

Firstly, one step of a well drilling is described to demonstrate the remeshing process in detail. As shown in Figure 5.8 (a), the existing mesh model have an average element size of 1.0 and there are five strata indicated by different colours. We adopt a well with a circular bore hole and thus the corresponding remeshing zone is approximately a cylinder. The parameters for the detection of remeshing zone are defined as $S_{min}=0.125$ the element size on the well, $S_{max}=1.0$ the average element size in the model and $q=1.5$ the gradation. The mesh highlighted by light green in Figure 5.8 (a) is the remeshing zone. Figure 5.8 (b) is the interface between the first and second stratum from the top of the model, which is required to be preserved in the remeshing process. Based on Formula 5.1, a size map in Figure 5.8 (c) is generated to control element sizes as well as adaptive features in the remeshed model. In Figure 5.8 (d), the stratum interface is remeshed and a hole is created in the area where the well passes through. Figure 5.8 (e) is the remeshed result for the remeshing domain. Obviously, the geometry of the stratum is maintained. Moreover, the element size distribution obeys the size map in Figure 5.8 (c), which increases from bore hole to the model

boundary. Finally, the new generated mesh in Figure 5.8 (e) is integrated into the original model to complete this drilling step.



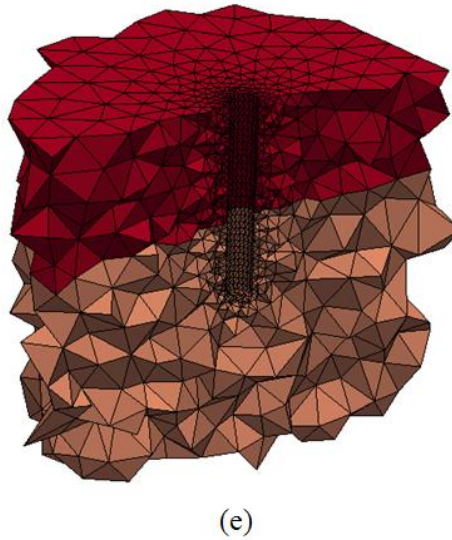


Figure 5.8: one step of a well drilling process: (a) the well and remeshing zone, (b) stratum interface within the remeshing zone, (c) the size map, (d) the stratum interface after remeshing and (e) the volumetric mesh after remeshing.

In Figure 5.9, the whole process of a well drilling is demonstrated. The size of the mesh model in Figure 5.9 (a) is $16 \times 16 \times 35 \text{m}^3$ and a well with a diameter of 0.8m will be created in the model. Figure 5.9 (b) is the stratum interfaces which need preservation in the remeshing for drilling. We adopt the minimum dihedral angle [174] as the element quality measurement and attach a chart with every volumetric meshes. From top to bottom, the drilling work is achieved by the proposed adaptive remeshing algorithm. As demonstrated in Figure 5.9 (c)-(f), the remeshing algorithm maintains all the stratum interfaces when the bore hole passes through them. Besides, the element size of the mesh is adapted from the bore hole to the model boundary. Additionally, the high element quality is kept in each step of drilling as required by geocomputing applications.

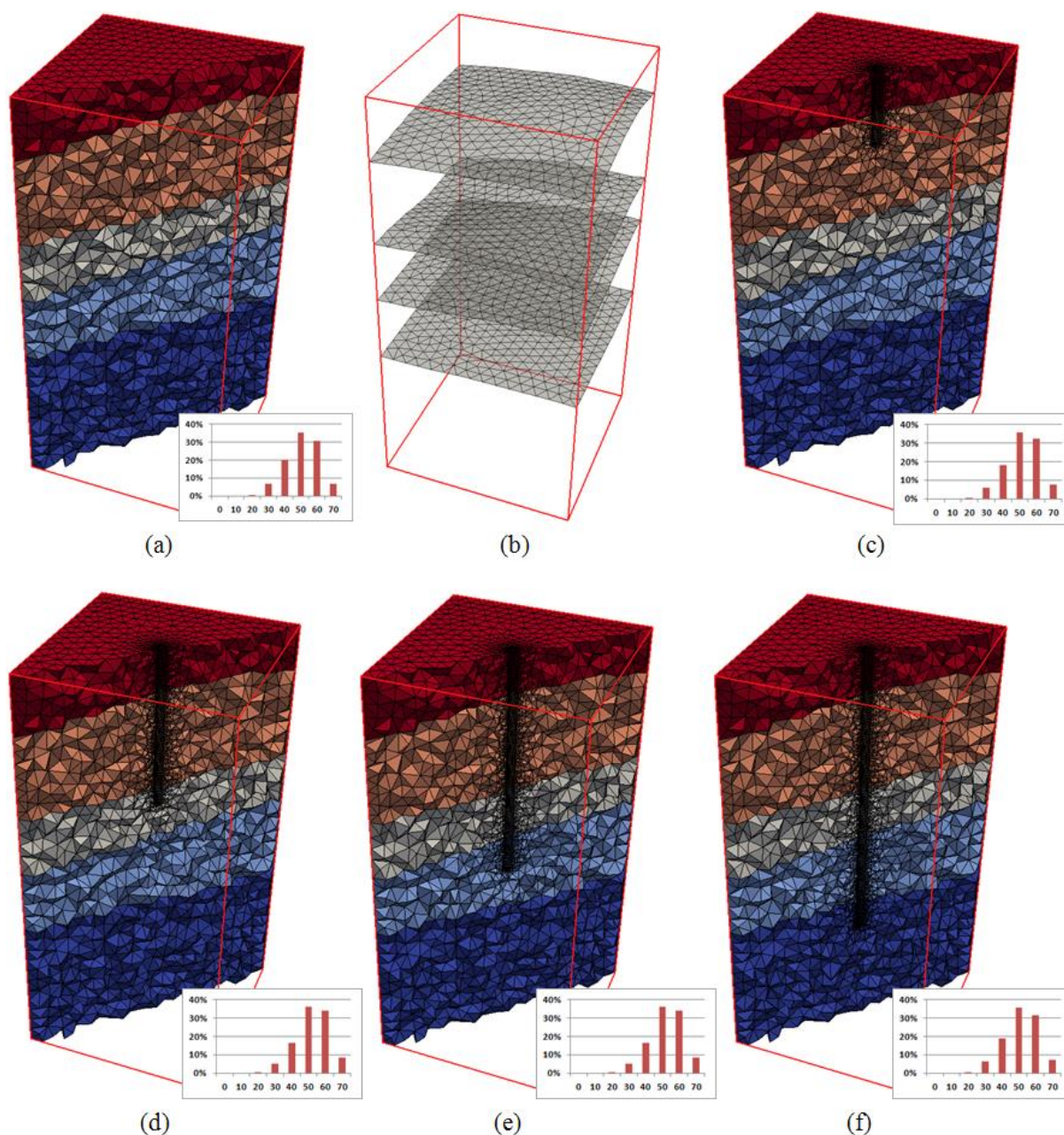


Figure 5.9: A well drilling process: (a) the well model, (b) the stratum interfaces and (c)-(f) the well drilling steps. The charts are element quality measured by the minimum dihedral angle in tetrahedral elements.

5.5.2 Remeshing for a horizontal long wall caving

Compared with the above well drilling process, the remeshing for a long wall caving is more complicated. As a long wall caving horizontally amends the structure of a stratum, the corresponding remeshing requires stratum interface preservation techniques in both 2D and 3D. Figure 5.11 (a) is the volumetric mesh model whose size is $200 \times 100 \times 48 \text{m}^3$. There are five strata as well as four interfaces. Figure 5.10 (a) is one side of the mesh model. The caving process is

undertaken in the second stratum from the bottom. The size of working face is $80 \times 3 \text{ m}^2$. The parameters of remeshing used here are $S_{min}=1.3$, $S_{max}=8.0$ and $q=1.5$. In terms of the 2D adaptive remeshing, the result is shown in Figure 5.10 (b). The geometries of the stratum interfaces in the new mesh are the same as that of old mesh. Besides, the element sizes in the mesh follow the defined size map based on Formula 5.1.

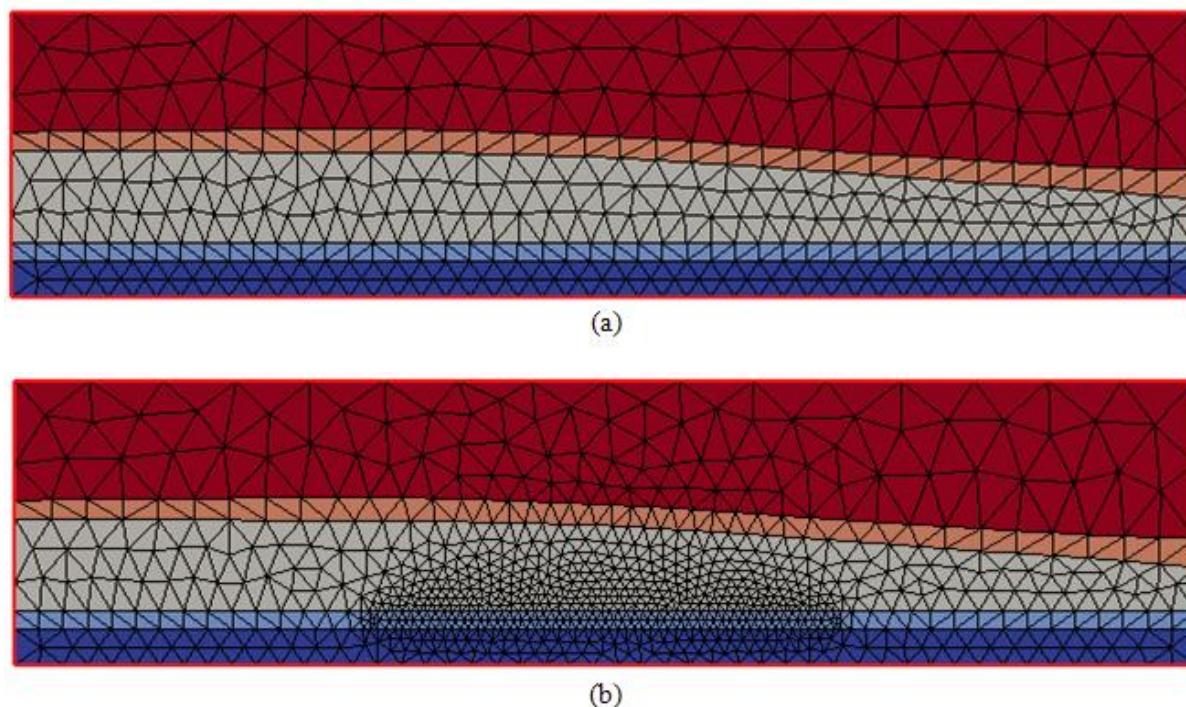


Figure 5.10: 2D adaptive remeshing conforming to stratum interfaces: (a) is the old mesh model and (b) is the remeshed result.

Mesheres in Figure 5.11 shows the complete process of a long wall caving by the proposed remeshing algorithm. Similar as the well drilling case, every step of the caving comes with a chart of element quality measured by the minimum dihedral angle [174]. Figure 5.11 (b) shows a half of the original mesh model, where the node quantity is just 8,083. Based on the customized shape of working face and length of caving step, the model is automatically remeshed from Figure 5.11 (c) to (f), where the caving process keep the same speed. Finally, the node quantity increases to 35,921 in Figure 5.11 (f). Although the stratum interfaces consist of different facets in each caving step, their geometrical features are preserved. Moreover, the proposed remeshing algorithm guarantee a generation of high-quality elements in each of these caving steps.

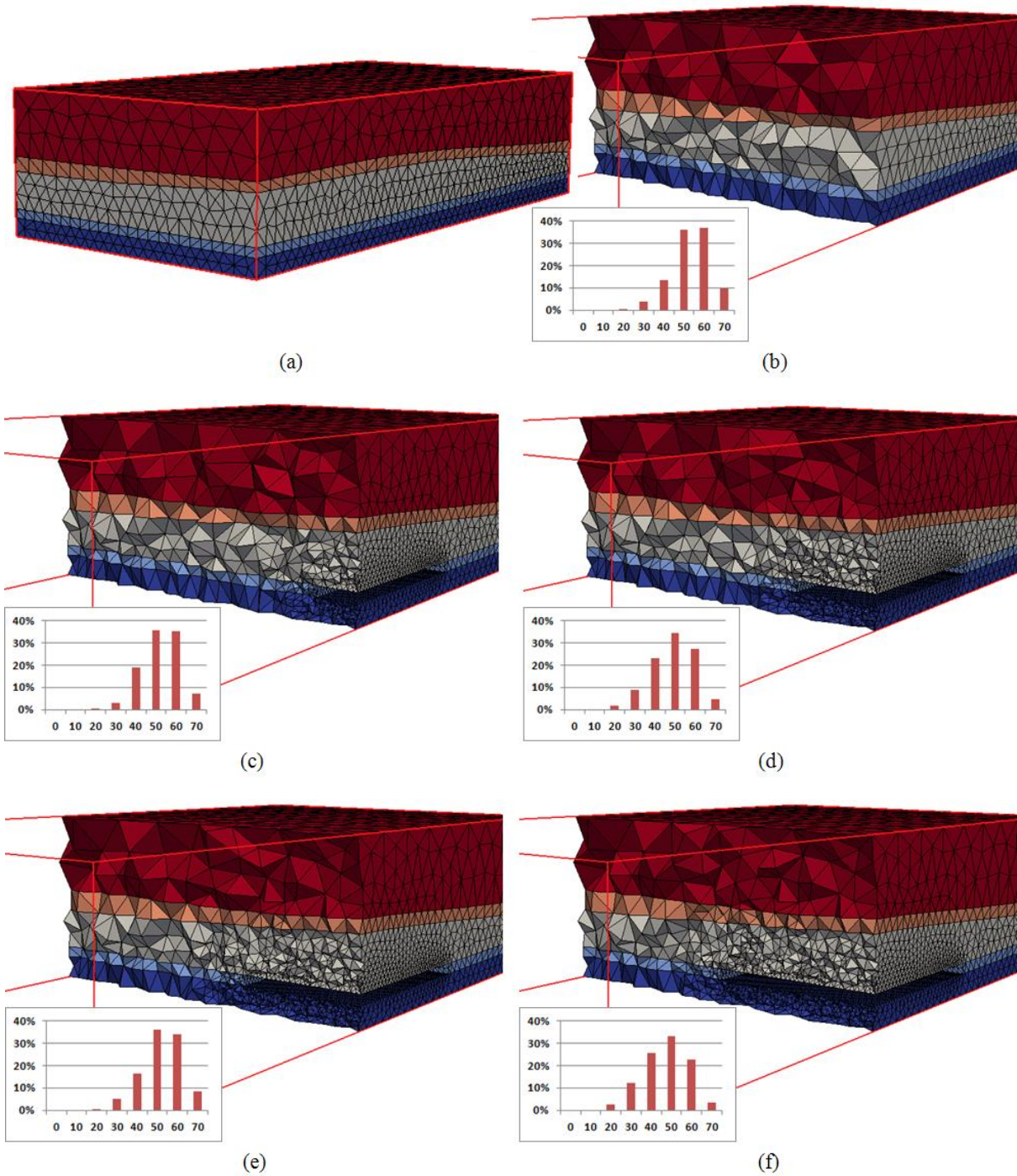


Figure 5.11: 3D adaptive remeshing conforming to stratum interfaces: (a) is the original mesh model and (b) is a half of it. (c)-(f) are the caving steps driven by the proposed remeshing method, where the charts are element quality measured by the minimum dihedral angle in tetrahedral elements.

5.6 Conclusions

In this paper, an adaptive remeshing approach is proposed for geological structure with stratum interface constraints. The numerical examples of remeshing for both drilling and caving processes

have validated the proposed algorithm and proven its usefulness. Therefore, the following conclusions are drawn:

- (1) Both 2D and 3D conforming strategies are effective to preserve stratum interfaces in terms of the geometry.
- (2) The proposed definition of the mesh size map is appropriate for adapting element size from working areas to model boundary as demonstrated in the above drilling and caving processes.
- (3) The proposed volumetric mesh generation method can effectively create high-quality elements with a gradation consistent with the corresponding size map for further geological engineering analysis

Chapter 6 Conclusions and Future Work

This thesis proposed new automatic mesh generation algorithms and an adaptive remeshing method to provide a link between geological data and numerical analysis. Strategies in both 2D and 3D are carried out to generate high-quality meshes for representation of geo-objects, which take into account fractures and material interface constraints. In this chapter, the conclusions of this thesis are summarized and the future work based on current outcomes is discussed.

6.1 Conclusions

Based on the research work carried out in this PhD project, the following conclusions are drawn:

(1). An arbitrary boundary constrained quadrilateral mesh generation method has been developed to produce high-quality mesh models for 2D multi-material geological structure. The proposed meshing approach significantly improves the element quality and creates layers of well-aligned elements around complex image boundaries. Compared with algorithms developed by Park et al. [168] and Lee et al. [43], the method has more advantages in generating high-quality elements and reducing irregular nodes. The effectiveness of the method has been validated using examples from practice such as images of coal plugs and fractured rocks.

(2). An effective 3D meshing algorithm has been proposed and implemented towards generating mesh representations for fractured rocks. When compared with 3D digital images of fractured rocks, the meshes generated by the proposed algorithm can represent fractured rocks through smaller data sets and reasonable shape similarities. The application example showed that the ratio between the tetrahedral mesh element number and the digital image grid number is 1:6704 and the corresponding shape similarity is 60.3%. Based on our numerical experiments, the optimal Voronoi cell radius used for generating surface mesh for the rock sample is 7 and surface meshes with shape similarity above 60% are considered as close approximations for fractured rocks. In terms of effectiveness, it was proved that if the proposed umbrella operations are successfully implemented to all surface nodes, the generated surface mesh is valid with regard to preserving mesh topology structure and representing geometry features of fracture. A junction weight threshold is introduced

to reduce the number of failed umbrella operations and its appropriate range is from 10 to 12. Even if the umbrella operation fails, the manual repair work is limited only to the vicinity of failed nodes and easy to achieve.

(3). A mesh generation method for 3D geological reservoirs with arbitrary stratigraphic surface constraints is proposed, which has been successfully applied to generate mesh for the Lawn Hill in Queensland, Australia. The proposed geodesic-based surface remeshing approach is effective in generating aligned elements parallel to surface junction lines. The front merge technique together with detection zone generation can robustly generate elements on a stratigraphic surface with complicated geometries. Compared with the Lawn Hill model in voxel format, the data set is reduced from 7.1×10^7 voxels to a volume mesh with only 1.7×10^5 nodes. Besides, the element quality of the generated mesh is high concerning four different measurements [173, 174], which is suitable for FEM-based applications.

(4). An adaptive remeshing approach conforming to stratum interfaces has been developed for geological structures towards simulation of geo-engineering processes by the finite element method. Both 2D and 3D stratum preservation algorithms are proposed and implemented to carry out a complete solution for remeshing with the consistency of interfaces. The proposed definition of the element size map is appropriate for adapting element size from working areas to model boundary. The proposed volumetric mesh generation method can effectively create high-quality elements with a gradation consistent with the corresponding size map. Applications in a well drilling and a long wall caving model demonstrate the potential capability of the proposed remeshing approach in both the petroleum and coal mining industry.

6.2 Future work

The majority of the work completed in this study focuses on generating static mesh models for geo-objects. One of the most important objectives of our future work is extending the developed algorithms to resolve dynamic problems for geological modelling. In addition hexahedral mesh generation for geological modelling is highly sought after due to its capacity for increased numerical accuracy. Besides, parallelization of the current SCVD construction is important to increase the speed of the proposed meshing algorithms for 3D images. Hence, the future research areas include:

- (1) Extending the proposed mesh generation for fractured rocks in Chapter 3 to further describe fracture propagation within the current mesh model promises to be a powerful tool. Challenges such as fracture mesh remeshing, fracture path detection and integration with corresponding numerical methods will need to be addressed.
- (2) A crucial step for the remeshing method proposed in Chapter 5 is the capability to couple the current size map with a stress field for many potential applications in geo-engineering. It is also worthwhile to resolve fractures into well mesh models so that effects such as near-wellbore effects on fracturing can be studied.
- (3) As demonstrated in Chapter 2 and 4, geodesic isolines can generate elements parallel to line constraints. Therefore it is reasonable to consider an extension of the proposed quadrilateral mesh generation method to achieve an automatic hexahedral mesh generation for geo-objects in 3D domain.
- (4) The time efficiency analysis in Chapter 3 reveals that the bottle neck of current mesh generation method is the SCVD construction. Fractures in rocks could be divided into several individual pieces and then utilize our algorithm to generate mesh for these sub-fractures simultaneously. Hence such a divide-and-conquer scheme should be further developed to improve the time efficiency of current image-based meshing method.

References

- [1] H.L. Xing, W. Yu, J. Zhang, 3D mesh generation in geocomputing, in: *Advances in Geocomputing*, Springer-Verlag GmbH, 2009, pp. 27-64.
- [2] A.K. Turner, Challenges and trends for geological modelling and visualisation, *Bull Eng Geol Environ*, 65 (2006) 109-127.
- [3] H. Andrä, N. Combaret, J. Dvorkin, E. Glatt, J. Han, M. Kabel, Y. Keehm, F. Krzikalla, M. Lee, C. Madonna, M. Marsh, T. Mukerji, E.H. Saenger, R. Sain, N. Saxena, S. Ricker, A. Wiegmann, X. Zhan, Digital rock physics benchmarks—Part I: Imaging and segmentation, *Computers & Geosciences*, 50 (2013) 25-32.
- [4] H. Andrä, N. Combaret, J. Dvorkin, E. Glatt, J. Han, M. Kabel, Y. Keehm, F. Krzikalla, M. Lee, C. Madonna, M. Marsh, T. Mukerji, E.H. Saenger, R. Sain, N. Saxena, S. Ricker, A. Wiegmann, X. Zhan, Digital rock physics benchmarks—part II: Computing effective properties, *Computers & Geosciences*, 50 (2013) 33-43.
- [5] O.C. Zienkiewicz, R.L. Taylor, *The finite element method*, McGraw-Hill, Burlington, USA, 1967.
- [6] S. Valliappan, Z. Wohua, Numerical modelling of methane gas migration in dry coal seams, *International Journal for Numerical and Analytical Methods in Geomechanics*, 20 (1996) 571-593.
- [7] M.R. Islam, D. Hayashi, A. Kamruzzaman, Finite element modeling of stress distributions and problems for multi-slice longwall mining in Bangladesh, with special reference to the Barapukuria coal mine, *International Journal of Coal Geology*, 78 (2009) 91-109.
- [8] J. Toraño, I. Diego, M. Menéndez, M. Gent, A finite element method (FEM)–Fuzzy logic (Soft Computing)–virtual reality model approach in a coalface longwall mining simulation, *Automation in Construction*, 17 (2008) 413-424.
- [9] W. Zhu, C. Wei, J. Liu, H. Qu, D. Elsworth, A model of coal-gas interaction under variable temperatures, *International Journal of Coal Geology*, 86 (2011) 213–221.
- [10] A. Ghassemi, S. Tarasovs, A.H.D. Cheng, Integral equation solution of heat extraction-induced thermal stress in enhanced geothermal reservoirs, *International Journal for Numerical and Analytical Methods in Geomechanics*, 29 (2005) 829-844.
- [11] X. Zhou, A. Ghassemi, A.H.D. Cheng, A three dimensional integral equation model for calculating poro and thermoelastic stresses induced by cold water injection into a geothermal reservoir, *International Journal for Numerical and Analytical Methods in Geomechanics*, 33 (2009) 1613-1640.
- [12] R. Shukla, P. Ranjith, S. Choi, A. Haque, Study of Caprock Integrity in Geosequestration of Carbon Dioxide, *International Journal of Geomechanics*, 11 (2011) 294.
- [13] H.L. Xing, A. Makinouchi, P. Mora, Finite element modeling of interacting fault systems, *Physics of the Earth and Planetary Interiors*, 163 (2007) 106-121.
- [14] Y.J. Hsu, M. Simons, C. Williams, E. Casarotti, Three dimensional FEM derived elastic Green's functions for the coseismic deformation of the 2005 Mw 8.7 Nias-Simeulue, Sumatra earthquake, *Geochemistry Geophysics Geosystems*, 12 (2011) Q07013.
- [15] R.B. Manasa, K. Murali, S. Sannasiraj, V. Sundar, Simulation and Prediction of Runup Heights Due to Great Indian Ocean Tsunami, *Advances in Water Resources and Hydraulic Engineering*, IV (2009) 1244-1249.
- [16] S.J. Owen, A survey of unstructured mesh generation technology, in: *Proceedings of the 7th International Meshing Roundtable*, Citeseer, 1998, pp. 239-267.
- [17] J.R. Shewchuk, Delaunay refinement algorithms for triangular mesh generation, *Computational Geometry*, 22 (2002) 21-74.

- [18] S.H. Lo, A new mesh generation scheme for arbitrary planar domains, *International Journal for Numerical Methods in Engineering*, 21 (1985) 1403-1426.
- [19] P.L. George, F. Hecht, E. Saltel, Automatic mesh generator with specified boundary, *Computer Methods in Applied Mechanics and Engineering*, 92 (1991) 269-288.
- [20] P. Alliez, G. Ucelli, C. Gotsman, M. Attene, Recent advances in remeshing of surfaces, *Shape Analysis and Structuring*, (2008) 53-82.
- [21] M. Alexa, Merging polyhedral shapes with scattered features, in: *Proceedings of the International Conference on Shape Modeling and Applications(SMI-99)*, IEEE, 1999, pp. 202-210.
- [22] M. Alexa, Recent advances in mesh morphing, *Computer Graphics Forum*, 21 (2002) 173-196.
- [23] C. Gotsman, X. Gu, A. Sheffer, Fundamentals of spherical parameterization for 3D meshes, *Acm Transactions on Graphics*, 22 (2003) 358-363.
- [24] E. Praun, H. Hoppe, Spherical parametrization and remeshing, *ACM Transactions on Graphics*, 22 (2003) 340-349.
- [25] A.W.F. Lee, D. Dobkin, W. Sweldens, P. Schröder, Multiresolution mesh morphing, in: *Proceedings of the 26th Annual Conference on Computer Graphics and Interactive Techniques ACM Press/Addison-Wesley Publishing Co.*, 1999, pp. 343-350.
- [26] J.L. Lin, J.H. Chuang, C.C. Lin, C.C. Chen, Consistent parametrization by quinary subdivision for remeshing and mesh metamorphosis, in: *Proceedings of the 1st International Conference on Computer Graphics and Interactive Techniques in Australasia and South East Asia*, ACM, 2003, pp. 151-158.
- [27] E. Praun, W. Sweldens, P. Schröder, Consistent mesh parameterizations, in: *Proceedings of the 28th Annual Conference on Computer Graphics and Interactive Techniques ACM*, 2001, pp. 179-184.
- [28] P. Alliez, E.C. de Verdiere, O. Devillers, M. Isenburg, Isotropic surface remeshing, in: *Proceedings of Shape Modeling International 2003*, 2003, pp. 49-58.
- [29] Q. Du, V. Faber, M. Gunzburger, Centroidal Voronoi tessellations: applications and algorithms, *SIAM Review*, 41 (1999) 637-676.
- [30] R. Kimmel, J.A. Sethian, Computing geodesic paths on manifolds, in: *Proceedings of the National Academy of Sciences*, 1998, pp. 8431-8435.
- [31] G. Peyre, L.D. Cohen, Geodesic remeshing using front propagation, *International Journal of Computer Vision*, 69 (2006) 145-156.
- [32] G. Peyre, L. Cohen, Surface segmentation using geodesic centroidal tessellation, in: *Proceedings of 3D Data Processing, Visualization and Transmission*, IEEE, 2004, pp. 995-1002.
- [33] O. Sifri, A. Sheffer, C. Gotsman, Geodesic-based surface remeshing, in: *Proceedings of 12th International Meshing Roundtable*, Citeseer, 2003, pp. 189-199.
- [34] T.D. Blacker, M.B. Stephenson, Paving: A new approach to automated quadrilateral mesh generation, *International Journal for Numerical Methods in Engineering*, 32 (1991) 811-847.
- [35] D.R. White, P. Kinney, Redesign of the paving algorithm: Robustness enhancements through element by element meshing, in: *Proceedings of the 6th International Meshing Roundtable*, Citeseer, 1997, pp. 323-335.
- [36] J.M. Hyman, S. Li, P. Knupp, M. Shashkov, An algorithm for aligning a quadrilateral grid with internal boundaries, *Journal of Computational Physics*, 163 (2000) 133-149.
- [37] E. Catmull, J. Clark, Recursively generated B-spline surfaces on arbitrary topological meshes, *Computer-Aided Design*, 10 (1978) 350-355.
- [38] P. Kinney, Cleanup: Improving quadrilateral finite element meshes, in: *Proceedings of the 6th International Meshing Roundtable*, 1997, pp. 437-447.
- [39] B.P. Johnston, J.M. Sullivan Jr, A. Kwasnik, Automatic conversion of triangular finite element meshes to quadrilateral elements, *International Journal for Numerical Methods in Engineering*, 31 (1991) 67-84.
- [40] C. Lee, S. Lo, A new scheme for the generation of a graded quadrilateral mesh, *Computers & Structures*, 52 (1994) 847-857.

- [41] H. Borouchaki, P.J. Frey, Adaptive triangular-quadrilateral mesh generation, *International Journal for Numerical Methods in Engineering*, 41 (1998) 915-934.
- [42] S.J. Owen, M.L. Staten, S.A. Canann, S. Saigal, Q-Morph: an indirect approach to advancing front quad meshing, *International Journal for Numerical Methods in Engineering*, 44 (1999) 1317-1340.
- [43] K.Y. Lee, I.I. Kim, D.Y. Cho, T. Kim, An algorithm for automatic 2D quadrilateral mesh generation with line constraints, *Computer-Aided Design*, 35 (2003) 1055-1068.
- [44] M. Lai, S. Benzley, D. White, Automated hexahedral mesh generation by generalized multiple source to multiple target sweeping, *International Journal for Numerical Methods in Engineering*, 49 (2000) 261-275.
- [45] L. Mingwu, S.E. Benzley, G. Sjaardema, T. Tautges, A multiple source and target sweeping method for generating all-hexahedral finite element meshes, in: *Proceedings of the 5th International Meshing Roundtable*, 1996, pp. 217-225.
- [46] N. Chiba, I. Nishigaki, Y. Yamashita, C. Takizawa, K. Fujishiro, A flexible automatic hexahedral mesh generation by boundary-fit method, *Computer Methods in Applied Mechanics and Engineering*, 161 (1998) 145-154.
- [47] M. Li, R. Tong, All-hexahedral mesh generation via inside-out advancing front based on harmonic fields, *Vis Comput*, 28 (2012) 839-847.
- [48] M. Nieser, U. Reitebuch, K. Polthier, CubeCover—Parameterization of 3D Volumes, *Computer Graphics Forum*, 30 (2011) 1397-1406.
- [49] M.L. Staten, R.A. Kerr, S.J. Owen, T.D. Blacker, Unconstrained Paving and Plastering: Progress Update, in: *Proceedings of the 15th International Meshing Roundtable*, Springer Berlin Heidelberg, 2006, pp. 469-486.
- [50] M.L. Staten, S.J. Owen, T.D. Blacker, Unconstrained Paving & Plastering: A New Idea for All Hexahedral Mesh Generation, in: *Proceedings of the 14th International Meshing Roundtable*, Springer Berlin Heidelberg, 2005, pp. 399-416.
- [51] M.L. Staten, R.A. Kerr, S.J. Owen, T.D. Blacker, M. Stupazzini, K. Shimada, Unconstrained plastering—Hexahedral mesh generation via advancing-front geometry decomposition, *International Journal for Numerical Methods in Engineering*, 81 (2010) 135-171.
- [52] T.J. Tautges, T. Blacker, S.A. Mitchell, The whisker weaving algorithm: A connectivity-based method for constructing all-hexahedral finite element meshes, *International Journal for Numerical Methods in Engineering*, 39 (1996) 3327-3349.
- [53] N.T. Folwell, S.A. Mitchell, Reliable Whisker Weaving via Curve Contraction, *Engineering with Computers*, 15 (1999) 292-302.
- [54] Y. Kawamura, M.S. Islam, Y. Sumi, A strategy of automatic hexahedral mesh generation by using an improved whisker-weaving method with a surface mesh modification procedure, *Engineering with Computers*, 24 (2008) 215-229.
- [55] Y. Zhang, C. Bajaj, Adaptive and quality quadrilateral/hexahedral meshing from volumetric data, *Computer Methods in Applied Mechanics and Engineering*, 195 (2006) 942-960.
- [56] L. Maréchal, Advances in Octree-Based All-Hexahedral Mesh Generation: Handling Sharp Features, in: *Proceedings of the 18th International Meshing Roundtable*, Springer Berlin Heidelberg, 2009, pp. 65-84.
- [57] Y. Ito, A.M. Shih, B.K. Soni, Octree-based reasonable-quality hexahedral mesh generation using a new set of refinement templates, *International Journal for Numerical Methods in Engineering*, 77 (2009) 1809-1833.
- [58] Y. Zhang, X. Liang, G. Xu, A robust 2-refinement algorithm in octree or rhombic dodecahedral tree based all-hexahedral mesh generation, *Computer Methods in Applied Mechanics and Engineering*, 256 (2013) 88-100.
- [59] J. Qian, Y. Zhang, Automatic unstructured all-hexahedral mesh generation from B-Reps for non-manifold CAD assemblies, *Engineering with Computers*, 28 (2012) 345-359.
- [60] J. Qian, Y. Zhang, W. Wang, A.C. Lewis, M.A.S. Qidwai, A.B. Geltmacher, Quality improvement of non-manifold hexahedral meshes for critical feature determination of

- microstructure materials, *International Journal for Numerical Methods in Engineering*, 82 (2010) 1406-1423.
- [61] M.A. Yerry, M.S. Shephard, Automatic three dimensional mesh generation by the modified octree technique, *International Journal for Numerical Methods in Engineering*, 20 (1984) 1965-1990.
- [62] M.S. Shephard, M.K. Georges, Automatic three-dimensional mesh generation by the finite octree technique, *International Journal for Numerical Methods in Engineering*, 32 (1991) 709-749.
- [63] V. Parthasarathy, S. Kodiyalam, A constrained optimization approach to finite element mesh smoothing, *Finite Elements in Analysis and Design*, 9 (1991) 309-320.
- [64] L.A. Freitag, On combining Laplacian and optimization-based mesh smoothing techniques, in: S.S. Canann S (Ed.) *Trends in Unstructured Mesh Generation*, AMD, New York, 1997, pp. 37-44.
- [65] D. Vartziotis, T. Athanasiadis, I. Goudas, J. Wipper, Mesh smoothing using the geometric element transformation method, *Computer Methods in Applied Mechanics and Engineering*, 197 (2008) 3760-3767.
- [66] Y. Zhang, C. Bajaj, B.-S. Sohn, 3D finite element meshing from imaging data, *Computer Methods in Applied Mechanics and Engineering*, 194 (2005) 5083-5106.
- [67] X. Liang, Y. Zhang, An octree-based dual contouring method for triangular and tetrahedral mesh generation with guaranteed angle range, *Engineering with Computers*, 30 (2014) 211-222.
- [68] Y. Zhang, G. Xu, C. Bajaj, Quality meshing of implicit solvation models of biomolecular structures, *Computer Aided Geometric Design*, 23 (2006) 510-530.
- [69] B. Delaunay, Sur la sphere vide, *Bulletin of Academy of Sciences of the USSR*, 6 (1934) 793-800.
- [70] A. Bowyer, Computing dirichlet tessellations, *The Computer Journal*, 24 (1981) 162-166.
- [71] D.F. Watson, Computing the n-dimensional Delaunay tessellation with application to Voronoi polytopes, *The Computer Journal*, 24 (1981) 167-172.
- [72] N.P. Weatherill, O. Hassan, Efficient three dimensional Delaunay triangulation with automatic point creation and imposed boundary constraints, *International Journal for Numerical Methods in Engineering*, 37 (1994) 2005-2039.
- [73] Q. Du, D. Wang, Constrained boundary recovery for three dimensional Delaunay triangulations, *International Journal for Numerical Methods in Engineering*, 61 (2004) 1471-1500.
- [74] P.L. George, H. Borouchaki, E. Saltel, 'Ultimate' robustness in meshing an arbitrary polyhedron, *International Journal for Numerical Methods in Engineering*, 58 (2003) 1061-1089.
- [75] J.R. Shewchuk, Delaunay refinement mesh generation. Carnegie Mellon University, 1997.
- [76] H. Si, Adaptive tetrahedral mesh generation by constrained Delaunay refinement, *International Journal for Numerical Methods in Engineering*, 75 (2008) 856-880.
- [77] R. Löhner, P. Parikh, Generation of three-dimensional unstructured grids by the advancing-front method, *International Journal for Numerical Methods in Fluids*, 8 (1988) 1135-1149.
- [78] R. Löhner, Progress in grid generation via the advancing front technique, *Engineering with Computers*, 12 (1996) 186-210.
- [79] S.H. Lo, Volume discretization into tetrahedra--I. Verification and orientation of boundary surfaces, *Computers & Structures*, 39 (1991) 493-500.
- [80] S.H. Lo, Volume discretization into tetrahedra--II. 3D triangulation by advancing front approach, *Computers & Structures*, 39 (1991) 501-511.
- [81] J. Ruppert, R. Seidel, On the difficulty of triangulating three-dimensional nonconvex polyhedra, *Discrete & Computational Geometry*, 7 (1992) 227-253.
- [82] P.L. George, E. Seveno, The advancing-front mesh generation method revisited, *International Journal for Numerical Methods in Engineering*, 37 (1994) 3605-3619.
- [83] J. Schöberl, NETGEN An advancing front 2D/3D-mesh generator based on abstract rules, *Computing and Visualization in Science*, 1 (1997) 41-52.
- [84] P.J. Frey, H. Borouchaki, P.L. George, 3D Delaunay mesh generation coupled with an advancing-front approach, *Computer Methods in Applied Mechanics and Engineering*, 157 (1998) 115-131.

- [85] M. Nixon, A. Aguado, Feature Extraction & Image Processing, Second Edition, Academic Press, 2008.
- [86] T. Ahonen, A. Hadid, M. Pietikainen, Face Description with Local Binary Patterns: Application to Face Recognition, IEEE Transactions on Pattern Analysis and Machine Intelligence, 28 (2006) 2037-2041.
- [87] S. Ribaric, I. Fratric, A biometric identification system based on eigenpalm and eigenfinger features, IEEE Transactions on Pattern Analysis and Machine Intelligence, 27 (2005) 1698-1709.
- [88] D. Liu, H. Gang, P. Viola, C. Tsuhan, Integrated feature selection and higher-order spatial feature extraction for object categorization, in: IEEE Conference on Computer Vision and Pattern Recognition, 2008, pp. 1-8.
- [89] F. Remondino, S. El-Hakim, Image-based 3D Modelling: A Review, The Photogrammetric Record, 21 (2006) 269-291.
- [90] Z. Yefeng, A. Barbu, B. Georgescu, M. Scheuering, D. Comaniciu, Fast Automatic Heart Chamber Segmentation from 3D CT Data Using Marginal Space Learning and Steerable Features, in: IEEE 11th International Conference on Computer Vision, 2007, pp. 1-8.
- [91] D. Lesage, E.D. Angelini, I. Bloch, G. Funka-Lea, A review of 3D vessel lumen segmentation techniques: Models, features and extraction schemes, Medical Image Analysis, 13 (2009) 819-845.
- [92] P. Aljabar, R.A. Heckemann, A. Hammers, J.V. Hajnal, D. Rueckert, Multi-atlas based segmentation of brain images: Atlas selection and its effect on accuracy, NeuroImage, 46 (2009) 726-738.
- [93] C.O. Karacan, E. Okandan, Adsorption and gas transport in coal microstructure: investigation and evaluation by quantitative X-ray CT imaging, Fuel, 80 (2001) 509-520.
- [94] S. Peth, R. Horn, F. Beckmann, T. Donath, J. Fischer, A.J.M. Smucker, Three-Dimensional Quantification of Intra-Aggregate Pore-Space Features using Synchrotron-Radiation-Based Microtomography Soil Sci. Soc. Am. J., (2008) 897-907.
- [95] A.S. Al-Kharusi, M.J. Blunt, Network extraction from sandstone and carbonate pore space images, Journal of Petroleum Science and Engineering, 56 (2007) 219-231.
- [96] J.C. Close, M.J. Mavor, Influence of Coal Composition and Rank on Fracture Development in Fruitland Coal Gas Reservoirs of the San Juan Basin, in: S. Schwochow, Murray, D.K., Fahy, M.F. (Ed.) Coalbed Methane of Western North America., 1991, pp. 109-121.
- [97] J. Liu, J. Sheng, A. Polak, D. Elsworth, H. Yasuhara, A. Grader, A fully-coupled hydrological-mechanical-chemical model for fracture sealing and preferential opening, International Journal of Rock Mechanics and Mining Sciences, 43 (2006) 23-36.
- [98] J.P. Mathews, J.D.N. Pone, G.D. Mitchell, P. Halleck, High-resolution X-ray computed tomography observations of the thermal drying of lump-sized subbituminous coal, Fuel Processing Technology, 92 (2011) 58-64.
- [99] Y. Zhang, T.J.R. Hughes, C.L. Bajaj, An automatic 3D mesh generation method for domains with multiple materials, Computer Methods in Applied Mechanics and Engineering, 199 (2010) 405-415.
- [100] D. Wildenschild, A.P. Sheppard, X-ray imaging and analysis techniques for quantifying pore-scale structure and processes in subsurface porous medium systems, Advances in Water Resources, 51 (2013) 217-246.
- [101] V. Cnudde, B. Masschaele, M. Dierick, J. Vlassenbroeck, L.V. Hoorebeke, P. Jacobs, Recent progress in X-ray CT as a geosciences tool, Applied Geochemistry, 21 (2006) 826-832.
- [102] P. Iassonov, T. Gebrenegus, M. Tuller, Segmentation of X-Ray Computed Tomography Images of Porous Materials: A Crucial Step for Characterization and Quantitative Analysis of Pore Structures, Water Resources Research, 45 (2009).
- [103] R.A. Ketcham, D.T. Slottke, J.M. Sharp, Three-dimensional measurement of fractures in heterogeneous materials using high-resolution X-ray computed tomography, Geosphere, 6 (2010) 499-514.

- [104] R. Quey, P.R. Dawson, F. Barbe, Large-scale 3D random polycrystals for the finite element method: Generation, meshing and remeshing, *Computer Methods in Applied Mechanics and Engineering*, 200 (2011) 1729-1745.
- [105] S. Bryant, M. Blunt, Prediction of relative permeability in simple porous media, *Physical Review A*, 46 (1992) 2004-2011.
- [106] S.L. Bryant, P.R. King, D.W. Mellor, Network model evaluation of permeability and spatial correlation in a real random sphere packing, *Transp Porous Med*, 11 (1993) 53-70.
- [107] S.L. Bryant, D.W. Mellor, C.A. Cade, Physically representative network models of transport in porous media, *AIChE Journal*, 39 (1993) 387-396.
- [108] S. Bakke, P.E. Øren, 3-D Pore-Scale Modelling of Sandstones and Flow Simulations in the Pore Networks, *SPE-35479-PA*, 2 (1997) 136-149.
- [109] P.E. Øren, S. Bakke, O.J. Arntzen, Extending Predictive Capabilities to Network Models, *SPE-35479-PA*, 3 (1998) 324-336.
- [110] H. Dong, M.J. Blunt, Pore-network extraction from micro-computerized-tomography images, *Physical Review E*, 80 (2009) 036307.
- [111] K. Terada, T. Miura, N. Kikuchi, Digital image-based modeling applied to the homogenization analysis of composite materials, *Computational Mechanics*, 20 (1997) 331-346.
- [112] Z. Wu, J.M. Sullivan Jr, Multiple material marching cubes algorithm, *International Journal for Numerical Methods in Engineering*, 58 (2003) 189-207.
- [113] D. Boltcheva, M. Yvinec, J.-D. Boissonnat, Mesh generation from 3D multi-material Images, in: *Medical Image Computing and Computer-Assisted Intervention – MICCAI 2009*, Springer Berlin Heidelberg, 2009, pp. 283-290.
- [114] T.K. Dey, F. Janoos, J.A. Levine, Meshing interfaces of multi-label data with Delaunay refinement, *Engineering with Computers*, 28 (2012) 71-82.
- [115] Y. Liu, H.L. Xing, Surface mesh generation of large-scale digital rock images in 3D, *Procedia Computer Science*, 18 (2013) 1208-1216.
- [116] R.E. Guldberg, S.J. Hollister, G.T. Charras, The accuracy of digital image-based finite element models, *Journal of Biomechanical Engineering*, 120 (1998) 289-295.
- [117] W.E. Lorensen, H.E. Cline, Marching cubes: A high resolution 3D surface construction algorithm, in: *Proceedings of the 14th Annual Conference on Computer Graphics and Interactive Techniques*, 1987, pp. 163-169.
- [118] M. Garland, P.S. Heckbert, Surface simplification using quadric error metrics, in: *Proceedings of the 24th Annual Conference on Computer Graphics and Interactive Techniques*, 1997, pp. 209-216.
- [119] H. Hoppe, Progressive meshes, in: *Proceedings of the 23rd annual conference on computer graphics and interactive techniques*, ACM, 1996, pp. 99-108.
- [120] G.M. Nielson, Dual Marching Cubes, in: *Proceedings of the conference on Visualization '04*, IEEE Computer Society, 2004, pp. 489-496.
- [121] S. Schaefer, J. Warren, Dual Marching Cubes: Primal Contouring of Dual Grids, *Computer Graphics Forum*, 24 (2005) 195-201.
- [122] D.C. Banks, S.A. Linton, Counting cases in marching cubes: toward a generic algorithm for producing subtopes, in: *IEEE Visualization*, 2003, pp. 51-58.
- [123] M. Bertram, G. Reis, R.H. van Lengen, S. Köhn, H. Hagen, Non-manifold mesh extraction from time-varying segmented volumes used for modeling a human heart, in: *Proceedings of the Seventh Joint Eurographics / IEEE VGTC Conference on Visualization*, 2005, pp. 199-206.
- [124] P. Shirley, A. Tuchman, A Polygonal Approximation to Direct Scalar Volume Rendering, *Computer Graphics*, 24 (1990) 63-70.
- [125] K.S. Bonnell, M.A. Duchaineau, D.R. Schikore, B. Hamann, K.I. Joy, Material interface reconstruction, *IEEE Transactions on Visualization and Computer Graphics*, 9 (2003) 500-511.
- [126] V. d'Otreppe, R. Boman, J.-P. Ponthot, Generating smooth surface meshes from multi-region medical images, *International Journal for Numerical Methods in Biomedical Engineering*, 28 (2012) 642-660.

- [127] J. Schreiner, C.E. Scheidegger, C.T. Silva, High-Quality Extraction of Isosurfaces from Regular and Irregular Grids, *IEEE Transactions on Visualization and Computer Graphics*, 12 (2006) 1205-1212.
- [128] C.E. Scheidegger, S. Fleishman, C.T. Silva, Triangulating point set surfaces with bounded error, in: *Proceedings of the Third Eurographics Symposium on Geometry Processing*, Eurographics Association, Vienna, Austria, 2005, pp. 63-72.
- [129] J. Schreiner, C.E. Scheidegger, S. Fleishman, C.T. Silva, Direct (Re)Meshing for Efficient Surface Processing, *Computer Graphics Forum*, 25 (2006) 527-536.
- [130] T. Karkanis, A.J. Stewart, Curvature-dependent triangulation of implicit surfaces, *Computer Graphics and Applications*, IEEE, 21 (2001) 60-69.
- [131] M. Meyer, R. Whitaker, R.M. Kirby, C. Ledergerber, H. Pfister, Particle-based Sampling and Meshing of Surfaces in Multimaterial Volumes, *IEEE Transactions on Visualization and Computer Graphics*, 14 (2008) 1539-1546.
- [132] M. Meyer, R.M. Kirby, R. Whitaker, Topology, Accuracy, and Quality of Isosurface Meshes Using Dynamic Particles, *IEEE Transactions on Visualization and Computer Graphics*, 13 (2007) 1704-1711.
- [133] G.L. Kindlmann, R.S.J. Estepar, S.M. Smith, C.F. Westin, Sampling and Visualizing Creases with Scale-Space Particles, *IEEE Transactions on Visualization and Computer Graphics*, 15 (2009) 1415-1424.
- [134] T.K. Dey, J.A. Levine, Delaunay meshing of piecewise smooth complexes without expensive predicates, *Algorithms*, 2 (2009) 1327-1349.
- [135] H.K. Zhao, T. Chan, B. Merriman, S. Osher, A Variational Level Set Approach to Multiphase Motion, *Journal of Computational Physics*, 127 (1996) 179-195.
- [136] D. Boltcheva, M. Yvinec, J.-D. Boissonnat, Feature preserving Delaunay mesh generation from 3D multi-material images, *Computer Graphics Forum*, 28 (2009) 1455-1464.
- [137] N. Amenta, M. Bern, Surface Reconstruction by Voronoi Filtering, *Discrete & Computational Geometry*, 22 (1999) 481-504.
- [138] W. Wang, E. Hakami, A Segmentation Algorithm for Rock Fracture Detection, in: S. Singh, M. Singh, C. Apte, P. Perner (Eds.) *Pattern Recognition and Image Analysis*, Springer Berlin Heidelberg, 2005, pp. 580-588.
- [139] Y. Liu, H.L. Xing, A feature extracting and meshing approach for sheet-like structures in rocks, *Computer methods in applied mechanics and engineering*, 276 (2014) 396-409.
- [140] A. Paluszny, S.K. MatthAI, M. Hohmeyer, Hybrid finite element–finite volume discretization of complex geologic structures and a new simulation workflow demonstrated on fractured rocks, *Geofluids*, 7 (2007) 186-208.
- [141] C. Galera, C. Bennis, I. Moretti, J.L. Mallet, Construction of coherent 3D geological blocks, *Computers & Geosciences*, 29 (2003) 971-984.
- [142] L. Feltrin, J. McLellan, N. Oliver, Modelling the giant, Zn-Pb-Ag Century deposit, Queensland, Australia, *Computers & Geosciences*, 35 (2009) 108-133.
- [143] A. Bistacchi, M. Massironi, G.V. Dal Piaz, G. Dal Piaz, B. Monopoli, A. Schiavo, G. Toffolon, 3D fold and fault reconstruction with an uncertainty model: An example from an Alpine tunnel case study, *Computers & Geosciences*, 34 (2008) 351-372.
- [144] C.L.C. De Veslud, M. Cuney, G. Lorilleux, J.J. Royer, M. Jébrak, 3D modeling of uranium-bearing solution-collapse breccias in Proterozoic sandstones (Athabasca Basin, Canada)--Metallogenic interpretations, *Computers & Geosciences*, 35 (2009) 92-107.
- [145] P. Calcagno, J.P. Chilès, G. Courrioux, A. Guillen, Geological modelling from field data and geological knowledge: Part I. Modelling method coupling 3D potential-field interpolation and geological rules, *Physics of the Earth and Planetary Interiors*, 171 (2008) 147-157.
- [146] P. Calcagno, G. Courrioux, A. Guillen, D. Fitzgerald, P. McInerney, How 3D implicit geometric modelling helps to understand geology: the 3DGeoModeller methodology, in: *Proceedings of Society for Mathematical Geology XIth International Congress*, 2006, pp. 2004-2007.

- [147] H. Kessler, S. Mathers, The past, present and future of 3D geology in BGS, *Journal Open University Geological Society*, 27 (2006) 13-15.
- [148] H. Kessler, S. Mathers, H.G. Sobisch, The capture and dissemination of integrated 3D geospatial knowledge at the British Geological Survey using GSI3D software and methodology, *Computers & Geosciences*, 35 (2009) 1311-1321.
- [149] G. Courrioux, S. Nullans, A. Guillen, J.D. Boissonnat, P. Repusseau, X. Renaud, M. Thibaut, 3D volumetric modelling of Cadomian terranes (Northern Brittany, France): an automatic method using Voronoï diagrams, *Tectonophysics*, 331 (2001) 181-196.
- [150] Q. Wu, H. Xu, An approach to computer modeling and visualization of geological faults in 3D, *Computers & Geosciences*, 29 (2003) 503-509.
- [151] Q. Wu, H. Xu, X. Zou, An effective method for 3D geological modeling with multi-source data integration, *Computers & Geosciences*, 31 (2005) 35-43.
- [152] Y. Liu, H.L. Xing, Z. Guan, An indirect approach for automatic generation of quadrilateral meshes with arbitrary line constraints, *International Journal for Numerical Methods in Engineering*, 87 (2011) 906-922.
- [153] Y. Liu, H.L. Xing, A boundary focused quadrilateral mesh generation algorithm for multi-material structures, *Journal of Computational Physics*, 232 (2013) 516-528.
- [154] T. Coupez, H. Dignonnet, R. Ducloux, Parallel meshing and remeshing, *Applied Mathematical Modelling*, 25 (2000) 153-175.
- [155] H. Borouchaki, P. Laug, A. Cherouat, K. Saanouni, Adaptive remeshing in large plastic strain with damage, *International Journal for Numerical Methods in Engineering*, 63 (2005) 1-36.
- [156] P.O. Bouchard, F. Bay, Y. Chastel, I. Toven, Crack propagation modelling using an advanced remeshing technique, *Computer Methods in Applied Mechanics and Engineering*, 189 (2000) 723-742.
- [157] P.O. Bouchard, F. Bay, Y. Chastel, Numerical modelling of crack propagation: automatic remeshing and comparison of different criteria, *Computer Methods in Applied Mechanics and Engineering*, 192 (2003) 3887-3908.
- [158] R. Boussetta, T. Coupez, L. Fourment, Adaptive remeshing based on a posteriori error estimation for forging simulation, *Computer Methods in Applied Mechanics and Engineering*, 195 (2006) 6626-6645.
- [159] A. Khoei, H. Azadi, H. Moslemi, Modeling of crack propagation via an automatic adaptive mesh refinement based on modified superconvergent patch recovery technique, *Engineering Fracture Mechanics*, 75 (2008) 2921-2945.
- [160] T. Frank, A.-L. Tertois, J.-L. Mallet, 3D-reconstruction of complex geological interfaces from irregularly distributed and noisy point data, *Computers & Geosciences*, 33 (2007) 932-943.
- [161] P. Durand-Riard, G. Caumon, P. Muron, Balanced restoration of geological volumes with relaxed meshing constraints, *Computers & Geosciences*, 36 (2010) 441-452.
- [162] H.L. Xing, Y. Liu, Mesh Generation for 3D Geological Reservoirs with Arbitrary Stratigraphic Surface Constraints, *Procedia Computer Science*, 29 (2014) 897-909.
- [163] O.C. Zienkiewicz, J.Z. Zhu, A simple error estimator and adaptive procedure for practical engineering analysis, *International Journal for Numerical Methods in Engineering*, 24 (1987) 337-357.
- [164] J. Braun, M. Sambridge, Dynamical Lagrangian Remeshing (DLR): a new algorithm for solving large strain deformation problems and its application to fault-propagation folding, *Earth and Planetary Science Letters*, 124 (1994) 211-220.
- [165] Y. Wang, J.P. Renaud, M.G. Anderson, C.B. Allen, A boundary and soil interface conforming unstructured local mesh refinement for geological structures, *Finite Elements in Analysis and Design*, 40 (2004) 1429-1443.
- [166] J. Pellerin, B. Lévy, G. Caumon, A. Botella, Automatic surface remeshing of 3D structural models at specified resolution: A method based on Voronoi diagrams, *Computers & Geosciences*, 62 (2014) 103-116.

- [167] H. Zhang, W. Xu, S. Di, P. Thomson, Quadratic programming method in numerical simulation of metal forming process, *Computer Methods in Applied Mechanics and Engineering*, 191 (2002) 5555-5578.
- [168] C. Park, J.S. Noh, I.S. Jang, J.M. Kang, A new automated scheme of quadrilateral mesh generation for randomly distributed line constraints, *Computer-Aided Design*, 39 (2007) 258-267.
- [169] T.C. Lee, R.L. Kashyap, C.N. Chu, Building Skeleton Models via 3-D Medial Surface Axis Thinning Algorithms, *CVGIP: Graphical Models and Image Processing*, 56 (1994) 462-478.
- [170] Y. Zhang, J. Qian, Resolving topology ambiguity for multiple-material domains, *Computer Methods in Applied Mechanics and Engineering*, 247–248 (2012) 166-178.
- [171] Y. Zhang, J. Qian, Dual Contouring for domains with topology ambiguity, *Computer Methods in Applied Mechanics and Engineering*, 217–220 (2012) 34-45.
- [172] M. Attene, M. Campen, L. Kobbelt, Polygon mesh repairing: An application perspective, *ACM Computing Surveys*, 45 (2013) 1-33.
- [173] S.H. Lo, Optimization of tetrahedral meshes based on element shape measures, *Computers & Structures*, 63 (1997) 951-961.
- [174] J.R. Shewchuk, What is a good linear element? interpolation, conditioning, and quality measures, in: *Proceedings of the 11th International Meshing Roundtable*, 2002, pp. 115-126.
- [175] Z. Wu, J.M. Sullivan, Multiple material marching cubes algorithm, *International Journal for Numerical Methods in Engineering*, 58 (2003) 189-207.
- [176] S.D. Golding, I.T. Uysal, M. Glikson, K.A. Baublys, P.N. Southgate, Timing and chemistry of fluid-flow events in the Lawn Hill platform, northern Australia, *Economic Geology*, 101 (2006) 1231-1250.
- [177] Y. Zhang, P. Sorjonen-Ward, A. Ord, P. Southgate, Fluid flow during deformation associated with structural closure of the Isa superbasin at 1575 Ma in the central and northern Lawn Hill platform, northern Australia, *Economic Geology*, 101 (2006) 1293-1312.
- [178] L. Feltrin, Predictive modelling of prospectivity for Pb–Zn deposits in the Lawn Hill Region, Queensland, Australia, *Ore Geology Reviews*, 34 (2008) 399-427.
- [179] Y. Liu, S.H. Lo, Z.Q. Guan, H.W. Zhang, Boundary recovery for 3D Delaunay triangulation, *Finite Elements in Analysis and Design*, 84 (2014) 32-43.
- [180] J.R. Shewchuk, Two discrete optimization algorithms for the topological improvement of tetrahedral meshes, in, 2002.
- [181] P. Alliez, D. Cohen-Steiner, M. Yvinec, M. Desbrun, Variational tetrahedral meshing, *ACM Transactions on Graphics*, 24 (2005) 617-625.
- [182] D. Vartziotis, J. Wipper, B. Schwald, The geometric element transformation method for tetrahedral mesh smoothing, *Computer Methods in Applied Mechanics and Engineering*, 199 (2009) 169-182.
- [183] P.L. George, H. Borouchaki, *Delaunay triangulation and meshing: application to finite elements*, Kogan Page, 1998.